MAGNETOHYDRODYNAMIC LATTICE BOLTZMANN SIMULATIONS OF TURBULENCE AND RECTANGULAR JET FLOW

A Thesis

by

BENJAMIN M. RILEY

Submitted to the Office of Graduate Studies of
Texas A&M University
in partial fulfillment of the requirements for the degree of

MASTER OF SCIENCE

May 2007

Major Subject: Aerospace Engineering

MAGNETOHYDRODYNAMIC LATTICE BOLTZMANN SIMULATIONS OF TURBULENCE AND RECTANGULAR JET FLOW

A Thesis

by

BENJAMIN M. RILEY

Submitted to the Office of Graduate Studies of
Texas A&M University
in partial fulfillment of the requirements for the degree of

MASTER OF SCIENCE

Approved by:

Chair of Committee, Sharath S. Girimaji
Committee Members, Gerald Morrison
Jacques C. Richard
Head of Department, Helen Reed

May 2007

Major Subject: Aerospace Engineering

ABSTRACT

Magnetohydrodynamic Lattice Boltzmann Simulations of Turbulence and Rectangular Jet Flow. (May 2007)
Benjamin M. Riley, B.S., Texas A&M University
Chair of Advisory Committee: Dr. Sharath S. Girimaji

Magnetohydrodynamic (MHD) investigations of decaying isotropic turbulence and rectangular jets (RJ) are carried out. A novel MHD lattice Boltzmann scheme that combines multiple relaxation time (MRT) parameters for the velocity field with a single relaxation time (SRT) parameter for the Maxwell's stress tensor is developed for this study.

In the MHD homogeneous turbulence studies, the kinetic/magnetic energy and enstrophy decays, kinetic enstrophy evolution, and vorticity alignment with the strain-rate tensor are evaluated to assess the key physical MHD turbulence mechanisms. The magnetic and kinetic energies interact and exchange through the influence of the Lorentz force work. An initial random fluctuating magnetic field increases the vortex stretching and forward cascade mechanisms. A strong uniform mean magnetic field increases the anisotropy of the turbulent flow field and causes inverse cascading.

In the RJ studies, an investigation into the MHD effects on velocity, instability, and the axis-switching phenomena is performed at various magnetic field strengths and Magnetic Reynolds Numbers. The magnetic field is found to decelerate the jet core, inhibit instability, and prevent axis-switching. The key physical mechanisms are: (i) the exchange of energy between kinetic and magnetic modes and (ii) the magnetic field effect on the vorticity evolution.

From these studies, it is found that magnetic field influences momentum, vorticity, and energy evolution and the degree of modification depends on the field strength. This interaction changes vortex evolution, and alters turbulence processes and rectangular jet flow characteristics. Overall, this study provides more insight into the physics of MHD flows, which suggests possible applications of MHD Flow Control.

Dedicated to my father Stephen Riley, brother Jonathon Riley, mema Viola Riley, grandma Ila Thornton, and stepmom Katie Riley

ACKNOWLEDGMENTS

I would like to give a great deal of thanks to Dr. Sharath S. Girimaji for being my advisor and committee chair. He has provided me with a lot of guidance and direction during my graduate studies. Academically, he has guided me to a greater level than I thought possible, and he has taught me a lot in general about how best to succeed in the face of difficult tasks.

Dr. Richard has admirably guided me during my graduate education. He has spent a tremendous amount of time helping me with research and editing my work. He has always been readily available for questions, advice, and help whenever it's needed. His enthusiasm and knowledge in research are not easily matched by many. It has been a great experience to learn and work alongside him during my graduate studies.

I would also like to thank Dr. Morrison for being a part of my committee, providing an experienced, practical perspective to my research.

I have really appreciated all of my teammates in the Turbulence Research Group. Everyone has always been very motivational, supportive, and hard working. An extra special thanks is given for the help of Tucker Lavin, Sunny Jain, Sawan Suman, Kurnchel Lee, Richard Rhodes, Andrea Hsu, Dr. Dahzi Yu, and Dr. Huidan Yu.

I would also like to thank Shane Schouten, Michael Albright, Randi Fuller, Lupe Perez, and Chris Haag, from my senior design team, Manticorps Aeronautics (2005). All of whom helped give me the desire to pursue further education in aerospace engineering.

I would like to thank my parents, brother, mema, and grandma for their unconditional love and support.

Finally, I would also like to thank Karen Knabe for all of her help during my tenure in graduate school. I've always been able to count on her help and guidance.

TABLE OF CONTENTS

Page

Page

Page

LIST OF FIGURES

Page

Page

Page

Page

CHAPTER I

INTRODUCTION

Magnetohydrodynamics is the study of the dynamics of the interaction between conducting fluids or plasmas with magnetic fields. The importance of conducting fluids and plasmas in nature is made very apparent in the fact that 90% of matter in the universe is plasma. Many energy production or conservation processes along with propulsion systems involve the use and control of conducting fluids and plasmas. MHD generators and accelerators [1-4] manipulate kinetic energy to generate electricity or accelerate flows. MHD pumps [5] are used to perfect steel casting methods, producing alloys with less defects. The study and modeling of solar flares, sunspots, and planetary magnetic fields are best realized by MHD physics [6]. MHD processes are involved in tokomak fusion reactors [6] where plasma confinement and stability are extremely important. Tokomak reactors [6] offer potentially the most abundant and cheap energy source ever. Electric plasma propulsion systems [7] require plasma flow control processes to produce thrust and enhance performance. These propulsion systems in contrary to conventional chemical propulsion are much more fuel efficient. Electric propulsion systems have already enhanced unmanned interplanetary space travel. If the energy efficiency and thrust output can be improved, then manned interplanetary space travel can also be greatly advanced.

Magnetohydrodynamic studies are largely characterized by the kinetic/magnetic energy interaction along with Lorentz force influence on the flow field structures. A magnetic field has the tendency to redirect momentum and kinetic energy due to the Lorentz force, changing the flow field properties. The amount of influence is dictated by the relative strength between these parameters. The ultimate characteristic of the magnetic field is to provide directionality or anisotropy to a flow based on the magnetic field configuration. This effect of the magnetic field is very notable in vorticity, momentum, and energy dynamics, making magnetic fields highly coveted as a flow

---

This thesis follows the style and format of Computers & Fluids.

control concept for conducting fluids and plasmas. A proper understanding of these phenomena can enhance our ability to harness the properties of magnetized fluids and plasmas to improve technology and scientific knowledge.

In order to understand the plasma phenomena, it's characteristics need to be properly described. There are three different regimes of plasma descriptions pertaining to the microscopic, macroscopic, and mesoscopic levels. These descriptions may be made for both magnetohydrodynamic and hydrodynamic phenomena. Studies are performed utilizing mesoscopic theory based numerical models to describe MHD flow.

A. Numerical Modeling of the Kinetic Description of Particles

The lattice Boltzmann method (LBM) is a kinetic theory based numerical modeling method that can recover the Navier-Stokes equations, within certain constrictions, by using the BGK collision operator [8-10]. A modification to this method can be used to accurately solve the MHD equations, which are derived from kinetic plasma theory. The details of the governing MHD equations will be covered later in the thesis. The MHD-LBM is the numerical scheme utilized in this thesis to model MHD physics.

LBM is a well-proven and reliable tool in calculating low Mach number incompressible flows, comparing well to conventional methods [8-10]. The LBM has been used to model plasma flows [11-16], chemically reacting flows [17-19], external flows [20], turbulent flows [21 and 22], jet flows [23 and 24], and other flows as catalogued in [25-27]. This method is a kinetic-theory-based DNS method derived from the mesoscopic Boltzmann equation (linearized in Bhatnagar-Gross-Krook (BGK) form) from which the Navier-Stokes equations are recovered with application of the Chapman-Enskog expansion.

The MHD-LBM has been used by Dellar, Breyiannis, Valougeorgis, Richard, and Prenmath and Pattison. Dellar [12] developed the method in which the magnetic field is modeled using the lattice Boltzmann equation, and he modifies the equilibrium equation formulation (EEF) to include the Maxwell's stress tensor. Breyannis and Valgeorgis [11] modeled the effect of the Lorentz force using a body force formulation (BFF) term.

Premnath and Pattison [28] demonstrated that the equation for the physical flow field using BFF can be modeled successfully using the Multi-Relaxation Time Method (MRT). With all of these different forms of the MHD-LBM, test cases such as Hartmann channel flow and Orzang-Vortex have been successfuly simulated, validating MHD-LBM within certain constraints of the low Mach number limit and high ratio of the hydrodynamic pressure to magnetic field pressure. Richard [13-16] has taken MHD-LBM another step by using the same method as Breyannis and Valgeorgis [11] to model the plasma flow in the discharge cathode assembly (DCA) of ion thrusters used in electric space propulsion systems.

B. Engineering Applications of MHD

The main interest of this paper is to assess magnetohydrodynamic flow control applications to aerospace propulsion. These applications primarily encompass hypersonic and plasma flow fields. In hypersonic flow, weakly ionized gases are formed, which lead to new phenomena unlike regimes below the Mach number of 5. The different parameters, which have been simulated, include boundary layer effects, flow acceleration (MHD accelerator), and power extraction (MHD generator) [2 and 3]. The Ajax concept is a good example [1]. It uses an MHD generator-accelerator system as an engine bypass, to increase thrust output. Figure 1 shows a simple layout of the Ajax scheme.

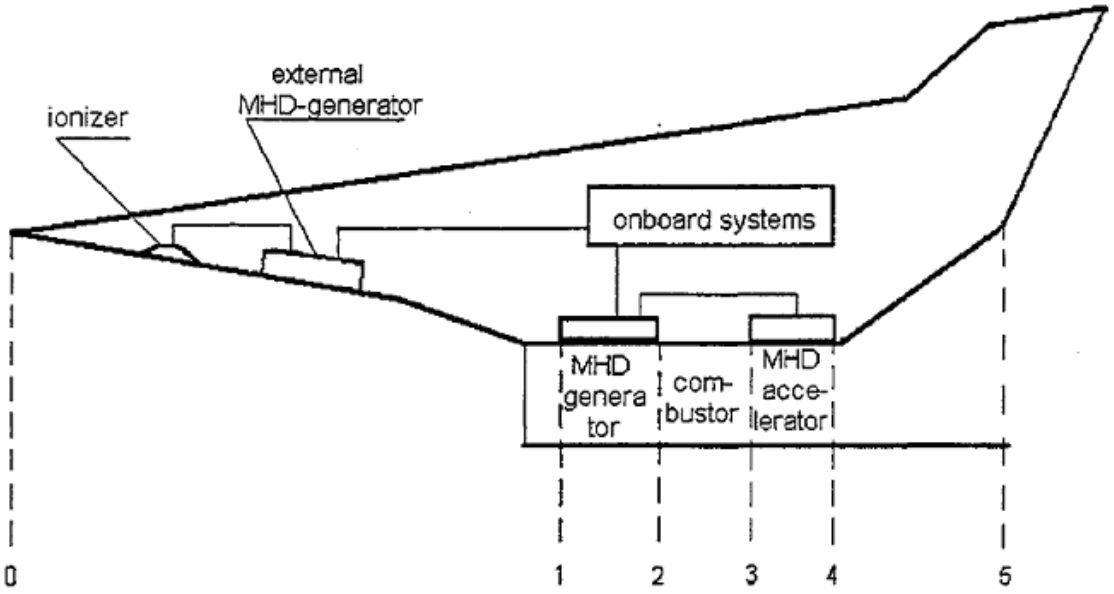

Figure 1. Simple Schematic of MHD Generator-Accelerator Ajax System [1]

MHD generators and accelerators are channels applying a magnetic field, producing favorable and adverse effects on the flow to either extract energy from or add to the flow field. The physical effects of these channels can be understood through a boundary layer analysis under the effects of an external magnetic field. In MHD generators, the Lorentz body force is added to the viscous forces, thus increasing the thickness of the boundary layer. In MHD accelerators, the Lorentz body force acts in the direction of the flow against the viscous forces, decreasing the boundary layer thickness. Figure 2, from a study on boundary layers in MHD performed [2], depicts this effect.

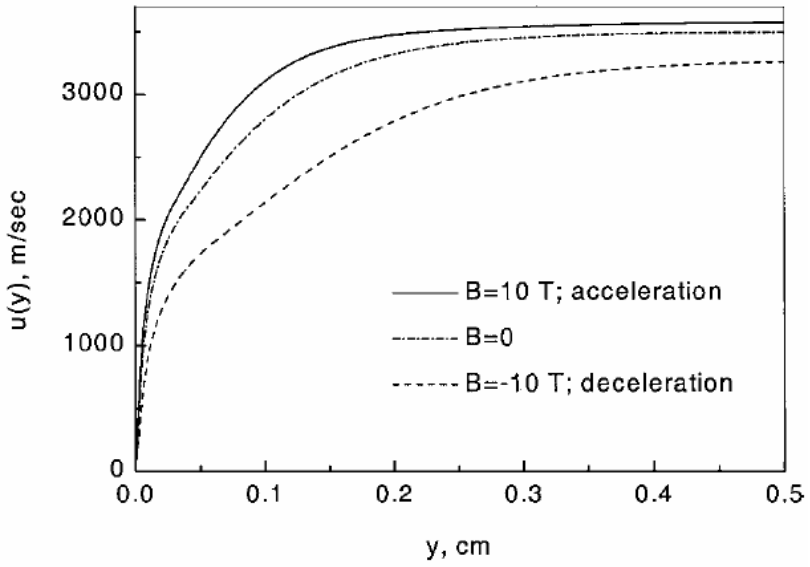

Figure 2. Lorentz Force Effect on Boundary Layers [2]

This trend corresponds with the proper physical theory behind the magnetic field effects. With a magnetic field, of an accelerator, acting with the flow, the flow field has less viscous drag acting against it. This means that the flow velocity will be higher and the boundary layer will be smaller and vice versa for the case of the generator.

In plasma propulsion systems, the plasma flow field, unlike for hypersonic flow fields, is considered to be fully ionized. This characteristic makes magnetic fields more influential; however, it also brings about a greater need for that effect as plasmas operate at temperatures near two million degrees Kelvin. At that temperature, magnetic fields have to be utilized to prevent plasma particles from damaging the engine.

Tokomaks [6] used in fusion reactor research provide a good example of magnetic confinement schemes. Tokomaks utilize a toriodal magnetic field confinement scheme that has had the most success at providing plasma confinement. This confinement scheme is presented in figure 3.

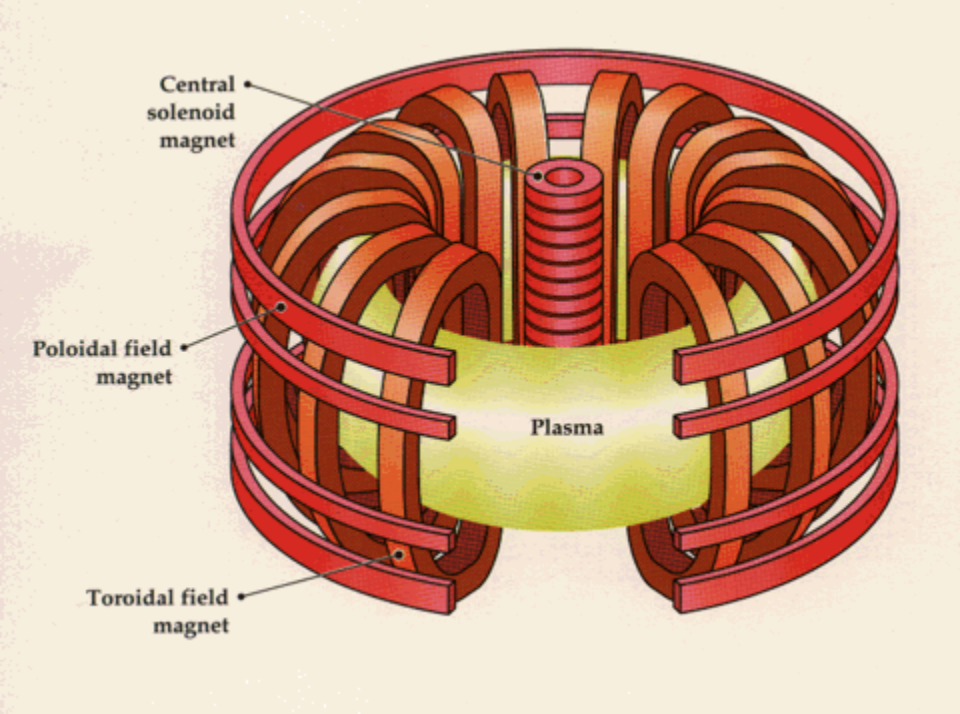

Figure 3. Tokomak Currents and Fields: (a) Toriodal Plasma Current Induced by Transformer (b) Primary Winding [29]

In tokomaks, a toroidal magnetic field is generated by currents wrapped around the torus. The poloidal magnetic field is generated by the current of the plasma around the torus, which is induced by changing the magnetic field in the core of the torus. This scheme is still under development, but it has shown the best results in confining plasma despite the large amount of instabilities exhibited. In contrast to tokomaks, plasma propulsion schemes do not confine plasmas. They control and propel plasma motion to produce thrust.

Electric propulsion systems have become increasingly desired because they have a much higher specific impulse, I_{sp} meaning that their fuel efficiency is much greater than that of chemical propulsion. A drawback of electric propulsion is that it does not produce as much thrust as chemical propulsion. For short range missions either within earth orbit or to the moon, chemical propulsion presents the most effective scheme. However, for long-range missions to another planet, where the weight of fuel becomes an increasingly

important mission factor, electric propulsion systems become more favorable. Over a longer period of time, electric propulsion schemes can generate greater amounts of thrust due to the constant acceleration of propellant. Overall, the effective thrust capability over a large period of time and much greater fuel efficiency of electric propulsion systems makes them more effective for long-range space missions than chemical propulsion systems.

Electric propulsion schemes are characterized as either electrothermal, electrostatic, and electromagnetic [30]. Electrothermal schemes heat propellant by either an electrical arc discharge through the fluid or by electrical heating through a wall. Some examples are the resistojet [7] and the arcjet [30]. Electrostatic propulsion systems [30] accelerate propellants consisting of discrete charged particles by electrostatic forces. The particles are charged by electron bombardment. Some examples are electron bombardment thrusters [30] and field/emission colloid thrusters [7]. Ion thrusters [31] have been well developed and used in orbiting satellites. Electromagnetic propulsion systems accelerate ionized propellant by the interaction of an external and internal magnetic field with electrical currents driven through the propellant stream. Some examples are VASIMR [32], Magnetoplasmadynamic Thrusters [33], Pulsed Plasma thrusters [34], and Hall thrusters [7]. Of all the examples, arcjets, resistojets, ion thrusters, and Hall thrusters have seen usage in satellites.

Currently, ion and Hall thrusters are the most effective electric propulsion schemes that have been significantly developed for practical use. Figure 4 explains the components of ion thrusters. In ion thrusters, neutral propellant is pumped into the ion production chamber, where it is separated into ions and electrons. The ions and electrons are drawn into separate streams. The ions are accelerated to high speeds by the electrodes and then exit the grid to produce thrust. The grid consists of two screens, a positive and negative one. Ions enter the positive screen first. They the ions are propelled outwards by the negative grid, which causes them to exit. The ionization chamber is maintained at the positive acceleration potential, while the last electrode is grounded at the vehicle potential. Ion thrusters are limited by the erosion of the grids and electrodes due to the physical interaction with the ions. Current testing shows the grid to last for about 10,000 hours.

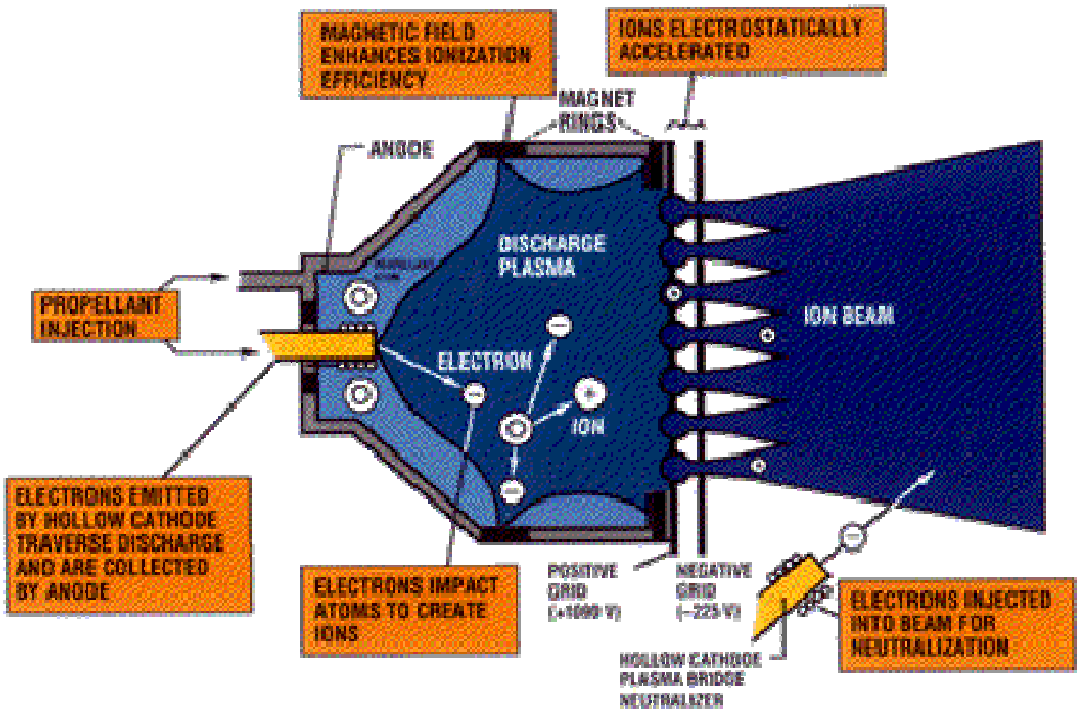

Figure 4. Ion Thruster Components [35]

Hall thrusters consist of two concentric annular magnetic pole pieces, a low pressure propellant, and two electrodes used to give off a discharge to the propellant. The propellant is released by the pressure gradient and passes by the electrodes which give off a discharge that ionizes the propellant with the positive upstream electrode and the negative downstream electrode of the magnetic pole pieces. The figure 5 shows the axial electric field generated by the electrodes and the radial magnetic field caused by the magnetic coils. The interaction between the two fields, $\mathbf{E}\times\mathbf{B}$ called the Hall Effect, produces a current being displaced from both fields in the azimuthal direction that is perpendicular to both fields. This produces a force on the propellant in the axial direction. The Hall thruster is limited by electron losses to the wall, degradation of the anode caused by back-streaming of electrons, and distortion of the external magnetic field caused by the diamagnetic influence of the hall current. This diamagnetic field, if strong enough, acts against the applied magnetic field, inhibiting the thrust output.

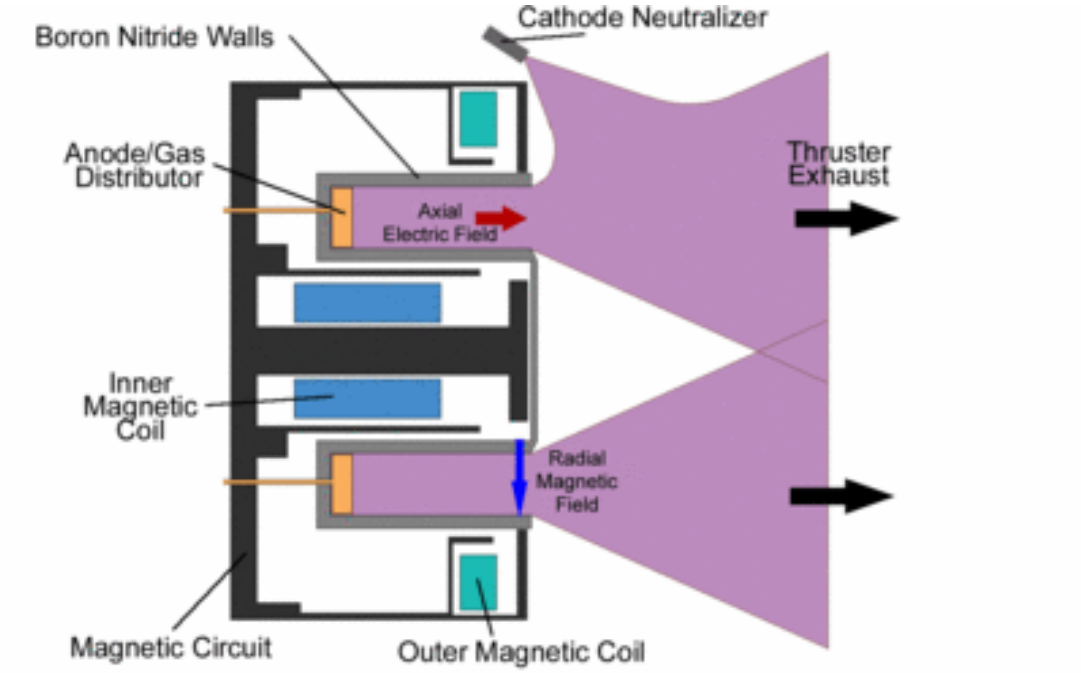

Figure 5. Hall Thruster Components

Hall and ion thrusters are limited in the level of power for which they can operate due to space charge effects. Electromagnetic propulsion systems, utilizing the Lorentz body force to accelerate plasma, can provide very high power levels at high specific impulse thrust. This makes the MPD and VASIMR propulsion systems potentially more favorable schemes for heavier lifting needs such as long-range manned space missions.

The Magnetoplasmadynamic (MPD) thruster, as shown in figure 6, has a central cathode surrounded by a cylindrical anode. As the propellant is ejected into the chamber, a high electric arc is formed between the cathode and anode. Electrons are emitted by the cathode and collide with the propellant to ionize it into plasma. Then a self-induced magnetic field is created by the current returning to the power supply through the cathode. This magnetic field interacts with the current flowing from the anode to the cathode to create an electromagnetic force that propels the plasma out of the engine to create thrust. While the thrust capabilities of MPD's are much greater than ion and Hall thrusters, their current energy efficiency is much less at 40%. Therefore methods of increasing the

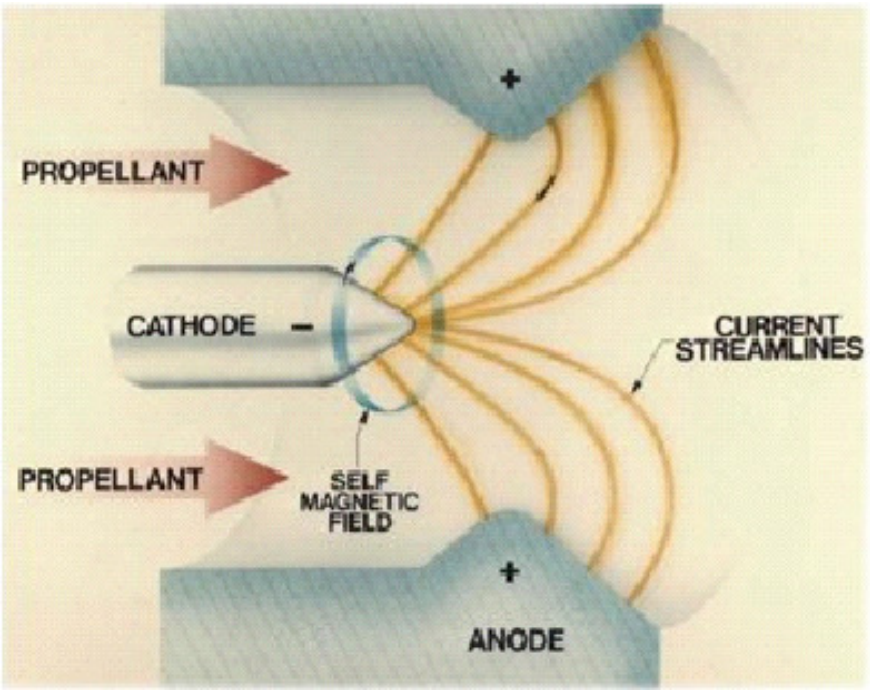

Figure 6. MPD Thruster Components [33]

energy efficiency are being developed to make the use of MPD's feasible. MPD's also incur degradation of the cathode and anode due to interaction with the plasma. VASIMR (Variable Specific Impulse Magnetoplasma Rocket) is a concept, which utilizes a Lorentz force to accelerate plasma to produce thrust. Figure 7 shows the different components of VASIMR [32]. In previous schemes, the greater thrust production capability of magnetic force due to higher power densities was introduced along with lifetime issue while using electrodes. This propulsion scheme shall enhance both areas, as VASIMR does not use electrodes to energize plasma. In this propulsion scheme, there are three main sections: (i) low energy helicon plasma source, (ii) ion-cyclotron resonance heating section (ICRH), and (iii) the magnetic nozzle. The helicon antenna ionizes the propellant by inducing electron-neutron and electron-ion collisions. The ICRH (Ion Cyclotron Resonance Heating) antenna further energizes the ions by increasing the frequency for which they rotate about the axial magnetic field. This process is collisionless, meaning that the amount of energy gained is based on how long

the ion spends in this resonance phase. The magnetic nozzle phase converts the gyro-motion of the plasma into axial motion, producing thrust. The main desirable features of

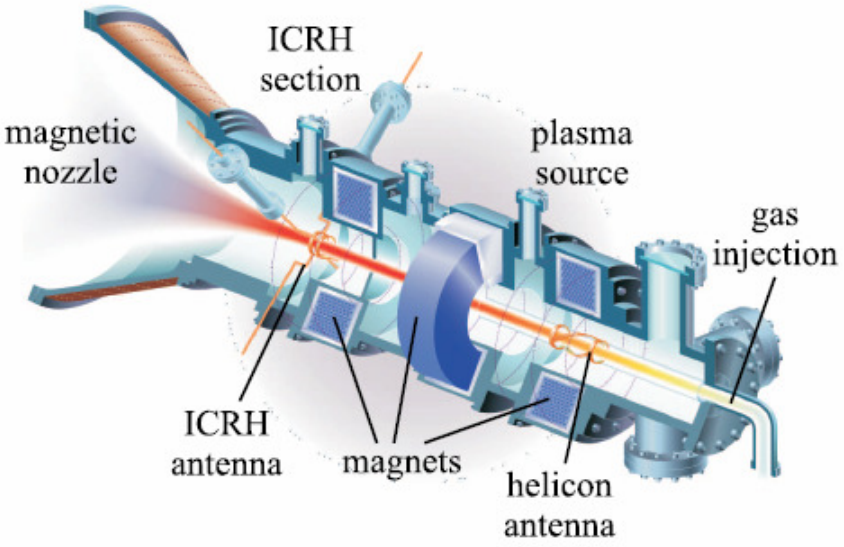

Figure 7. VASIIMR Components [32]

this engine are: (i) no degradation, (ii) high thrust, and (iii) high I_{sp}. This concept is still in the experimental phase as energy efficiency is still a major key issue.

These engineering applications, concerning propulsion and power, show the importance that MHD physics has on technological development. More examples of applications exist, pertaining to liquid metal flows [5], astrophysics [6], and geophysics [6]. It is important to note that in the engineering applications discussed, MHD physics does not fully depict processes that involve flow fields, which are not fully ionized plasma. Greater detail of MHD physics is provided later on in the thesis.

C. Objective of Thesis

The focus of this thesis is to provide a strong theoretical understanding of magnetohydrodynamics and its potential applications to controlling turbulence and rectangular jet flows. The following physical mechanisms will be shown to be the most significant in the flow fields of interest.

- Magnetic tension force of the magnetic field lines
- Kinetic/magnetic energy interaction
- Magnetic field influence on vorticity development

The main topics of this thesis encompass the fundamental theory and the research contributions. The fundamental theory covers the following areas:

- Kinetic Theory and Boltzmann description of particles
- Electromagnetic Theory
- Kinetic Plasma Theory
- Magnetohydrodynamics

The research contributions cover the following areas:

- MHD-LBM formulation, improvement, and verification
- MHD decaying isotropic homogeneous turbulence
- Axis-switching and instabilities in MHD rectangular jets

CHAPTER II

KINETIC THEORY AND THE BOLTZMANN DESCRIPTION OF FLUID PARTICLES

A. Introduction

In developing a model for kinetic plasma, the foundation is set by hydrodynamic fluid models. This chapter reviews over the fundamental aspects of molecular descriptions, the Boltzmann equation, and collision operator dynamics that formulate the hydrodynamic fluid model. The hydrodynamic fluid model provides a foundation for the formulation of the magnetohydrodynamic model.

There are three major descriptions of gases. The first description is the microscopic level in which fluid particles are viewed individually as molecules, at a constant state of motion colliding with one another. This method, called Molecular Dynamics, models each individual molecule according to the Newtonian description. This method can describe molecular motion at all Knudson numbers, $Kn=\lambda/L$, where. L is the characteristic length scale and λ is the mean free path of the molecules. This is ideally the most accurate method in describing fluid media; however, it is by far the least efficient means. Whenever incorporated, Molecular Dynamics usually only describes a system containing a number of particles on an order of 10^{23}, corresponding to Avogadro's Number of 6.022×10^{23} atoms per mole. For practical usage, systems billions of times larger than this will need to be studied.

The second description is the macroscopic level. Fluid particles are viewed individually as clumps of particles comprising of a number of discrete particles on an order of 10^{23}. This is the level in which actions of fluid media are most visible and easy to predict. The Navier-Stokes and Euler equations are used in describing fluid particles at the macroscopic level (also called continuum regime). As the larger order of molecules at which each fluid particle is modeled indicates, the length scale used at this level is much larger than that of the microscopic level. The Knudson number (Kn) for this regime is characterized as being less than 0.2. As the Knudson number gets close to

zero, the normal fluid model no longer applies, as molecules are so closely packed that collisions are insignificant. An inviscid continuum model is used, such as Euler's equations for this case. In this regime, the molecules behave more as solids than as fluids. Summations of actions at the microscopic level, equal an action at the macroscopic level. Hydrodynamic terms such as density, pressure, temperature, viscosity, and velocity represent the average collective behavior of the ensemble of molecules. The hydrodynamic model is fully governed by the continuity equation, Navier-Stokes, and energy equation.

The continuum models are the most developed and used models, but if the atmosphere of the system has much lower densities and pressure, the Knudsen number lowers to values outside the range applicable for the continuum regime. This new regime outside the range of the continuum is the rarefied gas regime. Since there is also such a large gap between the minimum Knudson number of the microscopic level and the macroscopic level, this means that using Molecular Dynamics can still be ineffective in the rarefied gas regime. Therefore a new level between the previous two is defined.

The third description is the mesoscopic level. Kinetic theory, utilizing the Discrete particle model, describes this level in order to bridge the gap between the microscopic and macroscopic levels. The Knudson number for this regime ranges from the inviscid limit (0) to 100. Kinetic theory is typified by using statistical descriptions and molecular distributions to model fluid particles. The Boltzmann equation is used as the governing equation in kinetic theory.

The following figure 8, taken from [36], relates the applicable Knudson number regimes to the continuum and discrete particle models.

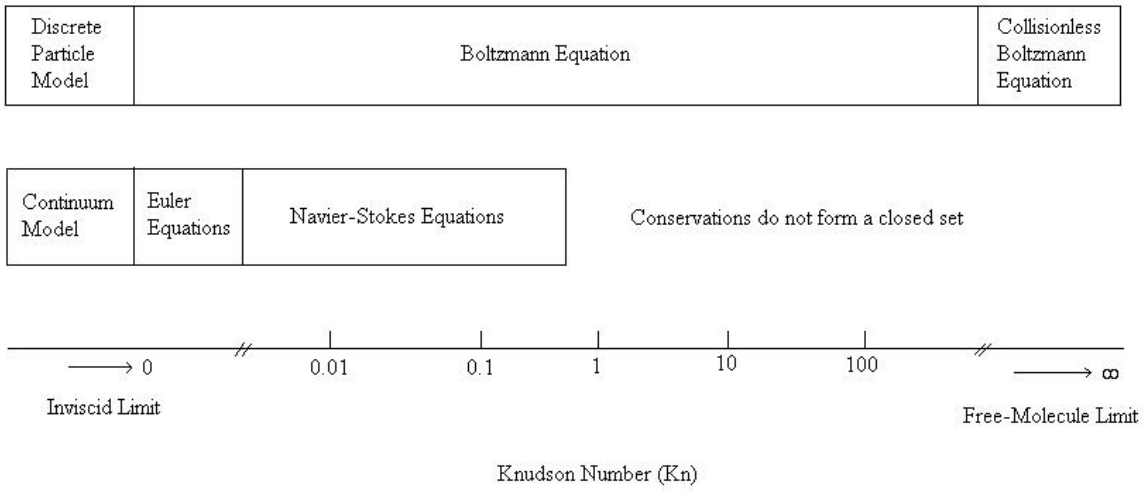

Figure 8. Molecular Models at Different Knudson Number Regimes [36]

B. Kinetic Description of Fluid Particles

The kinetic description of fluid particles begins with the definition of the intermolecular and intramolecular particle structure, defining the energy modes that characterize particle interaction. Then kinetic theory forms a statistical description of particle distributions and how they relate to physical thermodynamic properties. This statistical description is facilitated by the Boltzmann equation. When the Boltzmann equation is combined with collision dynamics of intermolecular interaction, they form the governing kinetic equations of the conservation of molecular density, momentum, and energy at the mesoscopic level. These kinetic equations can be used to retain the Navier-Stokes equations of the continuum level.

1. Molecular Structure

A molecule is influenced by both external and internal forces. The intramolecular forces due to the internal structure bind the molecule together. The internal structure is dictated by the configuration of the atoms of the molecule. The characteristics of the configuration dictate the types of intramolecular effects exhibited in the various energy

modes consisting of: translational, rotational, vibrational, and electronic. These modes are illustrated by figure 9, which is taken out of [36].

Consider a diatomic gas molecules: dumb bell mode 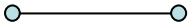

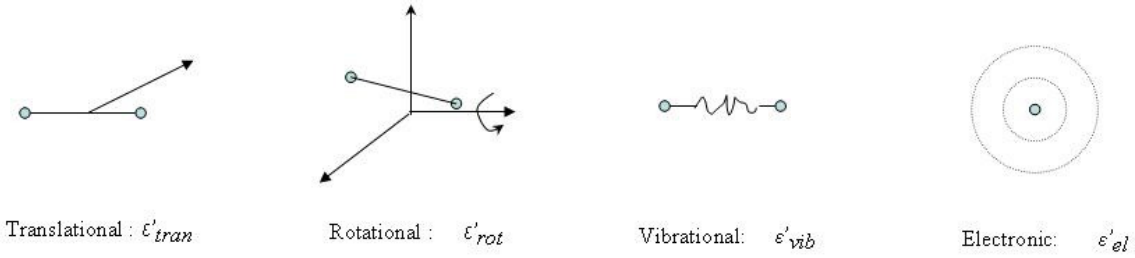

Figure 9. Intramolecular Energy Modes [36]

$\varepsilon' = \varepsilon'_{tran} + \varepsilon'_{rot} + \varepsilon'_{vib} + \varepsilon'_{el}$ Total energy of molecule ε'

$\varepsilon' = \varepsilon'_{tran} + \varepsilon'_{el}$ Total energy of atom ε'

Quantum Mechanics shows that all of these modes exist at discrete values, allowing the microscopic properties to be calculated [36 and 37]. Figure 10, taken from [36] provides a schematic that illustrates the energy levels of the different modes. This figure describes the existence of the energy levels of each mode in relation to the amount of energy. The vibration and electronic modes require relatively large amounts of energy to excite in relation to the translational and rotational energy modes. Therefore, in most situations, translational and rotational modes dominate.

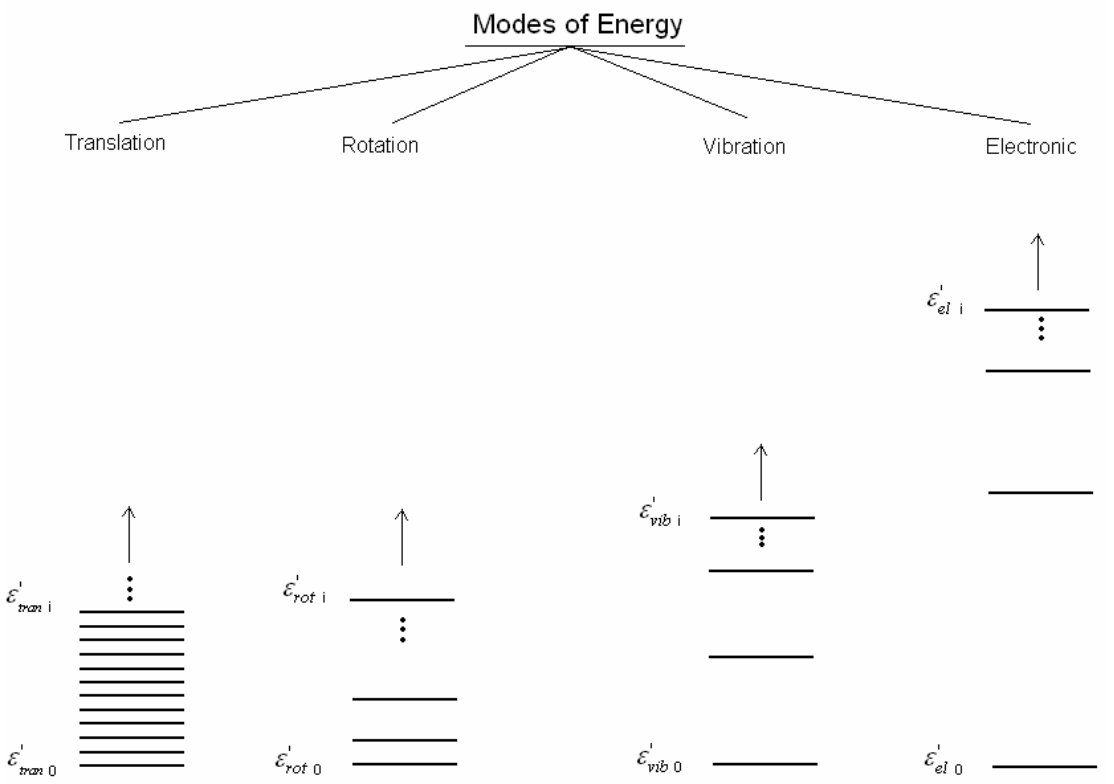

Figure 10. Energy Levels of the various Energy Modes [36]

Figure 11 shows a schematic of the temperature variation of the specific heat for a diatomic gas [36]. Initially, at 1K, translational energy is the only form. Between 1 and 3K, rotation becomes significant. After 3K, both translation and rotational energy modes are fully excited. At 600 K, vibrational energy mode gets excited. Then at 2000 K, the vibrational energy mode of diatomic gases is fully excited. At temperatures where vibrational and electronic modes are excited, is where the realm of MHD resides. In the regimes of dominant vibrational energy excitation is where hypersonics is studied. With even greater temperatures, where electronic energy is dominant, ionization becomes prevalent. This is the regime in which tokomaks [6], electric/plasma propulsion [7], and astrophysical phenomena [6] are studied.

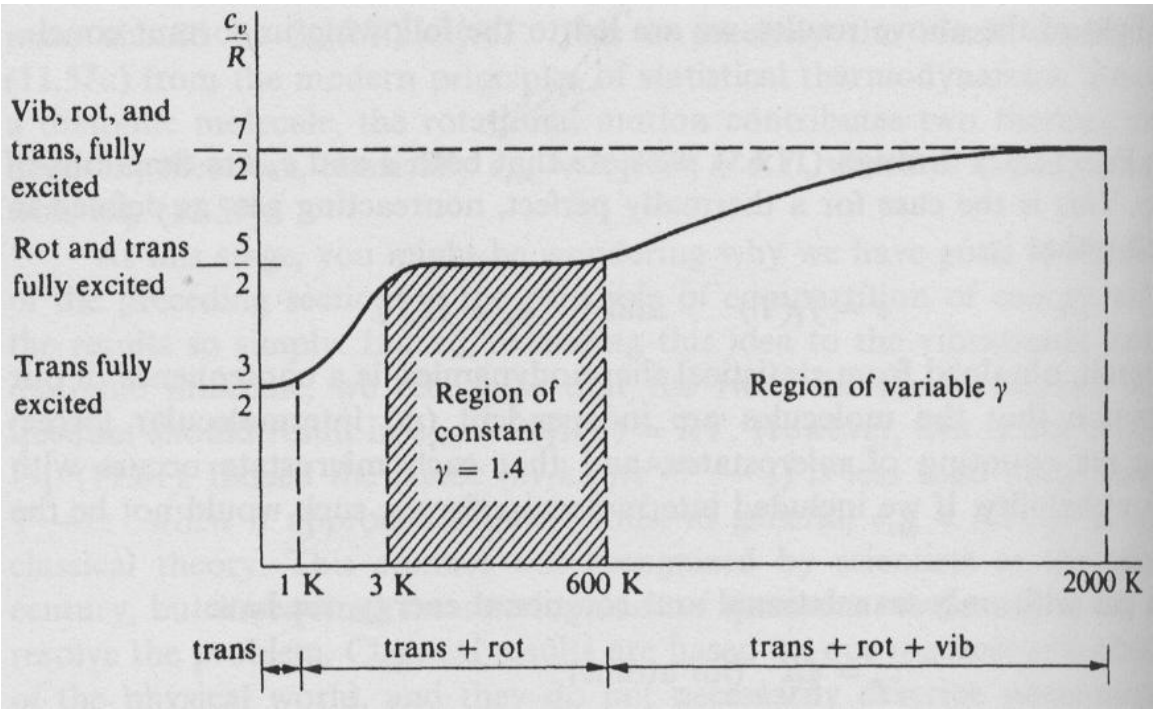

Figure 11. Schematic of Temperature Variation of the Specific Heat for a Diatomic Gas [36]

Figure 12 shows the range of dissociation and ionization of oxygen and nitrogen, the two dominant fluid particles in air [36]. This data, for example, applies to space vehicles on reentry into the earth's atmosphere. In this hypersonic flow regime, vibrational energy dominates. Vibrational energy is due to kinetic effects of linear atomic motion and potential energy effects of intramolecular forces. This effect will lead to the dissociation of fluid particles. In this process, the fluid molecules will split into smaller fluid molecules, atoms, ions, or radicals. Eventually this process will lead to the ionization of the fluid particles. Vibrational excitation begins for air at 800 K. O_2 will begin to dissociate above 2000 K and will be nearly completely dissociated above 4000 K. N_2 will begin to dissociate above 4000 K, and will almost be completely dissociated above the temperature of 9000 K. When dissociation is nearly complete, this means that the oxygen or nitrogen is no longer in its diatomic state, but at its atomic state. At 9000 K, as nitrogen and oxygen are nearly completely dissociated, air begins to ionize. At this temperature is when electronic energy modes become dominant.

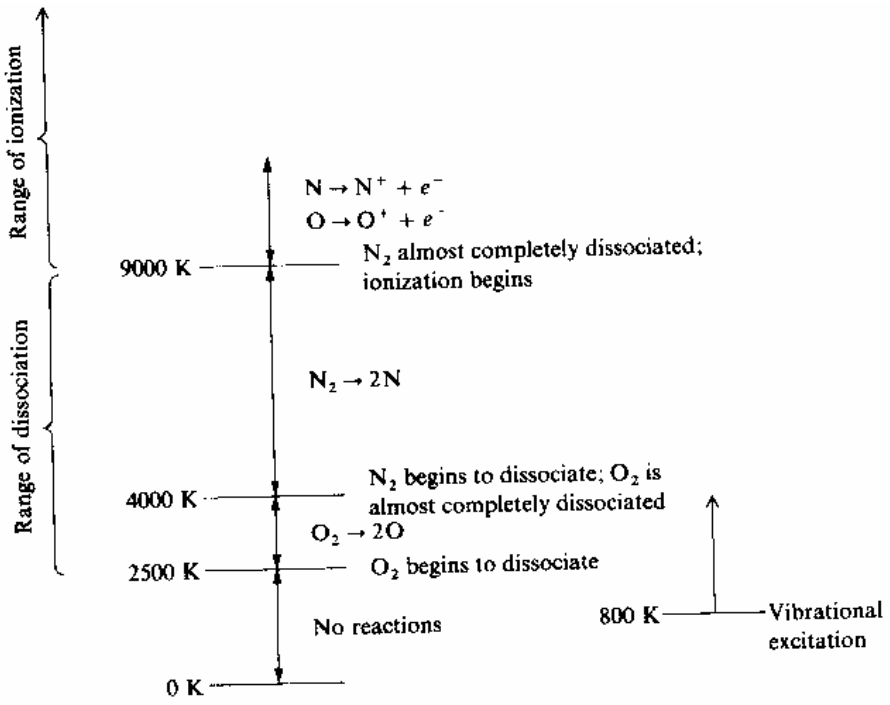

Figure 12. Ranges of Vibrational Excitation, Dissociation, and Ionization of Air at 1 atm [36]

Intermolecular forces are defined as electromagnetic forces that act between molecules. These energy modes are modeled using quantum mechanical models. Then, statistical mechanical summation methods incorporate the assumption of the Boltzmann limit to provide a macroscopic description. The Boltzmann limit is a very important factor in describing the fluid phenomena as it assumes that most energy states have no particles or that the energy states are not degenerate. Physically, the Boltzmann limit ensures that the particles are weakly interacting, allowing the thermodynamic properties to be formulated for the case of ideal gas. Statistically, this describes most fluid phenomena. This condition is usually violated in situations where particle mass is small with density being large (electron gas for example), or when the temperature of particles is extremely low. If this assumption is violated, then Bose-Einstein [36 and 37] or Fermi-Dirac [36 and 37] statistics have to be used in characterizing particle distributions over energy states. The Boltzmann limit is utilized in all descriptions of this paper.

2. Boltzmann Description of Fluid Particles

The Boltzmann equation is derived by using a Gibb's ensemble average to determine the macroscopic properties from the microscopic descriptions [38]. This definition of the Gibbs ensemble leads to the use of the probability distribution function (PDF) f in describing the macroscopic properties.

$$\frac{\partial f}{\partial t} + V_i \frac{\partial f}{\partial x_i} = -\frac{\partial}{\partial V_j}\left[\left\langle A_j \left| \underline{V} \right\rangle nf \right]\right. \quad \text{(Boltzmann Equation)} \tag{2.1}$$

The Boltzmann equation describes the evolution of a probability distribution function of molecular distributions, and how they are affected by internal and external influences.

$$\frac{\partial}{\partial V_j}\left[\left\langle A_j \left| \underline{V} \right\rangle nf \right]\right. = \frac{\partial}{\partial V_j}\left[\left\langle A_{j,external} \left| \underline{V} \right\rangle nf \right]\right. + \frac{\partial}{\partial V_j}\left[\left\langle A_{j,internal} \left| \underline{V} \right\rangle nf \right]\right. \tag{2.2}$$

n is the particle number density, and V_i is the particle velocity. The external forces can consist of intramolecular forces such as gravity and external magnetic fields, and the internal forces are due to molecular collisions. The internal collisions are described by the following collision operator.

$$-\frac{\partial}{\partial V_j}\left[\left\langle A_{j,internal} \left| \underline{V} \right\rangle nf \right]\right. = \left\{\frac{\partial}{\partial t}\left[nf\left(\underline{V}\right)\right]\right\}_{collision} \tag{2.3}$$

The applicability is limited to systems falling under the following assumptions [37 and 38].

- A dilute or extremely low dense gas of point-like molecules, which allows for binary collisions to be considered.
- The distribution function is smooth and can be treated as if it were in physical space.

- The distance between collisions of particles is sufficiently large compared to the range of the two body potential which is defined by the sphere of influence. This assumption is important to eliminate the possibility of a particle having collisions with multiple particles at an instant.

Figure 13 shows the sphere of influence that is used in physically describing the collision operator. This figure is taken from [37]. The sphere of influence can be thought

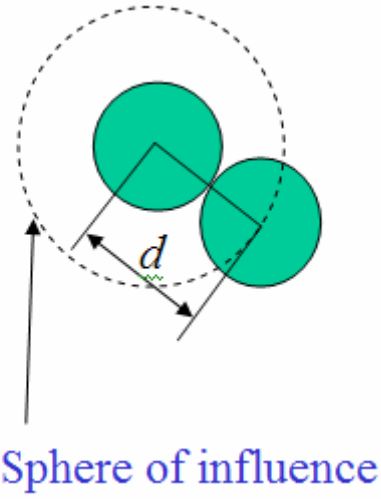

Figure 13. Sphere of Influence for Fluid Particles [37]

of as the range in which the influence of intermolecular collisions between spherical particles exists. There are multiple ways to describe collisions, but for this analysis, the use of the hard sphere model similar to colliding billiard balls is incorporated.

For a valid statistical description [37 and 38], it is further assumed that

- $N \to \infty$ The number of molecules is taken to be very large.

- $m \to 0$ The weight of each particle is taken to be extremely small compared to the total weight of the system. This allows us to describe the mass as the total system as being constant $Nm \to const$

- $d \to 0$ The size of the sphere of influence, which describes the range of intermolecular forces is taken to be extremely small such that the mean free path is constant, $\frac{1}{Nd^2} \to$ constant . Because the mean free path is finite, this limit describes the fluid as an imperfect gas. However from a strict thermodynamic sense, the fluid will be described as a perfect gas because of the Boltzmann gas limit.

Using the solid angle to define the scattering cross section, the collision operator based on the effects of depletion and replenishing hard sphere collisions can be derived. Figures 14 and 15 illustrate the replenishing and depletion collisions taking place through the scattering cross section area. These figures are taken from [37].

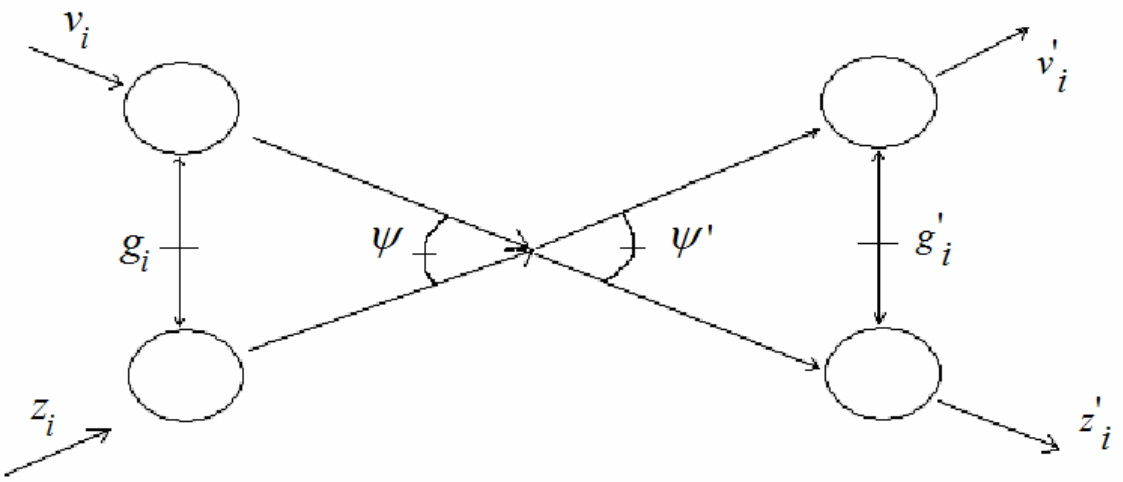

Figure 14. Binary Collision of Particles [37]

$\psi = \psi'$ because relative velocities, g_i and g_i', are the same before and after collision.

- $g_i = v_i - z_i$
- $g'_i = v'_i - z'_i$

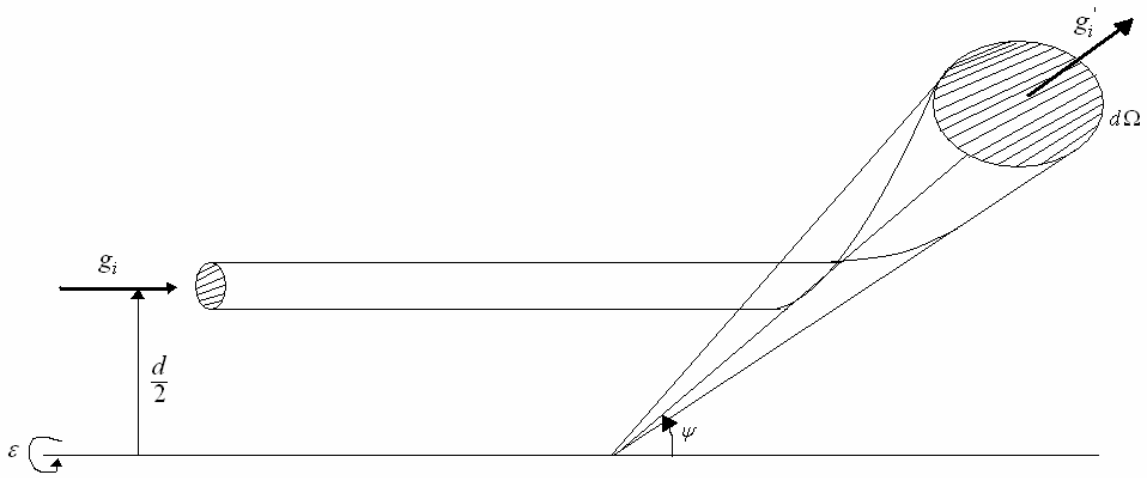

Figure 15. Scattering Cross Section Area for which Collision Takes Place [37]

In figure 15, g_i is the pre-collision relative velocity, g_i' is the post-collision relative velocity, d is the range of the interparticle collision defined by the potential or sphere of influence, ε is the azimuthal angle or the angle between the plane of collisions and a reference plane rotated around from 0 to 2π, ψ is the scattering angle or angle between the relative velocity and the line of centers, and $d\Omega$ is the solid angle, which is used to derive the area of the cross section of the scattered particles.

$d\Omega = \sin\psi d\psi d\varepsilon$ Cross sectional scattering area = $d^2 \sin\psi d\psi d\varepsilon$

Using the collision cross section, and relative velocities of colliding molecules, the following equation for the Boltzmann collision is formulated. Detail in this derivation is provided by [37].

$$\left\{\frac{\partial}{\partial t}\left[nf(v_i)\right]\right\}_{coll} = \int_{-\infty}^{\infty}\int_{0}^{2\pi}\int_{0}^{\pi/2} n^2\left[f(v_i^{'})f(Z_i^{'}) - f(v_i)f(Z_i)\right] g dP_v dV_Z \tag{2.4}$$

k is Boltzmann's constant, $dP_v = d^2 \sin\psi \cos\psi d\psi d\varepsilon$

This collision operator is validated by corresponding to the H-Theorem or entropy law, as shown below.

$$\frac{dS}{dt} = kN - kV\int_{-\infty}^{\infty}\left[1+\ln\left(\frac{h^3}{m^3}nf\right)\right]\left[\frac{\partial}{\partial t}(nf)\right]_{coll} dV_v \tag{2.5}$$

$$\frac{dS}{dt} = \frac{kV}{4}\int_{-\infty}^{\infty}\int_{-\infty}^{\infty}\int_{dP_c}\ln\left[\frac{f(v_i^{'})f(z_i^{'})}{f(v_i)f(z_i)}\right]\times n^2\left[f(v_i^{'})f(z_i^{'}) - f(v_i)f(z_i)\right] g dP_v dV_z dV_v \tag{2.6}$$

The expression of the collision operator will always be positive except for when $f(v_i^{'})f(z_i^{'}) = f(v_i)f(z_i)$. In this case, the collision operator is zero as the number of replenishing and depleting collisions are the same. Therefore it can be concluded that $\frac{dS}{dt} \geq 0$. This correctly corresponds to the definition of entropy as never decreasing but always increasing. In terms of the statistical mechanics of the Boltzmann equation, this shows that the entropy continuously increases until a state of equilibrium is reached which corresponds to $f(v_i^{'})f(z_i^{'}) = f(v_i)f(z_i)$. [37] show in greater detail how the Boltzmann collision operator satisfies H-Theorem.

The state of equilibrium is independent of time and the direction of the velocities from a distribution no longer matters. Using the condition for equilibrium along with the ideal gas law, the Maxwellian distribution is defined as follows.

$$f\left(v_i\right)=\left(\frac{m}{2\pi kT}\right)^{3/2}\exp\left[-\frac{m}{2kT}\left(v_1^2+v_2^2+v_3^2\right)\right] \tag{2.7}$$

This distribution is used to define three important molecular speeds that are very close to the value of the speed of sound.

- $v_{m,p}=\sqrt{2RT}$ (most probable speed)
- $\bar{v}=\sqrt{\frac{8RT}{\pi}}$ (average speed)
- $\sqrt{v^2}=\sqrt{3RT}$ (root-mean-square speed)

These speeds show how the energy of sound is actually transmitted through a gas by molecular collisions. These molecular speeds are important in describing thermodynamic properties of gases.

The Boltzmann equation can be more easily modeled using a linear collision operator called the Bhatnagar-Gross-Krook (BGK) collision model [37].

$$\frac{\partial nf}{\partial t}+v_j\frac{\partial nf}{\partial x_j}=\frac{n}{\lambda}(f^{(eq)}-f) \tag{2.8}$$

λ is local relaxation time, and $f^{(eq)}$ is a Maxwellian distribution.

The BGK collision retains the proper manner of decay, satisfying the H theorem. This also means that the distribution approaches a Maxwellian distribution over time. This collision operator also satisfies the zero, first, and second order moments of the Boltzmann equation.

$$\int_{-\infty}^{\infty} mn\nu\left(f^{(eq)}-f\right)dV_v=\frac{mn}{\lambda}\left[\int_{-\infty}^{\infty} f^{(eq)}dV_v-\int_{-\infty}^{\infty} fdV_v\right]=0 \tag{2.9}$$

$$\int_{-\infty}^{\infty} m v_i n\nu \left(f^{(eq)} - f \right) dV_v = mn\nu \left[\langle v_i \rangle - \langle v_i \rangle \right] = 0 \tag{2.10}$$

$$\int_{-\infty}^{\infty} \frac{1}{2} m v^2 n\nu \left(f^{(eq)} - f \right) dV_v = \frac{1}{2} mn\nu \left[\left(\langle v^2 \rangle + 3\frac{k}{m}T \right) - \left(\langle v^2 \rangle + 3\frac{k}{m}T \right) \right] = 0 \tag{2.11}$$

Using the Boltzmann equation, the assumptions of the Boltzmann limit, and the BGK collision operator; the proper conservation equations of particle density, momentum, and energy can be obtained. These equations show that the kinetic description of molecules can retain the governing equations of particle motion and interaction.

3. Macroscopic Description of Fluid Particles

By using the Chapman-Enskog expansion [37] (to be described later) and summing up the particle densities and velocities, the macroscopic equations of continuity, momentum, and energy are obtained.

$$\frac{\partial \rho}{\partial t} + \nabla \cdot (\rho \mathbf{v}) = 0 \tag{2.12}$$

$$\frac{\partial \rho \mathbf{v}}{\partial t} + \mathbf{v} \nabla \cdot \rho \mathbf{v} = -\nabla p - \nabla \cdot \bar{\boldsymbol{\pi}} \tag{2.13}$$

$$\frac{3}{2}\frac{\partial}{\partial t}(\rho kT) + \frac{3}{2}\mathbf{v} \cdot \nabla (\rho kT) + \rho kT \nabla \cdot \mathbf{v} = -\bar{\boldsymbol{\pi}} : \nabla \mathbf{v} - \nabla \cdot \mathbf{h} \tag{2.14}$$

The constitutive relationships for the viscous stress tensor and heat flux are defined as the following:

$$\bar{\boldsymbol{\pi}} = \mu \nabla \mathbf{v} \tag{2.15}$$

$$\mathbf{h} = -\kappa \nabla (kT) \tag{2.16}$$

Where μ is the absolute viscosity, κ is the thermal conductivity, and *k* is the Boltzmann constant.

Pressure is defined thermodynamically as

$$p_\alpha = \frac{1}{3} Tr\left(\mathbf{P}_\alpha\right) = \frac{1}{3} n_\alpha m_\alpha \left\langle \overset{\sim 2}{v_\alpha} \right\rangle = n_\alpha k T_\alpha \tag{2.17}$$

C Conclusion

The molecular descriptions and formulations of this chapter provide the well known kinetic and hydrodynamic fundamentals. In kinetic plasma theory, these fundamentals are still important, but they are modified by the electromagnetic properties of plasma. The next chapter will explain electromagnetic theory fundamentals, along with kinetic plasma theory, and MHD. The formulation of kinetic plasma theory and MHD will be closely related to the kinetic theory description of fluid particles.

CHAPTER III

ELECTROMAGNETIC THEORY

A. Introduction

This chapter overviews the important theoretical concepts concerning electromagnetic theory. Each atom is made up of nuclei, containing neutrons and protons, surrounded by electrons. The presence of these positive and negative charges generates electromagnetic forces. The effects are separated into that of an electric and magnetic field.

B. The Electric Charge

Electric charges are defined from the positively charged protons and negatively charged electrons. These charges exert forces on each other through the presence of the electric and magnetic fields generated by the charges. As will be explained later, the electric and magnetic fields exist due to the interaction of charges. The following highlights fundamental properties of electric charges [39].

- Charges exist in positive and negative varieties. Overall, the negative and positive charges exist in negligibly equal amounts causing most matter to be neutralized.
- The total charge of the universe is fixed for all time. This is the global conservation of charge that, similar to matter, can not be created or destroyed.

$$\frac{\partial \rho_0}{\partial t} + \nabla \cdot \rho_0 \mathbf{v} = 0 \tag{3.1}$$

C. Stationary Charges and Electric field phenomena

An electric field is a force emitted by a certain amount of a charge acting on objects around it. The strength of the point charge's electric field is related to the charge distribution and the inverse square of the distance from the charge (similar to gravitational force).

$$\mathbf{E} = \frac{1}{4\pi\varepsilon_0}\frac{q}{r^2}\mathbf{r} \tag{3.2}$$

$$\mathbf{F} = \frac{1}{4\pi\varepsilon_0}\frac{qQ}{r^2}\mathbf{r} = Q\mathbf{E} \quad \text{Coulombs Law} \tag{3.3}$$

Where ε_0 is the permittivity of free space, q the emitting point charge, Q the test charge, and r the distance between the emitting and test charges. From these equations, the type of electric field ($\mathbf{E}$) and force ($\mathbf{F}$) exerted by charges can be easily deduced. Coulomb's Law shows that opposite charges attract one another (negative sign of the force term), and that like charges repel each other (positive sign of force term). This effect can be used in understanding the electric field, as opposite charges emit electric fields that connect to one another.

The characteristics of the electric field lines indicate that they never cross one another. Electric field lines must always begin on positive charges and end on negative ones. Defining the rate of the flux of the electric field as being proportional to the number of electric field lines passing through an infinitesimal area, the flux through any closed surface is the total amount of charge inside the close surface [39]. This is known as Gauss's Law.

$$\mathbf{E} = k\frac{q}{r^2}\mathbf{r} \qquad \mathbf{E}\cdot d\mathbf{S} = kq\frac{r}{r}\frac{dS}{r^2} = kqd\Omega$$

$$d\mathbf{S} = \mathbf{n}dS \qquad d\Omega = \frac{dS}{r^2} \quad \text{from solid angle geometry}$$

$$\int_S \mathbf{E}\cdot d\mathbf{S} = \int kqd\Omega = kq(4\pi) = \frac{q}{\varepsilon_0} \qquad \int_S \mathbf{E}\cdot d\mathbf{S} = \frac{q}{\varepsilon_0} \quad \text{Gauss's Law} \qquad (3.4)$$

From these descriptions of the electric field, the divergence and curl properties can be shown.

The following is the derivation of Maxwell's 1st equation [39] that relates the charge distribution to the electric field over a closed surface by using the divergence theorem.

$$4\pi k\sum_i q_i = 4\pi k\int_v \rho d\tau$$

$$\int_S \mathbf{E}\cdot d\mathbf{S} = \int_v \nabla\cdot\mathbf{E}d\tau = 4\pi k\int_v \rho d\tau \quad \text{from divergence theorem}$$

$$\nabla\cdot\mathbf{E} = 4\pi k\rho_0 = \frac{\rho_0}{\varepsilon_0}$$

$$\nabla\cdot\mathbf{E} = \frac{\rho_0}{\varepsilon_0} \quad \text{Maxwell's 1st equation} \qquad (3.5)$$

An important property of stationary charges is that over a closed system, the charges neutralize each other leading to a zero net value of the total electric field or work done by the total electric field.

$$\mathbf{E}\cdot d\mathbf{l} = k\frac{q}{r^2}dr \rightarrow kq\int_{r_a}^{r_b}\frac{1}{r^2}dr = -kq\frac{1}{r}\Big|_{r_a}^{r_b} = kq\left(\frac{1}{r_a}-\frac{1}{r_b}\right) = 0\,, \text{ as } r_a = r_b$$

This derivation was performed using spherical coordinates $d\mathbf{r} = dr\mathbf{r} + rd\theta\boldsymbol{\theta} + rsin\theta d\phi\boldsymbol{\phi}$ [39]. From the previous result, using Stokes Theorem, the initial form of Maxwell's 2nd equation for stationary charges is formulated.

$$\oint_{\Sigma}\mathbf{E}\cdot d\mathbf{l} = \oint_{\partial\Sigma}(\nabla\times\mathbf{E})\cdot d\Sigma = 0$$

$\nabla \times \mathbf{E} = 0$ Initial form of Maxwell's 2nd equation (3.6)

D. Steady Currents and Magnetic Induction

A moving charge produces a magnetic induction field **B** and feels the effect of the magnetic fields produced by other moving charges. The magnetic induction field describes the force acting on a charge q that moves with velocity **v**.

$\mathbf{F} = q(\mathbf{v} \times \mathbf{B})$ Lorentz force law (3.7)

While in the presence of both electric and magnetic fields, the net force on a charge q is

$$\mathbf{F} = q\left[\mathbf{E} + (\mathbf{v} \times \mathbf{B})\right]. \quad (3.8)$$

This is a fundamental axiom of electromagnetic theory that has been justified from experiments [39].

Current refers to a flow of charges. Current is defined in terms of moving charges as follows.

$$\mathbf{j} = \rho_0 \mathbf{v} \qquad \mathbf{I} = \int \mathbf{j} d\tau$$

Where $\mathbf{j}$ is the current density; $\mathbf{I}$ is the current, and $d\tau$ is the infinitesimal area. Current and current density are related to the Lorentz force law by defining it as a line integral of the charge per unit length and the surface integral of charge per unit area [39].

$$\mathbf{F} = \int (\mathbf{v} \times \mathbf{B}) dq = \int (\mathbf{v} \times \mathbf{B}) \lambda dl = \int (\mathbf{I} \times \mathbf{B}) dl \qquad \mathbf{F} = I \int (d\mathbf{l} \times \mathbf{B})$$

$$\mathbf{F} = \int (\mathbf{v} \times \mathbf{B}) dq = \int (\mathbf{v} \times \mathbf{B}) \rho_0 d\tau = \int (\mathbf{j} \times \mathbf{B}) d\tau \qquad \mathbf{F} = \int (\mathbf{j} \times \mathbf{B})\, d\tau$$

The current density is more specifically defined as the current per unit area perpendicular to the flow.

$$\mathbf{j} = \frac{dI}{da_\perp}$$

From this definition of current density,

$$dI = \mathbf{j} da_\perp \rightarrow I = \int_S j da_\perp = \int_S \mathbf{j} \cdot d\mathbf{a} = \int_V (\nabla \cdot \mathbf{j}) d\tau \quad \text{(Gauss Divergence Theorem).}$$

Taking into account that charges are conserved the continuity equation of charges can be recovered.

$$\int_V (\nabla \cdot \mathbf{j}) d\tau = -\frac{\partial}{\partial t} \int_V \rho_0 d\tau = -\int_V \left(\frac{\partial \rho_0}{\partial t} \right) d\tau \Rightarrow \nabla \cdot \mathbf{j} = -\frac{\partial \rho_0}{\partial t}$$

$$\Rightarrow \frac{\partial \rho_0}{\partial t} + \nabla \cdot \rho_0 \mathbf{v} = \mathbf{0} \qquad (3.1)$$

This will hold true only for steady currents or stationary charges.

With the Lorentz force being defined in terms of the current, a useful relationship in defining the magnetic field by assuming a steady current can be obtained. This relationship is called the Biot-Savart Law. The following equation shows various forms of the Biot-Savart Law.

$$\mathbf{B} = \frac{\mu_0 I}{4\pi} \int \frac{d\mathbf{l} \times \mathbf{r}}{|\mathbf{r}|^3} = \frac{\mu_0}{4\pi} \int \frac{\mathbf{I} \times \mathbf{r}}{r^2} dl = \frac{\mu_0}{4\pi} \int \frac{\mathbf{j} \times \mathbf{r}}{r^2} d\tau \qquad (3.9)$$

This is a good approximation that has been verified to have good accuracy. It is, however, true that there is no such thing as steady current, so it should be understood that the Biot-

Savart law is a good estimation used to solve for the magnetic field under the condition of a negligibly steady current.

An important property of the magnetic field is that it is solenoidal. Thus the divergence theorem and Gauss' law for the flux of the magnetic field yield

$\nabla \cdot \mathbf{B} = 0$ Maxwell's 3rd Equation (3.10)

This means that there are no magnetic monopoles or that the magnetic field lines form a closed loop. All known testing thus far validates this property of magnetic fields. This equation is the third of the governing Maxwell's equations of electromagnetic theory. The Biot-Savart Law can be used to find a new relationship between the magnetic field and the current density. By solving the Biot-Savart Law for a closed current loop, we arrive at the new relation [39].

$$B = \frac{\mu_0 I}{2\pi s} \qquad \oint B \cdot dl = \frac{\mu_0 I}{2\pi} \oint \frac{1}{s} s d\phi = \frac{\mu_0 I}{2\pi} \int_0^{2\pi} d\phi = \mu_0 I$$

However, from Stokes theorem

$$\int (\nabla \times \mathbf{B}) \cdot d\mathbf{a} = \oint \mathbf{B} \cdot d\mathbf{l} = \mu_0 I = \mu_0 \int \mathbf{j} \cdot d\mathbf{a}$$

$\nabla \times \mathbf{B} = \mu_0 \mathbf{j}$ initial form of Maxwell's 4th Equation (3.11)

Where μ_0 is magnetic permeability. This equation only holds true for the case of a steady current and corresponds to the continuity equation of charges. It can be shown that if the charge density does change with time that this relationship no longer holds.

$$\nabla \cdot \mathbf{j} = -\frac{\partial \rho_0}{\partial t} \qquad \int_V \nabla \cdot \mathbf{j} = \int dS \mathbf{n} \cdot \mathbf{j} = -\frac{d}{dt} \int \rho_0 d\tau = -\frac{d}{dt} q \qquad \nabla \cdot \nabla \times \mathbf{B} = 0 = \mu_0 \nabla \cdot \mathbf{j}$$

For the case that $\frac{\partial \rho_0}{\partial t} \neq 0$, the current density must be modified as $\mathbf{j} + \mathbf{j}_D$, where $\mathbf{J}_D$ is a *displacement* current that accounts for the way a changing electric field causes a magnetic field [39].

$$\nabla \cdot \mathbf{j}_D = -\nabla \cdot \mathbf{j} = \frac{\partial \rho_0}{\partial t}$$

Next, Maxwell's 1st equation (3.5) is used to get the following.

$$\nabla \cdot \mathbf{E} = \frac{\rho_0}{\varepsilon_0} \quad (18) \qquad \nabla \cdot \mathbf{j}_D = \frac{1}{\varepsilon_0}\frac{\partial}{\partial t}\left(\nabla \cdot \mathbf{E}\right) \qquad \nabla \cdot \frac{1}{\varepsilon_0}\frac{\partial \mathbf{E}}{\partial t} = \nabla \cdot \mathbf{j}_D \qquad \mathbf{j}_D = \frac{1}{\varepsilon_0}\frac{\partial \mathbf{E}}{\partial t}$$

The equation for $\mathbf{j}_D$ has also been experimentally verified [39].

Adding the term of $\mathbf{j}_D$ to the current density ($\mathbf{j}$) in $\nabla \times \mathbf{B} = \mu_0 \mathbf{j}$, we obtain Maxwell's 4th equation.

$$\nabla \times \mathbf{B} = \mu_0 \mathbf{j} + \frac{\mu_0}{\varepsilon_0}\frac{\partial \mathbf{E}}{\partial t} \qquad (3.12)$$

This equation enhances the previous form of Maxwell's 4th (3.11) equation by showing that a changing electric field induces a magnetic field. This effect will only be taken into account for relativistic flows $\left(v^2 / c_L^2\right) \gg 1$. v is the velocity of the object or particle, and c_L is the speed of light. Therefore, the electric field term of (3.12) will be negligible for most cases. The initial form of Maxwell's 4th equation is used mostly except in the area of electromagnetic waves.

E. Electromotive Force and Maxwell's Equations

Now, a description of how an electric field affects moving charges is discussed. Charges move due to an electromotive force that is created from a difference in charges. Electromotive force is exhibited in batteries, in terms of the voltage, as a chemical reaction corresponds to the movement of charges. This process takes place until the electric field becomes strong enough to prevent the reaction. The current is the driving mechanism behind the electromotive force. In this context, the current density is defined as being proportional to the force per unit charge, $\mathbf{f}$.

$$\mathbf{j} = \frac{1}{\eta}\mathbf{f} \tag{3.13}$$

$$\mathbf{j} = \frac{1}{\eta}\left(\mathbf{E} + \mathbf{v}\times\mathbf{B}\right) \quad \text{Ohm's Law} \tag{3.14}$$

The electromotive force is defined as the following.

$$\varepsilon = \oint \mathbf{f}\cdot d\mathbf{l} = -\int_a^b \mathbf{E}\cdot d\mathbf{l}$$

This description can be directly related to a moving current loop due to the Lorentz force (qvB).

$\varepsilon = \oint \mathbf{f}\cdot d\mathbf{l} = vBh$ where v is the velocity of the current loop and h is a length scale distance between the opposing potentials that induce the electromotive force. From this relationship, a flux term is defined that provides an equation expressing the electromotive force in terms of the magnetic field [39]. For a rectangular current loop the following flux would be calculated.

$$\Phi = \int \mathbf{B}\cdot d\mathbf{a} = Bhx \qquad \frac{d\Phi}{dt} = \frac{d}{dt}\int \mathbf{B}\cdot d\mathbf{a} = Bh\frac{dx}{dt} = -Bhv$$

This shows how the velocity will decrease with time corresponding to a decrease in the flux as well. This provides a comparison between the magnetic flux and the electromotive force.

$$\varepsilon = -\frac{d\Phi}{dt}$$

This relationship applies for case of non-rectangular current loops or even loops with no fixed shape. From this, we arrive with the relationship between the electric and magnetic fields.

$$\oint \mathbf{E} \cdot d\mathbf{l} = -\int \frac{\partial \mathbf{B}}{\partial t} \cdot d\mathbf{a} \rightarrow \int (\nabla \times \mathbf{E}) \cdot da = -\int \frac{\partial \mathbf{B}}{\partial t} \cdot d\mathbf{a}$$

$$\nabla \times \mathbf{E} = -\frac{\partial \mathbf{B}}{\partial t} \quad \text{final form of Maxwell's 2}^{\text{nd}}\text{ equation} \tag{3.15}$$

This final form of Maxwell's 2nd equation demonstrates that a temporally changing magnetic field induces an electric just as a changing electric field will induce a magnetic field.

The following are the final set of Maxwell's Equations.

$$\nabla \cdot \mathbf{E} = \frac{\rho_0}{\varepsilon_0} \tag{3.5}$$

$$\nabla \times \mathbf{E} = -\frac{\partial \mathbf{B}}{\partial t} \tag{3.15}$$

$$\nabla \cdot \mathbf{B} = 0 \tag{3.10}$$

$$\nabla \times \mathbf{B} = \mu_0 \mathbf{j} + \frac{\mu_0}{\varepsilon_0} \frac{\partial \mathbf{E}}{\partial t} \tag{3.12}$$

F. Lorentz Force and the Maxwell's Stress Tensor

As previously described by the Lorentz force law, a moving charge exerts an electric and magnetic force on other charges [39].

$$\mathbf{F} = \int \left(\rho_0 \mathbf{E} + \mathbf{j} \times \mathbf{B}\right) d\tau \qquad \mathbf{f}_v = \rho_0 \mathbf{E} + \mathbf{j} \times \mathbf{B} \text{ (force per unit volume)}$$

By using Maxwell's equations, the force per unit volume can be redefined as

$$\mathbf{f}_v = -\frac{1}{2}\nabla\left(\varepsilon_0 E^2 + \frac{1}{\mu_0} B^2\right) - \varepsilon_0 \frac{\partial}{\partial t}\left(\mathbf{E} \times \mathbf{B}\right) \tag{3.16}$$

This equation presents two different phenomena that can be simplified into terms of the Maxwell's stress tensor and the Poynting vector. Taking the first term on the right side, the Maxwell's stress tensor can be further described as follows.

$$\frac{1}{2}\nabla\left(\varepsilon_0 E^2 + \frac{1}{\mu_0} B^2\right) = \nabla \cdot \overleftrightarrow{\mathbf{T}} \tag{3.17}$$

$$\overleftrightarrow{T}_{ij} = \varepsilon_0\left(E_i E_j - \frac{1}{2}\delta_{ij} E^2\right) + \frac{1}{\mu_0}\left(B_i B_j - \frac{1}{2}\delta_{ij} B^2\right) \tag{3.18}$$

$-\frac{\varepsilon_0}{2}\delta_{ij} E^2 - \frac{1}{2\mu_0}\delta_{ij} B^2$ (pressure) $\qquad\qquad$ $\varepsilon_0 E_i E_j + \frac{1}{\mu_0} B_i B_j$ (tension)

The Maxwell's stress tensor is further defined in terms of the electromagnetic pressure and electromagnetic tension. The electromagnetic pressure term accounts for normal forces like pressure, while the electromagnetic tension term accounts for tangential or shear forces. In MHD, the electric field influence is insignificant, therefore the final form of the Maxwell's stress tensor used in this paper is the following.

$$\overleftrightarrow{T}_{ij} = \frac{1}{\mu_0}\left(B_i B_j - \frac{1}{2}\delta_{ij} B^2 \right) \tag{3.19}$$

Assuming the Poynting vector to be insignificant, the Lorentz force is also defined as the Maxwell's stress divergence term in vector notation as follows.

$$(\mathbf{j}\times\mathbf{B}) = -\nabla\left(\frac{B^2}{2\mu_0}\right) + \frac{1}{\mu_0}(\mathbf{B}\cdot\nabla)\mathbf{B}$$

Magnetic tension acts parallel to the magnetic field lines. In application to magnetohydrodynamics, magnetic field lines can be described as being in tension exerting an elastic stress on a fluid. The magnetic tension term can be broken down into a normal and tangential component in reference to the fluid surface.

$$\frac{1}{\mu_0}(\mathbf{B}\cdot\nabla)\mathbf{B} = \frac{\partial}{\partial \mathbf{s}}\left(\frac{B^2}{2\mu_0}\right)\mathbf{e}_t - \frac{B^2}{\mu_0 R}\mathbf{e}_n \tag{3.20}$$

$\mathbf{e}_t$ is the tangential component, and $\mathbf{e}_n$ is the normal component.

Figure 16 visualizes the magnetic tension in the magnetic field lines, illustrated as a flux tube. Figure 17 shows the adverse affect that transverse magnetic field lines of strong magnetic tension can have on moving fluid particle of velocity, u. These figures are taken from [5].

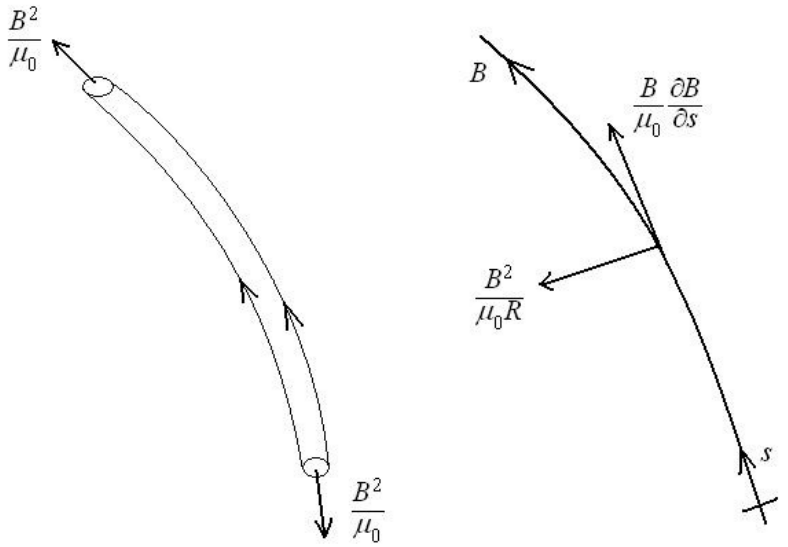

Figure 16. Magnetic Flux Tube Description [5]

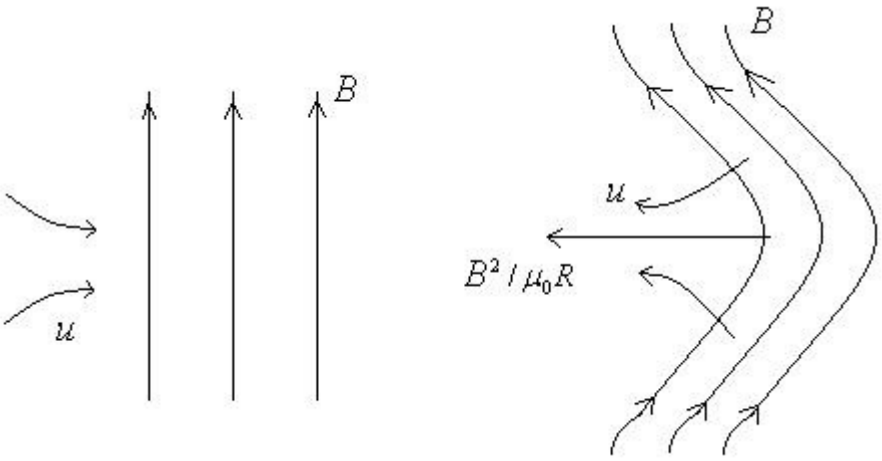

Figure 17. Illustration of Adverse Reactionary Magnetic Tension Force [5]

When a fluid particle's motion opposes the direction of the magnetic field line, the magnetic field line deforms. When this deformation occurs, the magnetic tension produces a reactionary force, slowing down the moving particle.

Metaphorically, the elastic magnetic fields lines can be thought of as rubber bands. As the velocity field attempts to flow through the magnetic field lines, the magnetic field lines bend and stretch like a rubber band would. As they stretch, the magnetic field strength also increases. Depending on the strength of the magnetic tension, the magnetic field lines stretch greatly or almost not at all. As the magnetic field line bends, it exerts an adverse reactionary force on the flow, resisting the velocity field's deformation effect.

The second term on the right side of the (3.16) is defined in terms of the Poynting vector.

$$\varepsilon_0 \frac{\partial}{\partial t}(\mathbf{E}\times\mathbf{B}) = \varepsilon_0\mu_0 \frac{\partial \mathbf{S}}{\partial t} \qquad \mathbf{S} = \frac{1}{\mu_0}(\mathbf{E}\times\mathbf{B}) \tag{3.21}$$

This term does not relate to momentum in as much of a physical manner as the Maxwell's stress tensor. The momentum generated by the temporal change in the Poynting vector is another form of momentum that is transported by the electromagnetic fields. The Poynting vector is the energy flux density created by the interaction of the intersecting electric and magnetic fields. Physically, this term has the effect of creating secondary drift motions in charges.

G. Energy Conservation and Poynting's Theorem

Both electric and magnetic fields contain energy necessary to assemble a charge distribution and move currents.

$$e_E = \frac{\varepsilon_0}{2}\int E^2 d\tau \qquad e_B = \frac{1}{2\mu_0}\int B^2 d\tau \qquad e_T = \int\left(\frac{\varepsilon_0 E^2}{2} + \frac{B^2}{2\mu_0}\right)d\tau$$

By taking the work done by the electromagnetic force, it is shown that the magnetic field does not contribute [39].

$$\mathbf{F}\cdot d\mathbf{l} = q\left[\mathbf{E}+\left(\mathbf{v}\times\mathbf{B}\right)\right]\cdot \mathbf{v}dt = q\mathbf{E}\cdot\mathbf{v}dt \qquad \frac{dW}{dt} = \int_V \left(\mathbf{E}\cdot\mathbf{j}\right)d\tau$$

Physically, this demonstrates that forces due to magnetic fields produce no work. This a difficult intuitive concept, however, it means that magnetic fields manipulate the directionality of forces instead of providing an additional force. By redefining $\mathbf{E}\cdot\mathbf{j}$ using the relations of Maxwell's equations, the equation for the rate at which work is rewritten to display Poynting's Theorem.

$$\frac{dW}{dt} = \frac{d}{dt}\int_V \left(\varepsilon_0 E^2 + \frac{1}{\mu_0}B^2\right)d\tau - \frac{1}{\mu_0}\oint_S \left(\mathbf{E}\times\mathbf{B}\right)\cdot d\mathbf{a} \tag{3.22}$$

This theorem states that the work done on the charges by the electromagnetic force is equal to the decrease in energy stored in the field, less the energy that flowed out through the surface [39].

H. Magnetic Induction Equation

The Maxwell's equations form the primary governing equations of electric and magnetic fields. From these equations, a more simplified set of governing equations for the magnetic field can be defined with the proper assumptions. The four equations, essential to this process are Maxwell's 2nd (3.15), Maxwell's 4th (3.12), Maxwell's 3rd (3.10), and Ohm's Law (3.14).

First, Maxwell's 4th equation is simplified to it's initial form (3.11) with the assumption of non-relativistic flows $\left(v^2/c_L^2\right) \ll 1$. This provides an equation for the current density. Then, an equation for the electric field, using Ohm's Law (3.14), is substituted into Maxwell's 2nd equation (3.15). This gives the magnetic induction equation.

$$\nabla\times\left(\mathbf{v}\times\mathbf{B}-\eta\mathbf{j}\right)=-\frac{\partial\mathbf{B}}{\partial t}$$

$$\Rightarrow\nabla\times\left(\mathbf{v}\times\mathbf{B}-\frac{\eta}{\mu_0}\nabla\times\mathbf{B}\right)=-\frac{\partial\mathbf{B}}{\partial t}$$

$$\frac{\partial\mathbf{B}}{\partial t}+\mathbf{v}\cdot\nabla\mathbf{B}=\mathbf{B}\cdot\nabla\mathbf{v}+\frac{\eta}{\mu_0}\nabla^2\mathbf{B} \tag{3.23}$$

$$\nabla\cdot\mathbf{B}=0 \tag{3.10}$$

Maxwell's 3rd equation (3.10) combines with the magnetic induction equation (3.23) to form a new set of governing magnetic field equations. It is important to note that the assumption of non-relativistic flows and use of Ohm's Law facilitates this assumption. These equations will be important later on in the development of the magnetohydrodynamic (MHD) equations.

I. Conclusion

The governing equations, describing how the electric and magnetic fields are related to momentum and energy, relate the interaction between electromagnetic theory and hydrodynamics. Maxwell's equations demonstrate how the evolution of electric and magnetic fields induced by a charge are related to each other along with the charge's velocity. The Lorentz force and energy equation show how electric and magnetic fields manipulate the movement of charges. This relationship is vital in understanding kinetic plasma theory and magnetohydrodynamics.

CHAPTER IV

KINETIC PLASMA THEORY AND THE MAGNETOHYDRODYNAMIC EQUATIONS

A. Introduction

This chapter overviews the important theoretical concepts of kinetic plasma theory and magnetohydrodynamics. The kinetic theory principles discussed in chapter II and the electromagnetic theory concepts in chapter III are used to describe kinetic plasma theory. The kinetic plasma modeling equations are derived and simplified for application in magnetohydrodynamics.

B. Kinetic Plasma Theory

There are three different theoretical models in plasma dynamics [6].

- Single Particle Motion is a model that tracks the motion of an individually charged particle in electric and magnetic fields.
- Kinetic Plasma Theory describes plasma as a collection of particles by the use of particle distributions.
- Fluid Theory describes plasmas in terms of averaged macroscopic functions of position and time. This is the model of magnetohydrodynamics.

The single particle motion model will not be of interest because this model is only useful for low densities such that interaction between particles can be ignored. The Kinetic Plasma Theory is of great interest along with its relationship to the magnetohydrodynamic model. In the previous chapter, fundamental elements of kinetic theory were described and the Boltzmann equation was used to describe fluid particle distributions. This distribution function is also used to describe charged particle distributions. It is important to understand that this is a statistical approach to describing

the collective behavior of charged particles. The Boltzmann equation for charged particles is as follows.

$$\frac{\partial f_\alpha}{\partial t} + \mathbf{v}\cdot\frac{\partial f_\alpha}{\partial \mathbf{r}} + \frac{q_\alpha}{m_\alpha}\left(\mathbf{E}+\mathbf{v}\times\mathbf{B}\right)\cdot\frac{\partial f_\alpha}{\partial \mathbf{v}} = \left(\frac{\partial f_\alpha}{\partial t}\right)_{coll} \tag{4.1}$$

This includes the previous form shown in chapter II along with an external forcing term, provided by the Lorentz force law. With the Lorentz force included, this equation describes not only internal collision effects but long range electromagnetic interactions. The effect of Lorentz body forces has been explained through the Maxwell's stress tensor and Poynting vector. An important focus, of kinetic plasma theory, is modeling the collision forces in plasmas. The collision forces, aside from accounting for viscous forces, must include effects from Coulomb interactions, momentum transfer between charged particles, and heat transfer between charged particles.

1. Plasma Description

Plasma is an ionized gas, consisting of positive ions, electrons, and neutral particles, that exhibits collective behavior and is electrically neutral over the macroscopic length scale. A gas becomes ionized whenever the temperature becomes large enough to excite the extreme modes of intermolecular forces. For example, vibrational and electronic intermolecular forces cause electrons and ions to separate. Figure 18 illustrates this process.

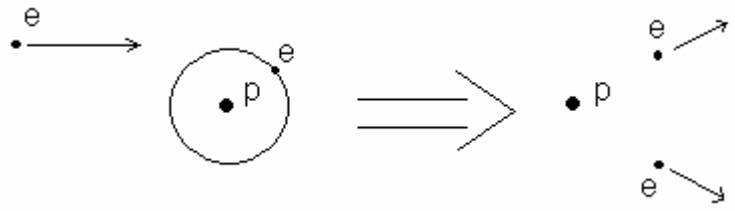

Figure 18. Ionization of a Gas Molecule

Plasma is in a state of nearly 100% ionization, implying that the threshold energy, for which recombination no longer occurs, has been reached. Because plasmas are considered to be a mixture of electrons, ions, and neutrals, the density, momentum, pressure, charge density, and current density are calculated by summations over the species (α) :

$$\rho = \sum_{\alpha} \rho_{\alpha} \tag{4.2}$$

$$\rho \mathbf{u} = \sum_{\alpha} \rho_{\alpha} \mathbf{u}_{\alpha} \tag{4.3}$$

$$p = \sum_{\alpha} p_{\alpha} \tag{4.4}$$

$$\rho_0 (\mathbf{r}, t) \equiv \sum q_{\alpha} n_{\alpha} \tag{4.5}$$

$$\mathbf{j}(\mathbf{r}, t) \equiv \sum q_{\alpha} n_{\alpha} \mathbf{u}_{a} \,. \tag{4.6}$$

In normal gases, neutral molecules move about freely until a collision occurs, which is modeled by short range binary collisions. In plasmas, consisting of oppositely charged molecules, long-range Coulomb interactions occur due to the electromagnetic forces. The characteristics, of individual charged particles influenced by electromagnetic fields at the microscopic level, are described by the following.

- The motion of a charged particle, accounting for magnetic effects, is governed by the following equations [6]. Figure 19, illustrates this model.

$$\frac{d\mathbf{v}}{dt} = \frac{\mathrm{q}}{\mathrm{m}} (\mathbf{v} \times \mathbf{B}) \qquad \ddot{x} - \frac{qB}{m} \dot{y} = 0 \qquad \ddot{y} - \frac{qB}{m} \dot{x} = 0 \tag{4.7}$$

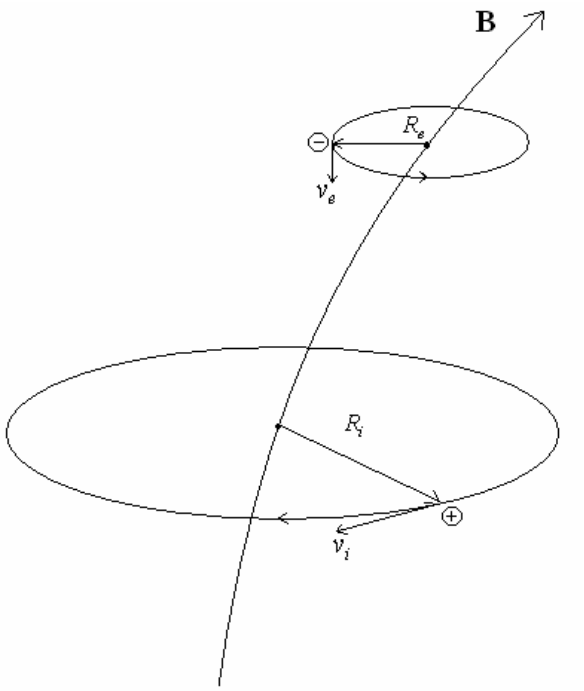

Figure 19. Charged Particle Motion Around a Magnetic Field [6]

The cyclotron frequency of the charged particle around a magnetic field is

$$\Omega_\alpha = \frac{q_\alpha B}{m_\alpha} , \tag{4.8}$$

and the Larmor radius of the charged particle is

$$R_\alpha = \frac{v_\alpha}{\Omega_\alpha} . \tag{4.9}$$

Using the thermal speed to characterize the velocities, the Larmor radius is

$$R_\alpha = \frac{\left(2km_\alpha T_\alpha\right)^{1/2}}{q_\alpha B} . \tag{4.10}$$

Because the mass of ions is much larger than electrons $\Omega_e \gg \Omega_i$ and $R_i \gg R_e$. These parameters are important in determining the magnetic field affecting the charged particle. This description of charged particles also corresponds to the single particle motion model.

- The motion of a charged particle, accounting for only electric effects, is described by the continuity and momentum equations [6].

$$\frac{d\mathbf{v}_\alpha}{dt} = \frac{q_\alpha}{m}\mathbf{E} \qquad \frac{\partial n_\alpha}{\partial t} = -n_\alpha \nabla \cdot \mathbf{v}_\alpha \qquad \varepsilon_0 \nabla \cdot \mathbf{E} = \sum_\alpha n_\alpha q_\alpha \tag{4.11}$$

As stated earlier, with the mass of the ion being much larger than that of the electron, the frequency of the electron will be much larger. The average number of electrons is also taken to be equal to that of ions (n_0) with a perturbation in the number of electrons (n_1) accounted for in characterizing oscillations. The perturbed number of electrons is much less than that of the average number. The electric field created by the perturbation is denoted by $\mathbf{E}_1$ as it is localized to a small area. The equations can be simplified by these assumptions to obtain the plasma frequency (ω_{pe}) associated with plasma oscillations [6].

$$n_e = n_0 + n_1(\mathbf{r},t) \qquad \mathbf{u}_e(\mathbf{r},t) = \mathbf{u}_1(\mathbf{r},t) \qquad \frac{\partial n_1}{\partial t} = -n_0 \nabla \cdot \mathbf{u}_1$$

$$q_e \nabla \cdot \mathbf{E_1} = \frac{q_e^2}{\varepsilon_0} n_1 \qquad \frac{d}{dt}(\nabla \cdot \mathbf{u}_1) = \frac{\mathrm{q}_e}{\mathrm{m_e}}(\nabla \cdot \mathbf{E_1}) \qquad \frac{\partial^2 n_1}{\partial t^2} + \omega_{pe}^2 n_1 = 0$$

$$\omega_{pe} = \left(\frac{n_0 q_e}{\varepsilon_0 m_e}\right)^{1/2} \tag{4.12}$$

The plasma frequency is a fundamental parameter of plasma that allows for the determination of plasma density.

- As stated earlier, plasmas maintain charge neutrality, however, at lower length scales oscillations in the electric field can occur that create charge imbalances. The length at which these imbalances take effect is called the Debye length.

$$\lambda_D = \sqrt{\frac{\varepsilon_0 k T_e}{n_0 q_e^2}} = \frac{v_e}{\sqrt{2}\omega_{pe}} \tag{4.13}$$

At length scales larger than the Debye length, the effects of electric field oscillations are negligible, meaning that charge neutrality is maintained.

Figure 20, provides plasma parameters for different applications [32 and 40]. The variable, *L*, is a characteristics length scale size for that system. In the more practical

Plasma	n_e (m^{-3})	T (K)	B (T)	λ_D (m)	N_D	ω_{pe} (s^{-1})	Ω_e (s^{-1})	R_e (m)	L (m)
VASIMR	10^{18}	10^4	0.565	10^{-4}	10^4	10^{10}	10^9	10^{-4}	0.05
Tokamak	10^{20}	10^8	10	10^{-4}	10^8	10^{12}	10^{12}	10^{-5}	5.0
Ionosphere	10^{12}	10^3	10^{-5}	10^{-3}	10^5	10^8	10^6	10^{-1}	—
Magnetosphere	10^7	10^7	10^{-8}	10^2	10^{10}	10^5	10^3	10^4	—
Solar core	10^{32}	10^7	—	10^{-11}	1	10^{18}	—	—	—
Solar wind	10^6	10^5	10^{-9}	10	10^{11}	10^5	10^2	10^4	—
Interstellar medium	10^5	10^4	10^{-10}	10	10^{10}	10^4	10	10^4	—
Intergalactic medium	1	10^6	—	10^5	10^{15}	10^2	—	—	—

Figure 20. Plasma Parameters in different Applications [32 and 40]

engineering applications, pertaining to VASIMR [33] and tokomaks [6], the characteristic length scale is much larger than the Debye length scale and Larmor radius. In these cases, as will be discussed in the MHD approximation, quasi charge neutrality is maintained.

These parameters are important in characterizing electromagnetic field effects on charged particles and plasmas at small length scales. The gyration effects by the magnetic field on charged particles are averaged out and not accounted for at macroscopic length scales. The Debye length describes the necessary size in order for oscillations in the electric field, characterized by the plasma frequency, to be an insignificant factor (quasi charge neutrality). This length scale is very important in deriving out relationships with plasmas on the macroscopic level.

2. Fokker-Planck Collision Operator

a. Coulomb Collisions in Plasmas

The Fokker-Planck collision operator describes the charged particle collisions by accounting for long range Coulomb effects [41]. This long range effect is the difference in describing the collision between charged particles versus fluid particles.

Part (a) of figure 21 shows the typical trajectory of a charged particle in a plasma, while part (b) shows the typical trajectory of a particle in a normal fluid. The important difference to note from the figure is that the velocity deflections are much smaller for particles in a plasma than particles in a normal fluid. The reason for this difference is due to long range Coulomb effects, which have an impact on charged particles that are far away, even if the impact is weak. The added Coulomb effect also simplifies the original Boltzmann collision operator, as higher order effects are no longer accounted for.

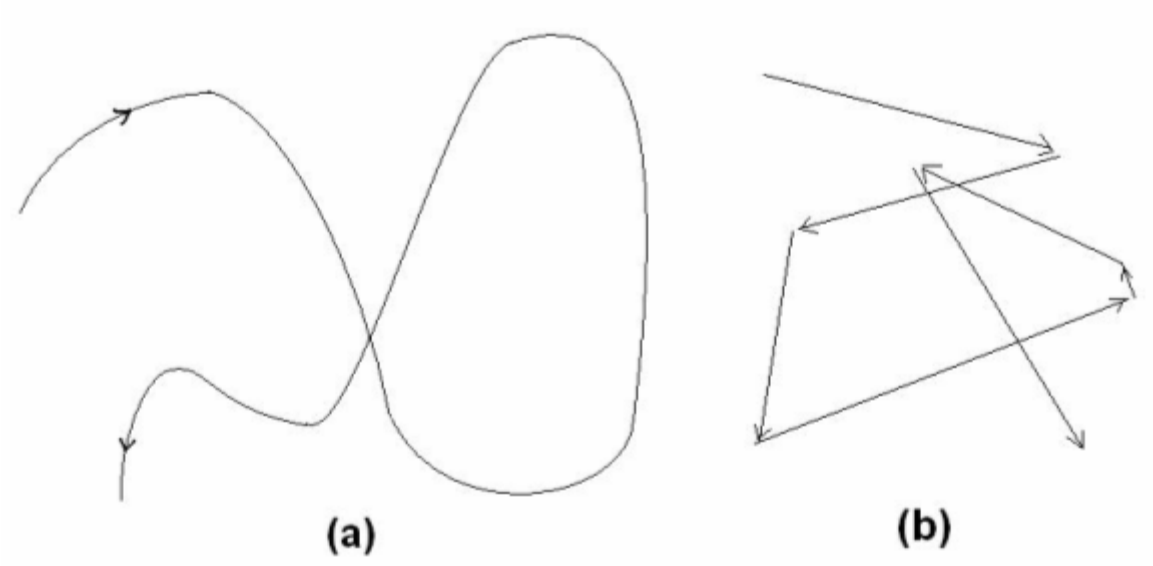

Figure 21. Comparison of Charged and Fluid Particle Collision Trajectories [41]

b. Molecular Assumptions

The applicability of the Fokker-Planck collision operator is limited to systems falling under the following assumptions [41].

- A dilute or extremely low dense gas of point-like molecules, causing binary collisions that result in small velocity deflections.
- The distribution function is smooth and can be treated as if it were in physical space.
- The distance between collisions of particles is large enough that the fluctuations in the electric field due to Coulomb interactions will be negligibly small. This distance must also be large in comparison to the distance between molecules such that collisions between multiple particles at an instant are eliminated. This distance is described by the sphere of influence, in which $d = 2\lambda_D$.

The sphere of influence has already been introduced in figure 13. For the case of fluid particles, the distance between the center of masses was used. This distance corresponds to the hard sphere model of binary collisions. In the case of charged particles, with long range interactions, this distance does not characterize the cross sectional area of which collision takes place. For plasmas, the hard sphere model does not work because it allows for large deflections in the velocity vector. Therefore the Fokker-Planck model that describes collisions through a diffusion process is utilized. Because higher order effects are neglected in the Fokker-Planck model, the impact parameter, b, is used in modeling the collision cross section between charged particles. The impact parameter, b, is the distance of closest approach between the centers of two molecules if there was no collision. Figure 22 illustrates the impact parameter versus the distance between center of masses.

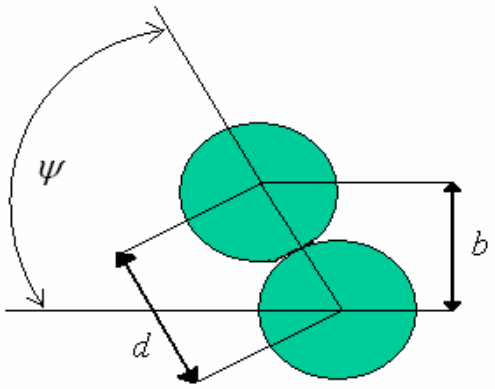

Figure 22. Sphere of Influence for Plasmas [37]

In modeling of the collision processes, it is important to note the Boltzmann gas limit, which describes the mathematical terms in the physical space for which the Boltzmann equation has been sufficiently proven. As with Boltzmann's equation, the following is assumed [37].

- $N \to \infty$ The number of molecules is taken to be very large.

- $m \to 0$ The weight of each particle is taken to be extremely small compared to the total weight of the system. This allows us to describe the mass as the total system as being constant $Nm \to \text{constant}$.
- $d \to 0$ The size of the sphere of influence, which describes the range of intermolecular forces is taken to be extremely small such that $Nd^2 \to \text{constant}$. Therefore the mean free path which is proportional to $\frac{1}{Nd^2}$ is constant as well.

Because the mean free path is finite, this limit describes the fluid as a calorically imperfect gas. This is because of the fact that the fluid is described as having intermolecular collisions leading to interparticle forces that can change the distribution function. Using a strict thermodynamic sense, the fluid will, however, be described as a calorically perfect gas. The reason why is because from the Boltzmann gas limit, it can also be derived that the total action volume goes to zero. $N\sigma^3 \to 0$ What this means physically is that, for this case, the system is irreversible because the volume of the system is not increasing, which is a key point in the second law of thermodynamics. A calorically perfect gas is considered to be reversible, while really in nature that isn't true, for the assumptions given in the Boltzmann gas limit, we can model this fluid as a perfect gas.

c. Coulomb Collision Dynamics

Modeling collisions between charged particles requires an understanding of how the Coulomb force affects each particle's trajectory.

Figure 23, taken from [41], shows the collision between an electron and an ion, using the impact parameter to derive a cross sectional area from where Coulomb collisions occur. Considering an electron of charge, q_e, traveling by an ion of charge, q_i, with a large impact parameter, b, the angle of deflection of the electron velocity is small.

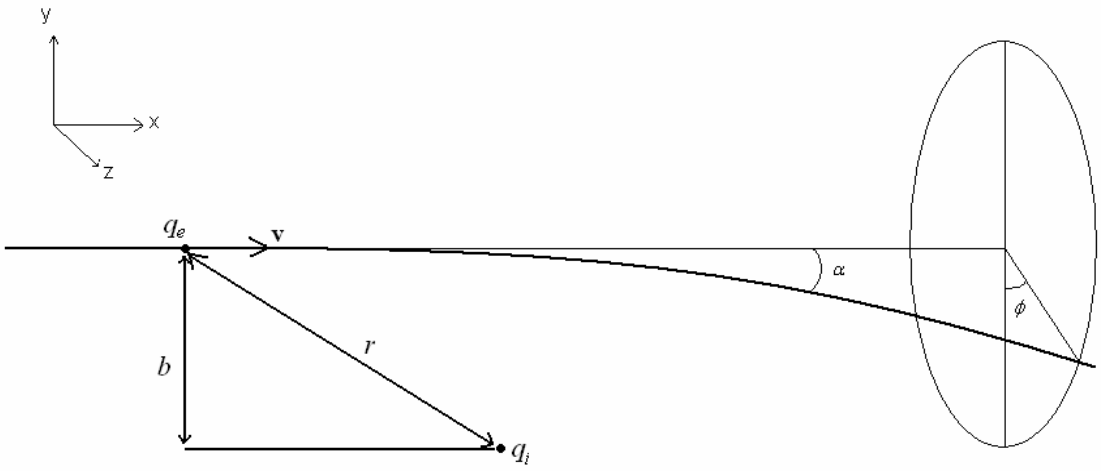

Figure 23. Illustration of Charged Particle Collision Interaction [41]

The Coulomb force exerted on the electron by the ion is used with the impact parameter to determine the angle of deflection of the electron's trajectory [41].

$$m_e \Delta v_y = \int_{-\infty}^{\infty} \frac{q_e q_i}{4\pi\varepsilon_0 r^2(t)} \frac{b}{r(t)} dt = \frac{q_e q_i}{2\pi\varepsilon_0 b v} \qquad \alpha = \frac{\Delta v_y}{v} = \frac{q_e q_i}{2\pi\varepsilon_0 b m_e v^2}$$

For simplicity of formulation, the variables are redefined in terms of center of mass and relative position.

$$m_* = \frac{m_a m_b}{m_a + m_b} \qquad r = x_a - x_b \qquad \dot{r} = u \qquad \alpha_* = \frac{q_a q_b}{2\pi\varepsilon_0 b m_* u^2}$$

From the term α_*, the importance of the size of the impact parameter is seen. For large values of *b*, the deflection angle is small, which corresponds to the deflection trends for charged particles. Using a Cartesian coordinate system (*x*, *y*, *z*) in which the particle of interest is moving in the *x* direction, the velocity deflections are related to the deflection angle as follows [41].

$$\Delta u_x = u\left(\cos\alpha_* - 1\right) \qquad \Delta u_y = u\sin\alpha_*\cos\phi \qquad \Delta u_z = u\sin\alpha_*\sin\phi \qquad \Delta \mathbf{v}_a = \frac{m_b}{m_a + m_b}\Delta \mathbf{u}$$

$$\Delta v_x = \left(1+\frac{m_a}{m_b}\right)\left(\frac{q_a q_b}{2\pi\varepsilon_0 m_a}\right)^2 \frac{1}{2bu^3} \tag{4.14}$$

$$\Delta v_y = \frac{q_a q_b}{2\pi\varepsilon_0 m_a}\frac{\cos\phi}{ub} \tag{4.15}$$

$$\Delta v_z = \frac{q_a q_b}{2\pi\varepsilon_0 m_a}\frac{\sin\phi}{ub} \tag{4.16}$$

These are the deflections in the velocity of a charged particle due to Coulomb collisions. Relativistic effects are not accounted for which is adequate for most laboratory and space plasmas.

d. Statistical Description of Collision Operator

The Fokker-Planck collision operator is characterized by a probability distribution function (PDF) [41].

$$f\left(v, t+\Delta t\right) = \int f\left(v-\Delta v, t\right) F\left(v-\Delta v, \Delta v\right) d\Delta v \qquad \int F\left(v, \Delta v\right) d\Delta v = 1 \tag{4.17}$$

$F\left(v-\Delta v, \Delta v\right)$ is the probability that the velocity of a particle will change from v to $v+\Delta v$. The sum of the probabilities of the velocity change is unity. The integrand is expanded out to the following using Taylor series expansion about Δv:

$$f\left(v, t+\Delta t\right) = \int\left[f\left(v,t\right)F\left(v,\Delta v\right) - \Delta v\frac{\partial f\left(v,t\right)F\left(v,\Delta v\right)}{\partial v} + \frac{\left(\Delta v\right)^2}{2}\frac{\partial^2 f\left(v,t\right)F\left(v,\Delta v\right)}{\partial v^2}\right] d\Delta v \tag{4.18}$$

Two expectation values are defined from this expansion as the following:

$$\langle \Delta v \rangle = \int F(v, \Delta v) \Delta v d\Delta v \tag{4.19}$$

$$\left\langle (\Delta v)^2 \right\rangle = \int F(v, \Delta v) (\Delta v)^2 d\Delta v \,. \tag{4.20}$$

Using the expectation values, the rate of change of the distribution function due to collisions is simplified.

$$C(f) = \left. \frac{\partial f(v,t)}{\partial t} \right|_{collisions} = -\frac{\partial}{\partial v}\left(\frac{\langle \Delta v \rangle}{\Delta t} f \right) + \frac{\partial^2}{\partial v^2}\left(\frac{\left\langle (\Delta v)^2 \right\rangle}{2\Delta t} f \right) \tag{4.21}$$

$$C(f) = -\nabla_v \cdot \mathbf{A} = \frac{\langle \Delta v \rangle}{\Delta t} f - \frac{\partial}{\partial v}\left(\frac{\left\langle (\Delta v)^2 \right\rangle}{2\Delta t} f \right) \tag{4.22}$$

$\mathbf{A}_a = \sum_b \mathbf{A}_{ab}$ (multiple species)

Higher order terms in the Taylor series expansion are neglected because they correspond to large deflections of the velocity vector, which is negligible in plasmas. This assumption is a very important aspect of the Fokker-Planck collision operator and how it applies effectively in modeling plasma collisions [28]. Mathematically, this assumption is justified later because those higher order terms decrease by a factor of $\ln \Lambda$. The term $\ln \Lambda$ accounts for the number of particles in the Debye sphere. The first collision term represents the drag force on the plasma particles, while the second term is characterized as a diffusion term. At equilibrium, the distribution takes a Maxwellian form.

e. Collision Operator Formulation

With the nature of the Coulomb collisions described along with the statistical description, the Fokker-Planck collision operator can be determined. For this formulation, a cross section, as a function of the impact parameter and angle, is utilized [41]. For now on, the impact parameter will be identified as *r*. Figure 24, illustrates the cross section.

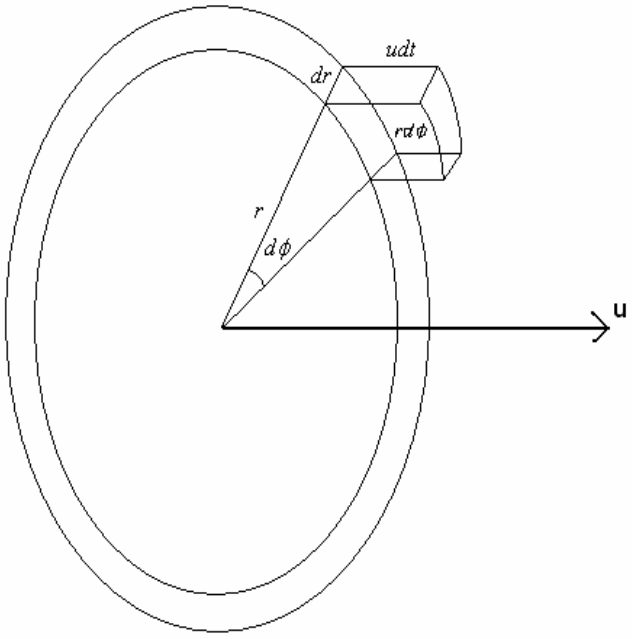

Figure 24. Collision Cross Section [41]

The area of the collision cross section is defined as $d\sigma = rdrd\phi$, and the volume is $dV = rdrd\phi udt$. The distance that particle *a* travels relative to particle *b* in time *dt* is udt. The number of collisions between particle *a* and *b* in a given time *dt* can be calculated from the probability distribution function as follows [41].

$$\Delta t d\phi r dr \int f_b\left(\mathbf{v}^b\right) u d^3 v^b \tag{4.23}$$

$$\mathbf{u} = \mathbf{v}^a - \mathbf{v}^b$$

By multiplying the velocity deflections, from eqns. (4.14), (4.15), and (4.16), with the number of collisions (4.23), the expectation values are defined more explicitly.

$$\frac{\left\langle \Delta v_k \right\rangle^{ab}}{\Delta t} = -\frac{L^{ab}}{4\pi}\left(1+\frac{m_a}{m_b}\right)\int \frac{u_k}{u^3} f_b\left(\mathbf{v}_b\right) d^3 v_b \tag{4.24}$$

$$\frac{\left\langle \Delta v_k \Delta v_l \right\rangle^{ab}}{\Delta t} = \frac{L^{ab}}{4\pi}\int U_{kl} f_b\left(\mathbf{v}^b\right) d^3 v^b \tag{4.25}$$

$$U_{kl} = \frac{u^2\delta_{kl} - u_k u_l}{u^3} \qquad\qquad L^{ab} = \left(\frac{q_a q_b}{m_a \varepsilon_0}\right)^2 \ln\Lambda$$

Using Rosenbluth potentials, from eqns. (4.24) and (4.25), the Fokker-Planck collision operator is defined as follows.

$$\varphi_b\left(\mathbf{v}^a\right) = -\frac{1}{4\pi}\int \frac{1}{u} f_b\left(\mathbf{v}^b\right) d^3 v^b \tag{4.26}$$

$$\psi_b\left(\mathbf{v}^a\right) = -\frac{1}{8\pi}\int u f_b\left(\mathbf{v}^b\right) d^3 v^b \tag{4.27}$$

$$C_{ab}\left(f_a, f_b\right) = \ln\Lambda\left(\frac{q_a q_b}{m_a \varepsilon_0}\right)^2 \frac{\partial}{\partial v_k^a}\left(\frac{m_a}{m_b}\frac{\partial \varphi_b}{\partial v_k^a} f_a - \frac{\partial^2 \varphi_b}{\partial v_k^a v_l^a}\frac{\partial f_a}{\partial v_l^a}\right) \tag{4.28}$$

It is important to take note of the $\ln\Lambda$ term. This term is known as the Coulomb logarithm [41]. In the previous subsection, d, this term was given credit for mathematically justifying the neglect of the higher order terms in the collision equation. Physically, Λ is the average number of charged particles in the Debye sphere. The value of Λ is approximated for most plasmas as

$$\Lambda \equiv \frac{\lambda_D}{r_{\min}} \gg 1.$$

This trend is required for the velocity deflections to be considered small. This trend means that the Debye length is much smaller than the impact parameter. In this case, the charged particles do not typically approach close enough to directly collide, as the long-range coulomb force prevents this. More details of this term and the Fokker-Planck derivation can be found in [41].

The final form of the Fokker-Planck collision operator is found by substituting the integral descriptions of the Rosenbluth potentials.

$$C_{ab}\left(f_a, f_b\right) = \frac{q_a^2 q_b^2 \ln\Lambda}{8\pi\varepsilon_0^2 m_a} \frac{\partial}{\partial v_k^a} \int U_{kl} \left[\frac{f_b\left(\mathbf{v}^b\right)}{m_a} \frac{\partial f_a\left(\mathbf{v}^a\right)}{\partial v_l^a} - \frac{f_a\left(\mathbf{v}^a\right)}{m_b} \frac{\partial f_b\left(\mathbf{v}^b\right)}{\partial v_l^b} \right] d^3 v^b \tag{4.29}$$

This collision operator satisfies the H-Theorem along with conserving mass, momentum, and energy.

$$\int C_{ab}\left(f_a\right) d^3 v = 0 \tag{4.30}$$

$$\int m_a \mathbf{v}_a C_{ab}\left(f_a\right) d^3 v_a = -\int m_b \mathbf{v}_b C_{ba}\left(f_b\right) d^3 v_b \tag{4.31}$$

$$\int \frac{m_a v_a^2}{2} C_{ab}\left(f_a\right) d^3 v_a = -\int \frac{m_b v_b^2}{2} C_{ba}\left(f_b\right) d^3 v_b \tag{4.32}$$

At equilibrium, the distribution of the PDF's, for this collision operator, are Maxwellian.

$$f_a^{eq}\left(\mathbf{r},t\right) = n_a\left(\mathbf{r},t\right) \left(\frac{m_a}{2\pi T_a\left(\mathbf{r},t\right)} \right)^{3/2} e^{\left(\frac{m_a \left[\mathbf{v}-\mathbf{V}_a\left(\mathbf{r},t\right)\right]^2}{2T_a\left(\mathbf{r},t\right)} \right)} \tag{4.33}$$

These attributes correspond with the characteristics of the Boltzmann collision operator, making the Fokker-Planck collision operator useful in understanding Coulomb collision interactions.

3. Kinetic Plasma Equations

With the description and understanding of plasma collisions properly defined, the modeling equation can now be obtained. The Fokker Planck collision operator provides a very effective physical understanding of the kinetic plasma collision process. This collision operator is, however, difficult to model itself. Therefore an estimation that satisfies the H-Theorem, molecular assumptions, particle interaction, and long-range coulomb interaction must be used. In order to accomplish this, the Boltzmann equation with the BGK collision operator is used. In the case of normal fluid particles, as discussed in the previous chapter, this model was also used. This model will have a different development, however, due to the known electromagnetic interactions between particles.

$$\frac{\partial f_\alpha}{\partial t} + \mathbf{v}\cdot\frac{\partial f_\alpha}{\partial \mathbf{r}} + \frac{q_\alpha}{m_\alpha}\left(\mathbf{E}+\mathbf{v}\times\mathbf{B}\right)\cdot\frac{\partial f_\alpha}{\partial \mathbf{v}} = \left(\frac{\partial f_\alpha}{\partial t}\right)_{coll} \tag{4.1}$$

The definitions of particle density (4.2), average velocity (4.3), charge density (4.5), and current density (4.6) are incorporated in the kinetic plasma equations. Multiplying by 1, $m_\alpha \mathbf{v}$, and $m_\alpha \mathbf{v}^2/2$ respectively, and integrating over velocity space yields the zeroth, first, and second moments of the Boltzmann equation [6].

$$\frac{\partial n_\alpha}{\partial t} + \nabla\cdot\left(n_\alpha \mathbf{u}_\alpha\right) = 0 \tag{4.34}$$

$$\frac{\partial}{\partial t}\left(n_\alpha m_\alpha \mathbf{u}_\alpha\right) + \nabla\cdot\left(n_\alpha m_\alpha \left\langle \mathbf{vv}\right\rangle_\alpha\right) + q_\alpha n_\alpha\left(\mathbf{E}+\mathbf{u}_\alpha\times\mathbf{B}\right) = \int C_{\alpha\beta} m_\alpha \mathbf{v} d^3v \tag{4.35}$$

$$\frac{\partial}{\partial t}\left(n_\alpha \frac{1}{2} m_\alpha \left\langle v^2\right\rangle_\alpha\right) + \nabla\cdot\left(n_\alpha \frac{1}{2} m_\alpha \left\langle v^2 \mathbf{v}\right\rangle_\alpha\right) - q_\alpha n_\alpha \mathbf{E}\cdot\mathbf{u}_\alpha = \int C_{\alpha\beta}\frac{1}{2} m_\alpha v^2 d^3v \tag{4.36}$$

Where the particle velocity $\mathbf{v}$ is decomposed into an average part $\mathbf{u}_\alpha$ and random part $\mathbf{v}_\alpha$ as $\tilde{\mathbf{v}}_\alpha = \mathbf{v} - \mathbf{u}_\alpha$.

In order to complete these equations, collision terms that encompass electromagnetic effects and particle collisions must be properly defined. Using the decomposition of the particle velocity, the definition of pressure and temperature, and the substitution for the collision terms, the momentum and energy equations are further described as follows [6].

$$\frac{\partial}{\partial t}\left(n_\alpha m_\alpha \mathbf{u}_\alpha\right) + \nabla\cdot\left(n_\alpha m_\alpha \mathbf{u}_\alpha \mathbf{u}_\alpha\right) + \nabla\cdot p_\alpha + q_\alpha n_\alpha\left(\mathbf{E} + \mathbf{u}_\alpha \times \mathbf{B}\right) = -\nabla\cdot\boldsymbol{\pi}_\alpha + \mathbf{R}_\alpha \tag{4.37}$$

$$\begin{aligned}&\frac{\partial}{\partial t}\left(\frac{1}{2}n_\alpha m_\alpha u_\alpha^2\right) + \frac{\partial}{\partial t}\left(\frac{3}{2}n_\alpha k T_\alpha\right) + \nabla\cdot\left(\frac{1}{2}n_\alpha m_\alpha u_\alpha^2 \mathbf{u}_\alpha + \frac{3}{2}n_\alpha k T_\alpha \mathbf{u}_\alpha\right)\\ &+\mathbf{u}_\alpha\nabla\left(kT_\alpha\right) + p_\alpha\nabla\cdot\mathbf{u}_\alpha = n_\alpha q_\alpha \mathbf{E}\cdot\mathbf{u}_\alpha - \boldsymbol{\pi}_\alpha : \nabla\mathbf{u}_\alpha - \nabla\cdot\mathbf{h}_\alpha + \mathbf{u}_\alpha\cdot\mathbf{R}_\alpha + Q_\alpha\end{aligned} \tag{4.38}$$

All of the terms in these equations are defined as follows.

$$\left\langle \mathbf{vv}\right\rangle_\alpha = \mathbf{u}_\alpha\mathbf{u}_\alpha + \left\langle \tilde{\mathbf{v}}_\alpha\,\tilde{\mathbf{v}}_\alpha\right\rangle \tag{4.39}$$

$$\mathbf{P}_\alpha = n_\alpha m_\alpha\left\langle \tilde{\mathbf{v}}_\alpha\,\tilde{\mathbf{v}}_\alpha\right\rangle = p_\alpha\mathbf{I} + \boldsymbol{\pi}_\alpha \tag{4.40}$$

$$p_\alpha = \frac{1}{3}Tr\left(\mathbf{P}_\alpha\right) = \frac{1}{3}n_\alpha m_\alpha\left\langle \tilde{v}_\alpha^2\right\rangle = n_\alpha k T_\alpha, \quad T_\alpha = \frac{m_\alpha}{3k}\left\langle \tilde{v}_\alpha^2\right\rangle \tag{4.41}$$

$$\boldsymbol{\pi}_\alpha = n_\alpha m_\alpha\left\langle \tilde{\mathbf{v}}_\alpha\,\tilde{\mathbf{v}}_\alpha - \frac{1}{3}\tilde{v}_\alpha^2\mathbf{I}\right\rangle \tag{4.42}$$

$$\int C_{\alpha\beta} m_\alpha \mathbf{v} d^3v = \int C_{\alpha\beta} m_\alpha\,\tilde{\mathbf{v}}_\alpha\, d^3v = \mathbf{R}_\alpha \tag{4.43}$$

$$\mathbf{h}_\alpha = \frac{1}{2}n_\alpha m_\alpha\left\langle \tilde{v}_\alpha^2\,\tilde{\mathbf{v}}_\alpha\right\rangle \tag{4.44}$$

$$\int C_{\alpha\beta}\frac{1}{2}m_\alpha \mathbf{v}d^3v = \int C_{\alpha\beta}\left(m_\alpha \mathbf{u}_\alpha \cdot \tilde{\mathbf{v}}_\alpha + \frac{1}{2}m_\alpha \tilde{v}_\alpha^2\right)d^3v = \mathbf{u}_\alpha \cdot \mathbf{R}_\alpha + Q_\alpha \tag{4.45}$$

$$Q_\alpha = \int C_{\alpha\beta}\frac{1}{2}m_\alpha \tilde{v}_\alpha^2\, d^3v \tag{4.46}$$

p_α is the pressure; π_α is the stress tensor; $\mathbf{h}_\alpha$ is the heat flow by random motion; $\mathbf{R}_\alpha$ is the friction force between different particle species, and Q_α is the heat transferred to a system of particles from collisions with particles of a different species. The momentum equation is simplified by the continuity equation, and the energy equation is further simplified by the continuity and momentum equations. The final forms of the Boltzmann equation for a particle species is the following.

$$\frac{\partial n_\alpha}{\partial t} + \nabla\cdot\left(n_\alpha \mathbf{u}_\alpha\right) = 0 \tag{4.34}$$

$$\frac{\partial}{\partial t}\left(n_\alpha m_\alpha \mathbf{u}_\alpha\right) + \mathbf{u}_\alpha \nabla\cdot\left(n_\alpha m_\alpha \mathbf{u}_\alpha\right) = -\nabla\cdot p_\alpha - q_\alpha n_\alpha\left(\mathbf{E} + \mathbf{u}_\alpha \times \mathbf{B}\right) - \nabla\cdot\pi_\alpha + \mathbf{R}_\alpha \tag{4.47}$$

$$\frac{3}{2}\frac{\partial}{\partial t}\left(n_\alpha kT_\alpha\right) + \frac{3}{2}\mathbf{u}_\alpha\cdot\nabla\left(n_\alpha kT_\alpha\right) + n_\alpha kT_\alpha \nabla\cdot\mathbf{u}_\alpha = -\pi_\alpha : \nabla\mathbf{u}_\alpha - \nabla\cdot\mathbf{h}_\alpha + Q_\alpha \tag{4.48}$$

For plasmas consisting of electrons and one kind of ion, the two fluid equations are derived from the previous equations [6].

$$\frac{\partial n_e}{\partial t} + \nabla\cdot\left(n_e \mathbf{u}_e\right) = 0 \tag{4.49}$$

$$\frac{\partial n_i}{\partial t} + \nabla\cdot\left(n_i \mathbf{u}_i\right) = 0 \tag{4.50}$$

$$\frac{\partial}{\partial t}\left(n_e m_e \mathbf{u}_e\right) + \mathbf{u}_e \nabla\cdot\left(n_e m_e \mathbf{u}_e\right) = -\nabla\cdot p_e - q_e n_e\left(\mathbf{E} + \mathbf{u}_e \times \mathbf{B}\right) - \nabla\cdot\pi_e + \mathbf{R}_e \tag{4.51}$$

$$\frac{\partial}{\partial t}\left(n_i m_i \mathbf{u}_i\right) + \mathbf{u}_i \nabla\cdot\left(n_i m_i \mathbf{u}_i\right) = -\nabla\cdot p_i - q_i n_i\left(\mathbf{E} + \mathbf{u}_i \times \mathbf{B}\right) - \nabla\cdot\pi_i + \mathbf{R}_i \tag{4.52}$$

$$\frac{3}{2}\frac{\partial}{\partial t}\left(n_e kT_e\right)+\frac{3}{2}\mathbf{u}_e\cdot\nabla\left(n_e kT_e\right)+n_e kT_e\nabla\cdot\mathbf{u}_e=-\pi_e:\nabla\mathbf{u}_e-\nabla\cdot\mathbf{h}_e-\left(\mathbf{u}_e+\mathbf{u}_i\right)\cdot\mathbf{R}_e-Q_i \quad (4.53)$$

$$\frac{3}{2}\frac{\partial}{\partial t}\left(n_i kT_i\right)+\frac{3}{2}\mathbf{u}_i\cdot\nabla\left(n_i kT_i\right)+n_i kT_i\nabla\cdot\mathbf{u}_i=-\pi_i:\nabla\mathbf{u}_i-\nabla\cdot\mathbf{h}_i+Q_i \quad (4.54)$$

The collision terms are redefined as $R_i=-R_e$ and $Q_e=-\left(\mathbf{u}_e+\mathbf{u}_i\right)\cdot\mathbf{R}_e-Q_i$, which are derived out of momentum and energy conservation. The collision term, $\mathbf{R}_e$ is simplified by defining it as the sum of the average impeding force on electrons due to collisions with ions and the thermoelectric force [42]. The thermoelectric force is created by temperature gradients in the electrons during collision that generate an addition electric current in the opposite direction of the gradient. This temperature gradient also causes additional kinetic energy to be transported by the electrons, as will be seen in the heat flux.

$$\mathbf{R}_e=q_e n_e\left(\boldsymbol{\eta}\cdot\mathbf{j}-\boldsymbol{\delta}\cdot\nabla T_e\right) \quad (4.55)$$

The heat flux term for electrons and ions are defined by the temperature gradients and kinetic energy terms associated with the induced electric current caused by the gradients [42].

$$\mathbf{h}_e=-\boldsymbol{\kappa}_e\cdot\nabla T_e-T_e\boldsymbol{\delta}\cdot\mathbf{j} \quad (4.56)$$

$$\mathbf{h}_i=-\boldsymbol{\kappa}_i\cdot\nabla T_i \quad (4.57)$$

The heat flux for the ions doesn't include the kinetic energy transport term because the ions are considered to be negligibly stationary in comparison to the electrons. The heat transferred to the ions from collisions with electrons is described by the temperature difference between electrons and ions [6]. Later on, in forming the macroscopic relationships, these terms will be further described in terms of constitutive equations.

$$Q_i = \frac{3n_e k\left(T_e - T_i\right)}{2\tau_{eq}} \tag{4.58}$$

Where τ_{eq} is the temperature equilibrium time scale, describing the time scale in which equal temperature between electrons and ions is established. These two-fluid equations along with Maxwell's equations, are used to fully describe the collective mesoscopic behavior of plasma particles.

C. Magnetohydrodynamics

1. Formulation of MHD Equations

From the two-fluid equations, incorporating assumptions associated with the macroscopic length scale, the magnetohydrodynamic equations can be derived, providing a macroscopic description of plasmas.

The most important characteristic of MHD is that it assumes charge neutrality. In terms of the Debye length and plasma frequency, these assumptions are described as follows.

$$\frac{\lambda_D}{\lambda_H} \ll 1 \qquad \frac{\omega_{pe}^{-1}}{\tau_H} \ll 1 \qquad \frac{R_e}{\lambda_H} \ll \frac{R_i}{\lambda_H} \ll 1$$

This assumption is derived from the fact that the macroscopic length scales are large enough for Coulomb fluctuations to negligible, and the charges emitted by electrons and ions are sufficiently close enough to assume negligible net charge. The macroscopic length scale is also sufficiently larger than the Larmor radius, $\left(R_e, R_i\right)$, such that the particles are no longer described as in the single particle model. The total mass density, momentum density, pressure, total charge density, and current density are re-described using eqns. (4.2), (4.3), (4.4), (4.5), and (4.6) to sum the species of electrons and ions. This summation over the two species forms the one-fluid macroscopic equation.

$$n_e m_e + n_i m_i = \rho \qquad \rho_0 = q_e n_e + q_i n_i \qquad \mathbf{j} = n_e q_e \mathbf{u}_e + n_e q_e \mathbf{u}_e$$

$$\rho \mathbf{v} = n_e m_e \mathbf{u}_e + n_i m_i \mathbf{u}_i \qquad p = p_e + p_i$$

At the macroscopic scale, the temperature relaxation time is considered to be large enough that thermal equilibration has already taken place. From this assumption, the macroscopic value of temperature is defined, and the collision term Q_i, relating the temperature difference between electrons and ions, is considered to be very small.

$$T = T_e = T_i \qquad \tau_H \gg \tau_{eq}$$

$$Q_i = 0 \tag{4.59}$$

The resistive collision term in the two-fluid equations are also be simplified. As shown in (4.55), $\mathbf{R}_e$ includes a resistive and thermoelectric part. In the resistive part, $q_e n_e \boldsymbol{\eta} \cdot \mathbf{j}$, $\bar{\boldsymbol{\eta}}$ is modeled as a tensor including isotropic and anisotropic parts [42]. Due to the time scales involved at the macroscopic level, this term is simplified to its isotropic term $\bar{\boldsymbol{\eta}} = \eta \bar{\mathbf{I}}$. This is the most used resistive model for the resistivity term in plasma dynamics. The thermoelectric part of the resistive collision term is neglected because, as shown by [42], the electron cyclotron frequency multiplied by the electron relaxation time is sufficiently small under the MHD approximation.

$$\left|\Omega_e \tau_e\right| \ll 1$$

This assumption means that the cyclotron electron gyro-motion is insignificant in relation to the total motion of the each particle. This assumption simplifies the resistive effects due to coulomb interactions to obtain

$$\mathbf{R}_e = n_e q_e \eta \mathbf{j}. \tag{4.60}$$

The macroscopic equations for mass density, charge density, momentum, and internal energy are now derived from the two-fluid kinetic equations as follows.

$$\frac{\partial \rho}{\partial t} + \nabla \cdot (\rho \mathbf{v}) = 0 \tag{2.12}$$

$$\frac{\partial \rho_0}{\partial t} + \nabla \cdot \rho_0 \mathbf{v} = 0 \tag{3.1}$$

$$\frac{\partial \rho \mathbf{v}}{\partial t} + \mathbf{v} \nabla \cdot \rho \mathbf{v} = -\nabla p + \tau \mathbf{E} + \mathbf{j} \times \mathbf{B} - \nabla \cdot \bar{\boldsymbol{\pi}} \tag{4.61}$$

$$\frac{3}{2} \frac{\partial}{\partial t} (\rho k T) + \frac{3}{2} \mathbf{v} \cdot \nabla (\rho k T) + \rho k T \nabla \cdot \mathbf{v} = -\bar{\boldsymbol{\pi}} : \nabla \mathbf{v} - \nabla \cdot \mathbf{h} - \eta \mathbf{j}^2 \tag{4.62}$$

The electric field term in the momentum equation can be neglected due to the MHD approximation of quasi-charge neutrality.

$$|n_e - n_i| \ll n_e \qquad \tau = q_e n_e + q_i n_i \rightarrow -e n_e + Z e n_i = -e (n_e - Z n_i) \approx 0$$

The momentum and energy equations require further simplification and description of the constitutive equations for $(\mathbf{h}_e, \mathbf{h}_i)$ and $\left(\bar{\boldsymbol{\pi}}_e, \bar{\boldsymbol{\pi}}_i\right)$.

At the macroscopic level, the statistical particle distributions are not used to describe the heat flux and stress tensor. Therefore, constitutive equations, relating the physical quantities to the material of the fluid are used to model the effects on the macroscopic scale. The stress and heat flux terms take the following form.

$$\bar{\boldsymbol{\pi}} = \mu \nabla \mathbf{v} \tag{2.15}$$

$$\mathbf{h} = -\kappa\nabla\left(kT\right) \tag{2.16}$$

By combining the continuity (2.12), simplified version of momentum (4.61), the magnetic induction equation (3.23), and Maxwell's 3rd equation (3.10), the magnetohydrodynamic (MHD) equations are formulated [6].

$$\frac{\partial\rho}{\partial t}+\nabla\cdot(\rho\mathbf{v})=0 \tag{2.12}$$

$$\frac{\partial\rho\mathbf{v}}{\partial t}+\mathbf{v}\cdot\nabla\rho\mathbf{v}=-\nabla p-\nabla\left(\frac{B^2}{2\mu_0}\right)+\frac{1}{\mu_0}\left(\mathbf{B}\cdot\nabla\right)\mathbf{B}+\mu\nabla^2\mathbf{v} \tag{4.63}$$

$$\frac{\partial\mathbf{B}}{\partial t}+\mathbf{v}\cdot\nabla\mathbf{B}=\mathbf{B}\cdot\nabla\mathbf{v}+\frac{\eta}{\mu_0}\nabla^2\mathbf{B} \tag{3.23}$$

$$\nabla\cdot\mathbf{B}=0 \tag{3.10}$$

These equations couple together to govern the characteristics of magnetized fluid flow and induced magnetic field.

The equation for internal energy has the following final form.

$$\frac{3}{2}\frac{\partial}{\partial t}\left(\rho kT\right)+\frac{3}{2}\mathbf{v}\cdot\nabla\left(\rho kT\right)+\rho kT\nabla\cdot\mathbf{v}=-\mu\nabla\mathbf{v}:\nabla\mathbf{v}-\nabla\cdot-\kappa\nabla\left(kT\right)-\eta\mathbf{j}^2 \tag{4.64}$$

2. MHD Characteristic Parameters

In normal hydrodynamic flows, the Reynolds number (Re) and Mach number (M) are typically the most non-dimensional characteristics. These parameters are used to understand the flow characteristics from a more universal perspective. In Magnetohydrodynamics, there are more non-dimensionalized terms that describe different MHD characteristics [5].

- Ratio of kinetic to magnetic energy: $\beta = \frac{2\mu_0 \rho v^2}{B_0^2} \Rightarrow \frac{\text{Kinetic Energy}}{\text{Magnetic Energy}}$

  β is an indicator of the relative dominance between the hydrodynamic and magnetic field. For cases of $\beta \gg 1$, the hydrodynamic flow field dominates over the magnetic field. The magnetic field still influences the system, but the kinetic energy dictates the evolution of fluid particle trends. When $\beta \ll 1$, the magnetic field dominates fluid particle motions.

- Magnetic Reynolds number:

  $$R_m = \frac{\mu_0 v L}{\eta} = \frac{vL}{\sigma} \Rightarrow \frac{convection}{diffusion} = \frac{\mu_0 \left[(\mathbf{v} \cdot \nabla)\mathbf{B} - (\mathbf{B} \cdot \nabla)\mathbf{v} \right]}{\eta \nabla^2 \mathbf{B}}$$

  The magnetic Reynolds number is the ratio of the magnetic convection to magnetic diffusion. This governs the evolution of the induced magnetic field in fluid particles. For high R_m, the fluid is highly conductive leading to a large induced magnetic field coupled to the velocity field. For low R_m, the fluid is highly resistive and very little induced magnetic field evolves, causing decoupling between the magnetic field and velocity field.

- Interaction parameter: $N = \frac{\sigma B^2 l}{\rho u} \Rightarrow \frac{\text{Lorentz force}}{\text{inertial force}}$

  The interaction parameter is important in the relating the dominance of the magnetic field over the evolution of flow field structures. This parameter is important in characterizing vorticity dynamics and magnetic field influence in turbulence processes. More detail on how this parameter describes vorticity development is provided later.

- $H = \dfrac{B_0 L}{\sqrt{\rho_0 \eta \nu}} \Rightarrow \dfrac{\text{Lorentz Force}}{\text{Viscous Force}}$

  Hartmann number is important in the study of boundary layers under magnetic field influence. For $H \gg 1$, the boundary layer thickness will shorten due to the redirection of momentum caused by the Lorentz force. For $H \ll 1$, the boundary layer thickness will be longer than the previous case as the Lorentz force is negligible.

D. Conclusion

The MHD equations provide an effective means of describing the interaction between plasma or a conducting fluid with a magnetic field. These equations are the basis for which plasma jet flow is described later in this paper. At the kinetic level, plasma flow is described by the moments of the Boltzmann equation along with Maxwell's equation. As previously shown, the important concepts behind the formulation of the MHD equations are that the plasma flow travels at non-relativistic velocities, quasi-charge neutrality, and the macroscopic length scale. These assumptions, describing plasma flow at the macroscopic level, transform the kinetic plasma equations into the MHD model.

CHAPTER V

LATTICE BOLTZMANN METHOD FOR MAGNETOHYDRODYNAMICS

A. Introduction

The concepts behind the Boltzmann equation and kinetic theory have been described showing how the Boltzmann equation can be used to recover both Navier-Stokes and MHD equations while satisfying the H-theorem. Therefore, MHD can be modeled by a discretized form of the Boltzmann equation (LBE) using the BGK collision operator under certain constraints. This model is known as the lattice Boltzmann method (LBM). [8-10] describes and validates how the Navier-Stokes and MHD equations can be modeled using LBM. This chapter demonstrates the formulation of the LBM model for MHD, along with a verification of the method.

B. Lattice Boltzmann Method

The Boltzmann equation, that models kinetic theory, is

$$\frac{\partial f_\alpha}{\partial t} + \mathbf{c} \cdot \frac{\partial f_\alpha}{\partial \mathbf{x}} = \left(\frac{\partial f_\alpha}{\partial t} \right)_{coll} . \tag{5.1}$$

This form of the Boltzmann equation differs from the form of (2.7) and (4.1) as it is expressed in vector notation, with the characteristic velocity, **c**. This notation is used for the formulation of the lattice Boltzmann method.

Using the linear BGK collision operator, this equation can be rewritten as

$$\frac{\partial f_\alpha}{\partial t} + \mathbf{c} \cdot \frac{\partial f_\alpha}{\partial \mathbf{x}} = -\frac{1}{\lambda}\left(f_\alpha - f_\alpha^{(eq)} \right). \tag{5.2}$$

(5.2) differs from (2.7) as the number density term is considered to be non-dimensionalized to a value of unity, and the equation is in vector notation instead of tensor notation.

This equation can be discretized into the lattice Boltzmann equation as follows.

$$\frac{f_\alpha(x,t+\delta t)-f_\alpha(x,t)}{\delta t}+c\frac{f_\alpha(x+\delta x_\alpha,t+\delta t)-f_\alpha(x,t+\delta t)}{\delta x_\alpha}=-\frac{f_\alpha(x,t)-f_\alpha^{eq}(x,t)}{\tau\varepsilon} \tag{5.3}$$

$\lambda=\tau_f\varepsilon$ is substituted as τ_f is the collision frequency and ε is the Knudson number. This discretized equation can be simplified by assuming $c=\frac{\delta x_\alpha}{\delta t}$ to be the isothermal speed of sound, $c=\sqrt{3RT}$. This is the characteristic velocity at which the lattice particles propagate.

$$f_\alpha(x+\delta x_\alpha,t+\delta t)-f_\alpha(x,t)=-\frac{\delta t}{\tau_f\varepsilon}\left(f_\alpha(x,t)-f_\alpha^{eq}(x,t)\right) \tag{5.4}$$

Setting $\delta t=\varepsilon$, the final discretized form of the LBE is

$$f_\alpha(x+\delta x_\alpha,t+\delta t)=\left[1-\frac{1}{\tau_f}\right]f_\alpha(x,t)+\frac{1}{\tau_f}f_\alpha^{eq}(x,t)\,. \tag{5.5}$$

The LBE describes the changes in the probability density distribution functions, f_α, due to collisions. The collision frequency, τ_f, is a relaxation parameter that characterizes the nature of the collisions. Further on, the collision frequency will be related to the constitutive kinematic viscosity term.

As, was previously shown, the Boltzman equation using the linear BGK collision operator recovers the Navier-Stokes equations, which are the following:

$$\frac{\partial \rho}{\partial t} + \nabla \cdot (\rho \mathbf{v}) = 0 \tag{2.12}$$

$$\frac{\partial \rho \mathbf{v}}{\partial t} + \mathbf{v}\nabla \cdot \rho \mathbf{v} = -\nabla p - \nabla \cdot \bar{\bar{\boldsymbol{\pi}}}. \tag{2.13}$$

In order to recover the Navier-Stokes equations, the LBE needs to be expanded using the Chapman-Enskog procedure, Taylor-series expansion about δt, and an expansion of the time derivative as follows [9 and 12].

$$f_\alpha = \sum_{n=0}^{\infty} \varepsilon^n f_\alpha^{(n)} = f_\alpha^0 + \left[\varepsilon f_\alpha^1 + \varepsilon^2 f_\alpha^2 + ... \right] \qquad f_\alpha^0 = f_\alpha^{eq}$$

$$f_\alpha \left(x + \delta x_\alpha, t + \delta t \right) = f_\alpha \left(x + \delta x_\alpha, t \right) + \frac{\partial f \left(x + \delta x_\alpha, t \right)}{\partial t} \frac{\delta t}{1!} + \frac{\partial^2 f \left(x + \delta x_\alpha, t \right)}{\partial t^2} \frac{\delta t^2}{2!} + ...$$

$$\frac{\partial}{\partial t} = \sum_{n=0}^{\infty} \varepsilon^n \frac{\partial}{\partial t_n} = \frac{\partial}{\partial t_0} + \varepsilon \frac{\partial}{\partial t_1} + \varepsilon^2 \frac{\partial}{\partial t_2} + ...$$

These expansions for 1st and 2nd order of δt provide the following equations.

$$\left[\frac{\partial}{\partial t_0} + \mathbf{e}_\alpha \cdot \nabla \right] f_\alpha^0 = -\frac{f_\alpha^1}{\tau_f} \tag{5.6}$$

$$\frac{\partial f_\alpha^0}{\partial t_1} + \left(1 - \frac{1}{2\tau_f} \right) \left[\frac{\partial}{\partial t_0} + \mathbf{e}_\alpha \cdot \nabla \right] f_\alpha^1 = -\frac{f_\alpha^2}{\tau_f} \tag{5.7}$$

The $\mathbf{e}_\alpha$ is the characteristic velocity vector, corresponding to the direction of the characteristic speed, c. The first and second moments of these equations yield the following.

$$\frac{\partial}{\partial t} \left(\sum_\alpha f_\alpha^0 \right) + \nabla \cdot \left(\sum_\alpha \mathbf{e}_\alpha f_\alpha^0 \right) = 0 \tag{5.8}$$

$$\frac{\partial}{\partial t}\left(\sum_{\alpha}\mathbf{e}_{\alpha}f_{\alpha}^{0}\right)+\nabla\cdot\left(\Pi^{0}+\delta t\left(1-\frac{1}{2\tau_{f}}\right)\Pi^{1}\right)=O\left(\delta t^{2}\right) \tag{5.9}$$

$$\Pi^{n}=\sum_{\alpha}\mathbf{e}_{\alpha}\mathbf{e}_{\alpha}f_{\alpha}^{n}$$

The Π^{0} and Π^{1} terms must be modeled by using a proper equilibrium function, f_{α}^{eq}, in the lattice Boltzmann equation. Π^{0} contains first order terms while Π^{1} contains second order dissipation terms of the momentum equation. It's also important to note from the first and second moments that the equilibrium equation must correspond to the divergence terms in the Navier-Stokes equations.

$$\frac{\partial\rho}{\partial t}+\nabla\cdot(\rho\mathbf{v})=0 \tag{2.12}$$

$$\frac{\partial}{\partial t}(\rho\mathbf{v})+\nabla\cdot\left(\rho\mathbf{v}\mathbf{v}+p\bar{\mathbf{I}}\right)+\nabla\cdot\left(\rho\upsilon\bar{\mathbf{S}}\right)=0 \tag{5.10}$$

The momentum equation is re-defined in (5.10) in a form more conducive to the LBM formulation. $\bar{\mathbf{S}}=\nabla\mathbf{v}+(\nabla\mathbf{v})^{T}$ is the stress tensor, depicting the higher order dissipation effects of the momentum equation. [9] has shown that using the following as the equilibrium equation recovers these terms.

$$f_{\alpha}^{(eq)}=\rho w_{\alpha}[1+\frac{3}{c^{2}}\boldsymbol{e}_{\alpha}\cdot\mathbf{v}+\frac{9}{2c^{4}}(\boldsymbol{e}_{\alpha}\cdot\mathbf{v})^{2}-\frac{3}{2c^{2}}\mathbf{v}\cdot\mathbf{v}] \tag{5.11}$$

The term w_{α} is a weighting factor to be further defined based on the lattice structure for the fluid particles in LBM. The constraint of this equilibrium function with the lattice Boltzmann equation is that the Mach number must be .3 or less. If this constraint is

violated, the method will become less stable and less accurate. This means that the Navier-Stokes equations can be accurately modeled in the incompressible limit with the LBM.

Corresponding to the higher order term of the second moment equation, the equilibrium function, and the momentum equation, the kinematic viscosity can be calculated as a function of the collision frequency, τ_f.

$$\nu = \frac{\left(\tau_f - .5\right)}{3} c^2 \delta t \tag{5.12}$$

This relationship between the kinematic viscosity and collision frequency provides a physical relationship for the rate of collisions of particles at the molecular level. This relationship describes how viscosity is in fact defined by intermolecular collisions. This kinematic approach to simulating the Navier-Stokes equations demonstrates that the physical trends at the continuum level can be fundamentally described by intermolecular collisions at the molecular level.

The discretized PDF's are summed to compute both the density and momentum as follows.

$$\rho = \sum_{\alpha=1}^{N} f_\alpha \qquad \rho v_\alpha = \sum_{\alpha=1}^{N} e_\alpha f_\alpha$$

The characteristic velocity vector, $\mathbf{e}_\alpha$, is important in computing the momentum. The direction of these vectors, is determined by the lattice structure configuration of each molecule being modeled with LBM. This lattice structure can be developed multiple ways. The lattice structure is very important, as it impacts the accuracy of the LBM. With more lattice structures for each node, the LBM obtains greater accuracy. The problem with using many lattice structures for each node, is that it increases the computational requirements. A balance between accuracy and computational efficiency must be reached to obtain the most useful lattice structures. [9 and 12] demonstrates that for two dimensional flows the Q9D2 lattice structure is the most preferred, and that the

Q19D3 structure is preferred for three-dimensional flows. These lattice configurations have been numerically validated for their accuracy and stability. Figure 25 illustrates these lattice structures.

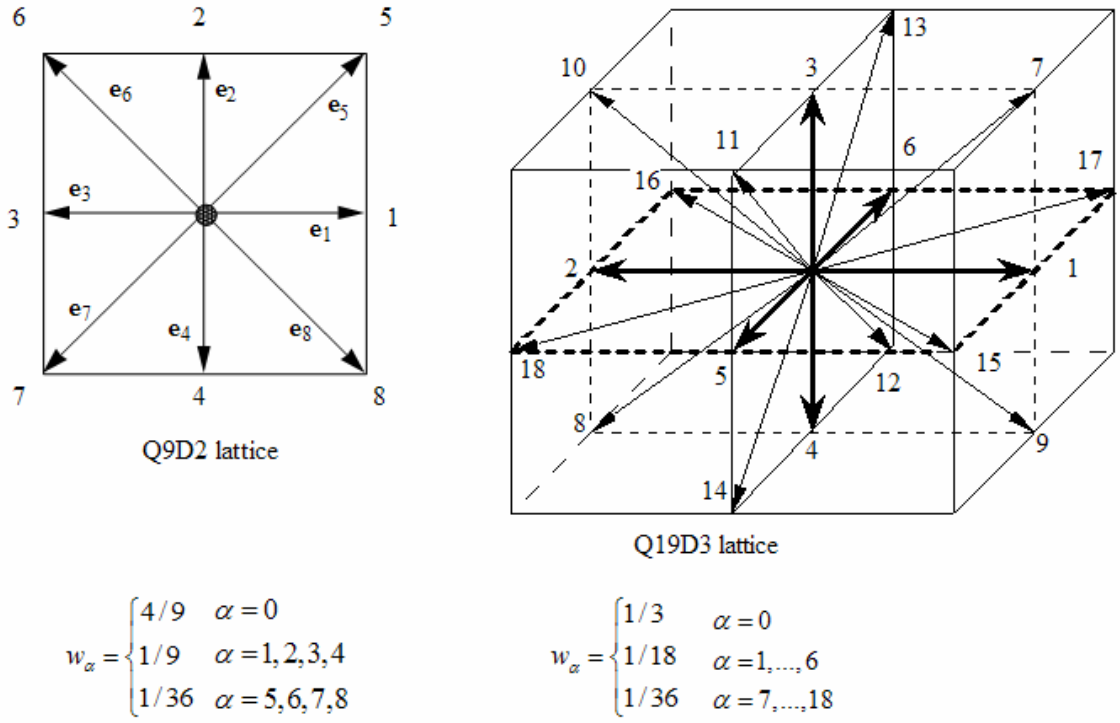

Figure 25. Q9D2 and Q19D3 Lattice Structures [12]

With the formulation of LBM demonstrated, the methodology needs further explanation. The lattice Boltzmann equation, equilibrium equation, lattice structures, and physical computations outline the major portions of the lattice Boltzmann method. However, the principles of lattice propagation must be noted. The lattice configuration shows that each particle is modeled with a combination of different lattices. In LBM, it is the propagation of each lattice that transports distribution changes due to collisions between particles. The characteristic velocity, as previously stated, describes the speed at which these lattices propagate. With this important concept defined, the outline of the

lattice Boltzmann method can be described as a three phase process of collision, streaming (propagation), and physical value calculations.

- 1.) Collision: $f_\alpha\left(x+\delta x_\alpha, t+\delta t\right)=\left[1-\frac{1}{\tau_f}\right]f_\alpha\left(x,t\right)+\frac{1}{\tau_f}f_\alpha^{eq}\left(x,t\right)$

- 2.) Streaming: $f_\alpha\left(x+e_\alpha\delta t,t\right)=f_\alpha\left(x,t\right)$

- 3.) Physical value calculation: $\rho=\sum_{\alpha=1}^{N}f_\alpha \qquad \rho v_\alpha=\sum_{\alpha=1}^{N}e_\alpha f_\alpha$

C. Magnetohydrodynamic Lattice Boltzmann Method (MHD-LBM)

1. Introduction to MHD-LBM

The Boltzmann equation used in modeling kinetic plasma theory, is

$$\frac{\partial f_\alpha}{\partial t}+\mathbf{v}\cdot\frac{\partial f_\alpha}{\partial \mathbf{r}}+\frac{q_\alpha}{m_\alpha}\left(\mathbf{E}+\mathbf{v}\times\mathbf{B}\right)\cdot\frac{\partial f_\alpha}{\partial \mathbf{v}}=\left(\frac{\partial f_\alpha}{\partial t}\right)_{coll}. \tag{4.1}$$

This is the same as the Boltzmann equation used in kinetic theory with the addition of the electromagnetic forces. Using the linear BGK collision operator, this Boltzmann equation can be written in the following form, where $\mathbf{a}$ is an acceleration term representing the electromagnetic force.

$$\frac{\partial f_\alpha}{\partial t}+\mathbf{c}\cdot\nabla f_\alpha+\mathbf{a}\cdot\nabla_c f_\alpha=-\frac{1}{\tau_f}\left(f_\alpha-f_\alpha^{(eq)}\right) \tag{5.13}$$

In plasma dynamics, the Boltzmann equation can be used as a two-fluid model for the separate species of ions and electrons, or a one-fluid model containing both considered to be a plasma species. This formulation will be for a one-fluid plasma

species. Using the one-fluid model, the magnetohydrodynamic equations can be obtained as follows.

$$\frac{\partial \rho}{\partial t} + \nabla \cdot (\rho \mathbf{v}) = 0 \tag{2.12}$$

$$\frac{\partial \rho \mathbf{v}}{\partial t} + \mathbf{v} \cdot \nabla \rho \mathbf{v} = -\nabla p - \nabla \left(\frac{B^2}{2\mu_0} \right) + \frac{1}{\mu_0} (\mathbf{B} \cdot \nabla) \mathbf{B} + \mu \nabla^2 \mathbf{v} \tag{4.63}$$

$$\frac{\partial \mathbf{B}}{\partial t} + \mathbf{v} \cdot \nabla \mathbf{B} = \mathbf{B} \cdot \nabla \mathbf{v} + \frac{\eta}{\mu_0} \nabla^2 \mathbf{B} \tag{3.23}$$

$$\nabla \cdot \mathbf{B} = 0 \tag{3.10}$$

Modeling of the MHD equations requires not only the model of the continuity and momentum equations, like in Navier-Stokes, but also a model for the evolution of the magnetic field. Therefore, MHD-LBM comprises of two sets of computations. MHD-LBM calculates the PDF (f_α), to find the value of density and momentum, and it also calculates the PDF's ($g_{\beta j}$) to model the magnetic induction equation. Dellar [12] developed the method in which the magnetic induction equation is calculated by the LBE.

In developing the formula of the momentum equation of MHD-LBM, there are two forms of the LBE that can be used. One form includes the Lorentz force effects through a body force formulation (BFF). This formulation calculates an external acceleration term corresponding to the acceleration term in (5.13). There are multiple ways in which to numerically incorporate this scheme. [11] uses this formulation with accuracy and stability. Another form, neglects the acceleration term in (5.13) and extends the equilibrium formulation (EEF) with the addition of the Maxwell's stress tensor. Physically, using EEF does not seem intuitively correct, as it doesn't directly include the external electromagnetic forces, shown in (5.13). However, this formulation has been developed by [12] and verified for accuracy and stability. EEF will be the method of choice.

2. Momentum Modeling in MHD-LBM

a. BFF Model of the Lorentz Force

When using BFF to model the Lorentz force, (5.5) is modified to include an external acceleration term.

$$f_\alpha\left(x+\delta x_\alpha, t+\delta t\right)=\left[1-\frac{1}{\tau_f}\right]f_\alpha\left(x,t\right)+\frac{1}{\tau_f}f_\alpha^{eq}\left(x,t\right)-\left(1-\frac{1}{2\tau_f}\right)\delta_t\mathbf{a}\bullet\nabla_e f_\alpha . \tag{5.14}$$

In this formula, the external acceleration term is modeled as

$$\mathbf{a}\cdot\nabla_e f_\alpha=-\frac{3w_\alpha\rho}{c^2}\left[\left(\mathbf{e}_\alpha-\mathbf{v}\right)+3\frac{\left(\mathbf{e}_\alpha\cdot\mathbf{v}\right)}{c^2}\mathbf{e}_\alpha\right]\cdot\left(\mathbf{j}\times\mathbf{B}\right). \tag{5.15}$$

This model is described in [11], as it has been developed to be used for external body forces in general. The equilibrium equation is the same as presented in the previous section. In addition to modifying the collision equation, the calculation of the momentum is also modified to include the Lorentz force in the summation.

$$\rho v_\alpha=\sum_{\alpha=1}^{N}e_\alpha f_\alpha+\left(\mathbf{j}\times\mathbf{B}\right)\frac{\delta_t}{2}$$

b. EEF Model of the Lorentz Force

The modeling of the momentum equation by using EEF only requires the equilibrium function to be modified. The LBE and calculation of the density and momentum stay the same as in the original hydrodynamic form of the LBE. The reason for this modification is because the Lorentz force in the momentum equation can be described as a Maxwell's stress divergence term.

$$\frac{\partial}{\partial t}(\rho \mathbf{v}) + \nabla \cdot \left(\rho \mathbf{v}\mathbf{v} + p\,\bar{\mathbf{I}} + \frac{1}{2\mu_0} B^2\,\bar{\mathbf{I}} - \frac{1}{\mu_0}\mathbf{B}\mathbf{B} \right) + \nabla \cdot \left(\rho \upsilon \bar{\mathbf{S}} \right) = 0 \tag{5.16}$$

Because the Maxwell's stress tensor can be added to the momentum equation as a divergence term, numerically, the Lorentz force can be included in the equilibrium equation as the following.

$$w_\alpha \rho \left(1 + \frac{3}{c^2} \boldsymbol{e}_\alpha \cdot \mathbf{v} + \frac{9}{2c^4} (\boldsymbol{e}_\alpha \cdot \mathbf{v})^2 - \frac{3}{2c^2} \mathbf{v} \cdot \mathbf{v} \right) + \frac{9}{2c^2 \mu_0} w_\alpha \left(\frac{1}{2} |B_\alpha|^2 |e_\alpha|^2 - (\mathbf{e}_\alpha \cdot \mathbf{B}_\alpha)^2 \right) \tag{2-D}$$

$$w_\alpha \rho \left(1 + \frac{3}{c^2} \boldsymbol{e}_\alpha \cdot \mathbf{v} + \frac{9}{2c^4} (\boldsymbol{e}_\alpha \cdot \mathbf{v})^2 - \frac{3}{2c^2} \mathbf{v} \cdot \mathbf{v} \right) + \frac{9}{2c^2 \mu_0} w_\alpha \left(\frac{1}{3} |B_\alpha|^2 |e_\alpha|^2 - (\mathbf{e}_\alpha \cdot \mathbf{B}_\alpha)^2 \right) \tag{3-D}$$

EEF is the method chosen for the MHD-LBM simulations because it is the easiest to implement, and the method is the most developed.

3. Magnetic Induction Modeling in MHD-LBM

Dellar [12] presents a method in which the magnetic induction equation is calculated by using an analogous lattice Boltzmann formulation.

$$\frac{\partial g_{\beta j}}{\partial t} + \Xi \cdot \nabla g_{\beta j} = -\frac{1}{\tau_g} \left(g_{\beta j} - g_{\beta j}^{(eq)} \right) \tag{5.17}$$

Physically, the evolution of the magnetic field is not described by kinetic theory. Numerically the LBE can model the magnetic induction equation because the magnetic induction equation is a form similar to that of the momentum equation (conservative hyperbolic equation). The following compares the two equations in their divergence forms.

$$\frac{\partial}{\partial t}(\rho \mathbf{v}) + \nabla \cdot \left(\rho \mathbf{v}\mathbf{v} + p\bar{\mathbf{I}} + \frac{1}{2\mu_0} B^2 \bar{\mathbf{I}} - \frac{1}{\mu_0}\mathbf{B}\mathbf{B} \right) + \nabla \cdot \left(\rho \upsilon \bar{\mathbf{S}} \right) = 0 \tag{5.16}$$

$$\frac{\partial \mathbf{B}}{\partial t} + \nabla \cdot (\mathbf{v}\mathbf{B} - \mathbf{B}\mathbf{v}) + \nabla \cdot \left(\frac{\eta}{\mu_0} \nabla \mathbf{B} \right) = 0 \tag{5.18}$$

The discretized form of the LBE for the magnetic field takes the same form as the previous hydrodynamic LBE (5.5).

$$\mathbf{g}_{\beta j}(x + \Xi_\beta \delta_t, t + \delta_t) = \left(1 - \frac{1}{\tau_g} \right) \mathbf{g}_{\beta j}(x,t) - \frac{1}{\tau_g} \mathbf{g}_{\beta j}^{(eq)}(x,t) \tag{5.19}$$

$\mathbf{g}_{\beta j}$ is the magnetic field PDF, Ξ the magnetic field PDF lattice speed, and τ_g is the magnetic field relaxation time. This equation is expanded in the same way as the original LBM equation using Chapman-Enskog, Taylor-series, and expansion of the time derivatives.

$$\mathbf{g}_{\beta j} = \sum_{n=0}^{\infty} \varepsilon^n \mathbf{g}_{\beta j}^{(n)} = \mathbf{g}_{\beta j}^0 + \left[\varepsilon \mathbf{g}_{\beta j}^1 + \varepsilon^2 \mathbf{g}_{\beta j}^2 + ... \right] \qquad \mathbf{g}_{\beta j}^0 = \mathbf{g}_{\beta j}^{eq}$$

$$\mathbf{g}_{\beta j}(x + \delta x_\alpha, t + \delta t) = \mathbf{g}_{\beta j}(x + \delta x_\alpha, t) + \frac{\partial \mathbf{g}_{\beta j}(x + \delta x_\alpha, t)}{\partial t} \frac{\delta t}{1!} + \frac{\partial^2 \mathbf{g}_{\beta j}(x + \delta x_\alpha, t)}{\partial t^2} \frac{\delta t^2}{2!} + ...$$

$$\frac{\partial}{\partial t} = \sum_{n=0}^{\infty} \varepsilon^n \frac{\partial}{\partial t_n} = \frac{\partial}{\partial t_0} + \varepsilon \frac{\partial}{\partial t_1} + \varepsilon^2 \frac{\partial}{\partial t_2} + ...$$

The magnetic field lattice Boltzmann equation is expanded to obtain the 2nd order of δt like the hydrodynamic lattice Boltzmann equation (LBE).

$$\frac{\partial}{\partial t} \left(\sum_\beta \Xi_\beta \mathbf{g}_{\beta j}^0 \right) + \nabla \cdot \left(\Lambda^0 + \delta t \left(1 - \frac{1}{2\tau_g} \right) \Lambda^1 \right) = O\left(\delta t^2 \right) \tag{5.20}$$

$$\Lambda^n = \sum_\beta \Xi_\beta \Xi_\beta \mathbf{g}^n_{\beta j}$$

Like for the case of modeling Navier-Stokes, this equation includes both first and second order terms in which the second order term is a resistive term. An appropriate equilibrium function must be used that will retain the terms in equation (5.17). However, there is an important difference in the way that the equilibrium function models the magnetic induction versus momentum. The magnetic induction equation contains anti-symmetric divergence terms, while the momentum equation contains symmetric divergence terms.

- $\mathbf{vB} - \mathbf{Bv}$ Anti-Symmetric Magnetic Induction Divergence Term

- $\rho \mathbf{vv} + p\bar{\mathbf{I}} + \frac{1}{2\mu_0} B^2 \bar{\mathbf{I}} - \frac{1}{\mu_0} \mathbf{BB}$ Symmetric Momentum Divergence Terms

From this difference, the magnetic field variables are calculated differently than the fluid variables. Dellar [12] deals with this issue by calculating each component of the magnetic field separately, each being modeled by it's own PDF $\mathbf{g}_{\beta j}$. Dellar [12] found the most suitable equilibrium function that recovers the terms of the magnetic induction equation, to be

$$\mathbf{g}^{(eq)}_{\beta j} = w_\beta \left[\mathbf{B}_j + \frac{4}{c} \left(v_i B_j - B_i v_j \right) \right]. \tag{5.21}$$

With the second moment of the magnetic field LBE satisfying the magnetic induction equation, the magnetic diffusivity, $\frac{\eta}{\mu_0} = \sigma$ can be related to the magnetic field relaxation parameter in the same way that the kinematic viscosity is related to the collision frequency.

$$\sigma = \frac{\left(\tau_g - .5\right)}{3} c^2 \delta t \quad \text{(2-D)} \qquad \sigma = \frac{\left(\tau_g - .5\right)}{4} c^2 \delta t \quad \text{(3-D)} \tag{5.22}$$

This relationship for the magnetic diffusivity does not relate to the relaxation parameter in the same physical way that the kinematic viscosity does. The relaxation parameter is a numerical value used to model the magnetic induction equation.

The lattice structure of the magnetic field PDF differs from that of the velocity field because the magnetic field is described by vector distribution functions, instead of scalar distribution functions. In the case of the velocity field, the scalar PDF describes all components of the velocity field. In the case of the magnetic field, each vector PDF describes a single component of the magnetic field. The use of a vector PDF, means that less information is carried by each magnetic field PDF. Therefore, a less complicated lattice structure is required to obtain acceptable accuracy for each magnetic field vector PDF. [12] demonstrates that for two dimensional flows the Q5D2 lattice structure is the most preferred, and that the Q7D3 structure is preferred for three-dimensional flows. These lattice configurations have been numerically validated for their accuracy and stability. The figure 26 illustrates these lattice structures.

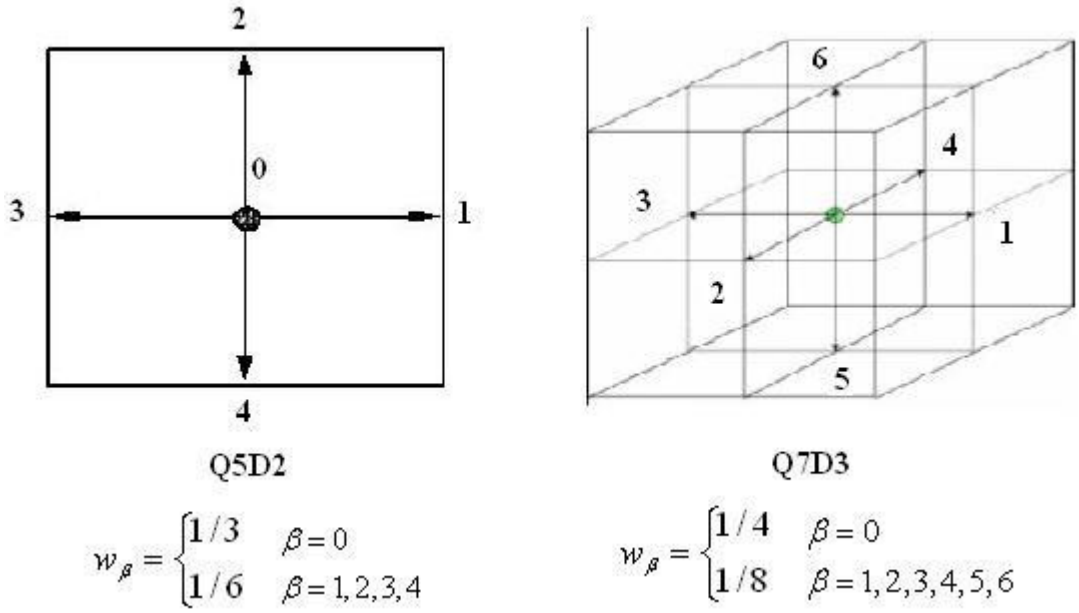

$$w_\beta = \begin{cases} 1/3 & \beta = 0 \\ 1/6 & \beta = 1,2,3,4 \end{cases}$$

$$w_\beta = \begin{cases} 1/4 & \beta = 0 \\ 1/8 & \beta = 1,2,3,4,5,6 \end{cases}$$

Figure 26. Q5D2 and Q7D3 Lattice Structures [12]

The value of the magnetic field is calculated by summing up all the magnetic field PDF's of the lattice structure.

$$\mathbf{B}_j = \sum_{\beta=1}^{M} \mathbf{g}_{\beta j} \qquad j = x, y, z$$

D. Multiple Relaxation Time Method

Previously, the hydrodynamic LBM formulation used a single relaxation time (SRT) parameter. This refers to using a single parameter for τ_f or τ_g. The SRT method works well for flows of simple geometry and very low Reynolds numbers. A multi-relaxation time (MRT) method, was developed to enhance numerical stability, increase the Reynolds number limit, and improve accuracy [43 and 44]. This method redefines the PDF's in terms of different moments, $|m\rangle$, of the Boltzmann equation, each using a specific relaxation parameter. The following shows the formulation of MRT-LBM model expressing the terms in a Dirac notation.

$$\left|f_\alpha\left(\mathbf{x}+\mathbf{e}_\alpha\delta t, t+\delta t\right)\right\rangle - \left|f_\alpha\left(\mathbf{x},t\right)\right\rangle = -\mathrm{M}^{-1}\mathrm{S}\left(\left|m\left(\mathbf{x},t\right)\right\rangle - \left|m^{(0)}\left(\mathbf{x},t\right)\right\rangle\right) \tag{5.23}$$

M is the transformation matrix that computes a certain moment from the PDF's via the linear mapping M: $|m\rangle = \mathrm{M}|f\rangle$, and is constructed via $\mathrm{M} = \left[|m_\alpha\rangle\right]^{\mathrm{T}} = \left(|m_0\rangle,....,|m_{18}\rangle\right)^{\mathrm{T}}$ where the $\langle m|$ moments are orthogonalized by the Gram-Schmidt procedure. S is the diagonal relaxation matrix which contains different relaxation times for different moments. The values for both matrices are presented below and numerically verified in [43].

$$\mathrm{M} = \begin{pmatrix}
1 & 1 & 1 & 1 & 1 & 1 & 1 & 1 & 1 & 1 & 1 & 1 & 1 & 1 & 1 & 1 & 1 & 1 & 1 \\
-30 & -11 & -11 & -11 & -11 & -11 & -11 & 8 & 8 & 8 & 8 & 8 & 8 & 8 & 8 & 8 & 8 & 8 & 8 \\
12 & -4 & -4 & -4 & -4 & -4 & -4 & 1 & 1 & 1 & 1 & 1 & 1 & 1 & 1 & 1 & 1 & 1 & 1 \\
0 & 1 & -1 & 0 & 0 & 0 & 0 & 1 & -1 & 1 & -1 & 1 & -1 & 1 & -1 & 0 & 0 & 0 & 0 \\
0 & -4 & 4 & 0 & 0 & 0 & 0 & 1 & -1 & 1 & -1 & 1 & -1 & 1 & -1 & 0 & 0 & 0 & 0 \\
0 & 0 & 0 & 1 & -1 & 0 & 0 & 1 & 1 & -1 & -1 & 0 & 0 & 0 & 0 & 1 & -1 & 1 & -1 \\
0 & 0 & 0 & -4 & 4 & 0 & 0 & 1 & 1 & -1 & -1 & 0 & 0 & 0 & 0 & 1 & -1 & 1 & -1 \\
0 & 0 & 0 & 0 & 0 & 1 & -1 & 0 & 0 & 0 & 0 & 1 & 1 & -1 & -1 & 1 & 1 & -1 & -1 \\
0 & 0 & 0 & 0 & 0 & -4 & 4 & 0 & 0 & 0 & 0 & 1 & 1 & -1 & -1 & 1 & 1 & -1 & -1 \\
0 & 2 & 2 & -1 & -1 & -1 & -1 & 1 & 1 & 1 & 1 & 1 & 1 & 1 & 1 & -2 & -2 & -2 & -2 \\
0 & -4 & -4 & 2 & 2 & 2 & 2 & 1 & 1 & 1 & 1 & 1 & 1 & 1 & 1 & -2 & -2 & -2 & -2 \\
0 & 0 & 0 & 1 & 1 & -1 & -1 & 1 & 1 & 1 & 1 & -1 & -1 & -1 & -1 & 0 & 0 & 0 & 0 \\
0 & 0 & 0 & -2 & -2 & 2 & 2 & 1 & 1 & 1 & 1 & -1 & -1 & -1 & -1 & 0 & 0 & 0 & 0 \\
0 & 0 & 0 & 0 & 0 & 0 & 0 & 1 & -1 & -1 & 1 & 0 & 0 & 0 & 0 & 0 & 0 & 0 & 0 \\
0 & 0 & 0 & 0 & 0 & 0 & 0 & 0 & 0 & 0 & 0 & 0 & 0 & 0 & 0 & 1 & -1 & -1 & 1 \\
0 & 0 & 0 & 0 & 0 & 0 & 0 & 0 & 0 & 0 & 0 & 1 & -1 & -1 & 1 & 0 & 0 & 0 & 0 \\
0 & 0 & 0 & 0 & 0 & 0 & 0 & 1 & -1 & 1 & -1 & -1 & 1 & -1 & 1 & 0 & 0 & 0 & 0 \\
0 & 0 & 0 & 0 & 0 & 0 & 0 & -1 & -1 & 1 & 1 & 0 & 0 & 0 & 0 & 1 & -1 & 1 & -1 \\
0 & 0 & 0 & 0 & 0 & 0 & 0 & 0 & 0 & 0 & 0 & 1 & 1 & -1 & -1 & -1 & -1 & 1 & 1
\end{pmatrix}$$

$$S = diag\left(0, s_1, s_2, 0, s_4, 0, s_4, 0, s_4, s_9, s_2, s_9, s_2, s_9, s_9, s_9, s_{16}, s_{16}, s_{16}\right)$$
$$= diag\left(0, s_e, s_\varepsilon, 0, s_q, 0, s_q, 0, s_q, s_\nu, s_\pi, s_\nu, s_\pi, s_\nu, s_\nu, s_\nu, s_m, s_m, s_m\right)$$

The values of these relaxation parameters are chosen as the following because of their optimizing effects on the stability of the model [43].

$s_1 = 1.19$ $\quad$ $s_2 = s_{10} = 1.4$ $\quad$ $s_4 = 1.2$ $\quad$ $s_{16} = 1.98$

With the MRT method formulated, the next step is to adapt its use for MHD-LBM. The lattice Boltzmann equation for the physical flow field is adapted. Currently there are no methods that use MRT to model the magnetic field lattice Boltzmann equation, using

the EEF scheme. To adapt MRT with the MHD-LBM, using EEF, the equilibrium function is separated into the velocity field and magnetic field parts. The velocity field parts are redefined in terms of moments, using the MRT method. The Maxwell's stress portion is modeled using the SRT formulation with a constant collision frequency.

$$\left[f_\alpha(x+e_\alpha\delta_t,t+\delta_t)-f_\alpha(x,t)\right]=-\mathrm{M}^{-1}\mathrm{S}\left[m_\alpha(x,t)-m_\alpha^{(eq)}(x,t)\right]+\frac{1}{\tau_f}f_{B\alpha}^{(eq)} \tag{5.24}$$

$$f_{B\alpha}^{(eq)}=\frac{9}{2}w_\alpha\left(\frac{1}{3}\left|B_\alpha\right|^2\left|e_\alpha\right|^2-\left(\mathbf{e}_\alpha\cdot\mathbf{B}_\alpha\right)^2\right) \quad \text{(3-D)}$$

$$f_{B\alpha}^{(eq)}=\frac{9}{2}w_\alpha\left(\frac{1}{2}\left|B_\alpha\right|^2\left|e_\alpha\right|^2-\left(\mathbf{e}_\alpha\cdot\mathbf{B}_\alpha\right)^2\right) \quad \text{(2-D)}$$

Using MRT, as shown, attains good agreement with the SRT version, and it stays more stable and accurate at higher Reynolds numbers than SRT. Figure 27 shows results for the axial centerline velocity of a 3-D RJ at Reynolds number of 10 and 25; a magnetic Reynolds number of 5, and with an externally applied magnetic field generated by a circular current loop. The details of the MHD RJ flow simulation are provided later. This comparison between SRT and MRT shows that at the lower Reynolds number of 10, both methods produce very close results. At Reynolds number 25, there is a notable difference in the results. The results for SRT agree with MRT initially right as it exits the inlet, but then it has a fluctuation and then returns to having close agreement with MRT. At a low Reynolds number of 25, where the flow is laminar, this type of fluctuation should not occur. This fluctuation is numerical and corresponds to a lack of stability and accuracy in the SRT method at Reynolds number 10. The smoothness of the axial velocity decay, shown by the MRT method, demonstrates the greater stability and accuracy properties of the MRT method. This demonstration corresponds to the results and conclusion of the MRT method analysis by [43].

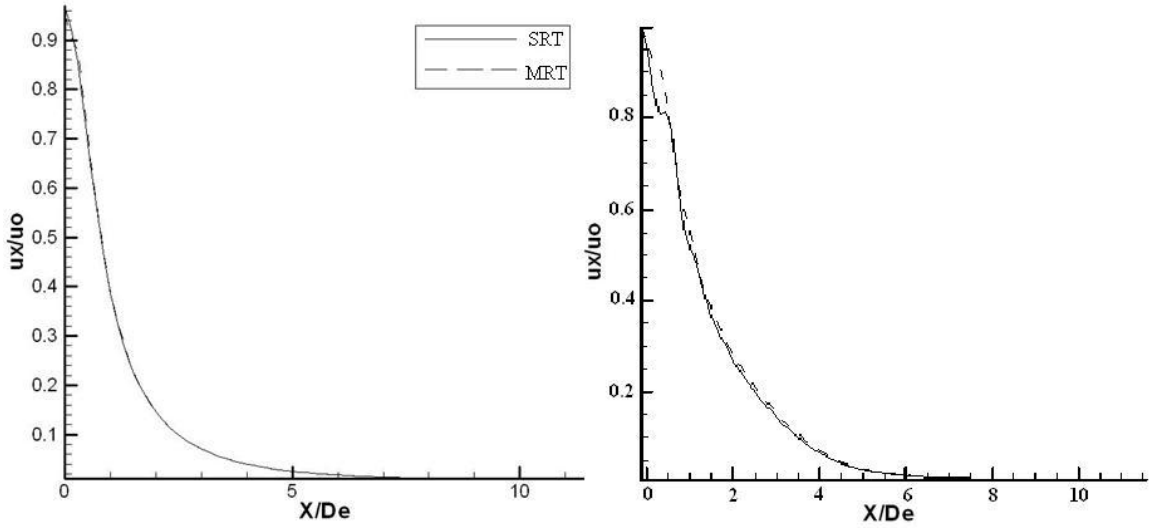

Figure 27. Comparison of Stability and Accuracy between SRT and MRT MHD-LBM Formulations

More comparisons of the stability properties between SRT and MRT are provided later in this chapter. Overall, this MRT MHD-LBM provides a robust and accurate method of simulating different types of MHD flows.

E. 2-D Hartmann Channel Flow Verification

The 2-D Hartmann channel flow case is a simple way of verifying MHD-LBM because it can be analytically solved [12].

1. 2-D Hartmann Channel Flow Problem

The 2-D Hartmann channel flow case is of interest in liquid metal flows through channels. The test case is for a channel of conducting fluid at a steady and fully developed state with a constant pressure gradient and uniformly applied external magnetic field in the non-axial direction. The channel walls are insulated. With all these conditions, the Hartmann flow problem and its analytical solution for $\mathbf{B} = \left(B_x(x), B_0\right)$ and $\mathbf{v} = \left(v_x(x), 0\right)$ become the following.

$$B_0 \frac{dB_x}{dx} + \rho_0 \nu \frac{d^2 v_x}{dx^2} + F = 0 \tag{5.25}$$

$$B_0 \frac{du_x}{dx} + \eta \frac{d^2 b_x}{dx^2} = 0 \tag{5.26}$$

$$B_x(x) = \frac{FL}{B_0}\left(\frac{\sinh(Hx/L)}{\sinh(H)} - \frac{x}{L} \right) \tag{5.27}$$

$$v_x(x) = \frac{FL}{\sqrt{\rho_0} B_0} \sqrt{\frac{\eta}{\nu}} \coth(H) \left(1 - \frac{\cosh(Hx/L)}{\cosh(H)} \right) \tag{5.28}$$

These solutions are derived by Dellar [12]. F is the constant body force for the pressure gradient effect. B_0 is a constant external magnetic field applied in the non axial direction. The length across the channel is 2L, from –L to L.

Simulations are performed for Hartmann numbers of 5, 10, and 30, while the Reynolds and magnetic Reynolds numbers are kept equal to 10. The boundary conditions of the hydrodynamic PDF are solid wall boundaries for the walls, and periodic boundaries for the inlet and outlet. The boundary conditions for the magnetic field PDF are insulated boundaries for the walls and periodic boundaries for the inlet and outlet.

2. 2-D Hartmann Channel Flow Results and Comparison

The results of the 2-D Hartmann channel flow case, showing the axial velocity and magnetic field profiles in the transverse direction, are shown in figures 28 and 29. For each case, a plot of the analytical solution versus the numerical solution for the axial velocity profile and induced axial magnetic field profile are shown.

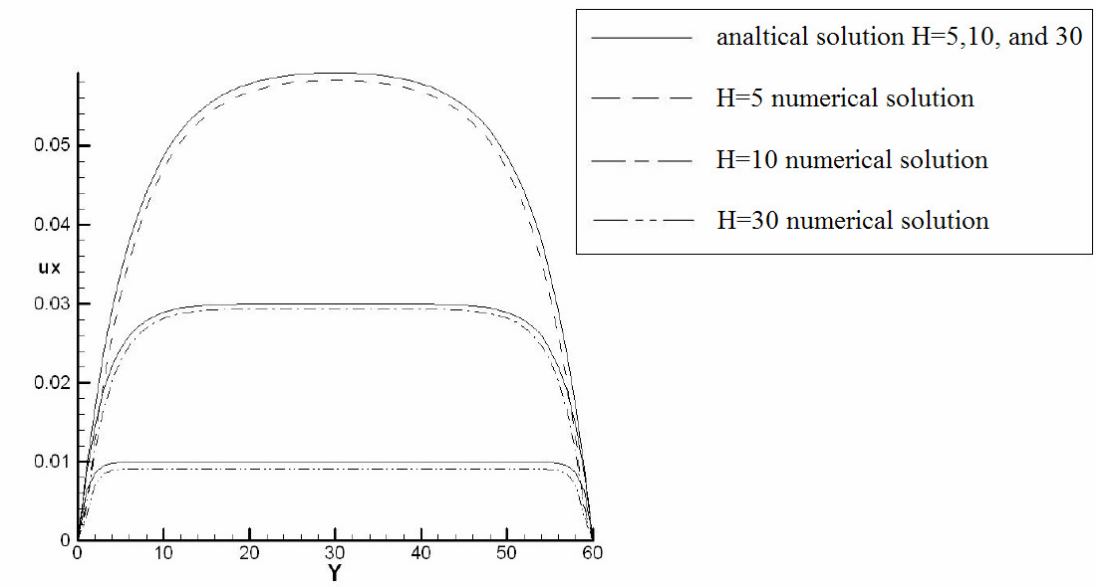

Figure 28. Axial Velocity Profile of 2-D Hartmann Channel Flow at various H

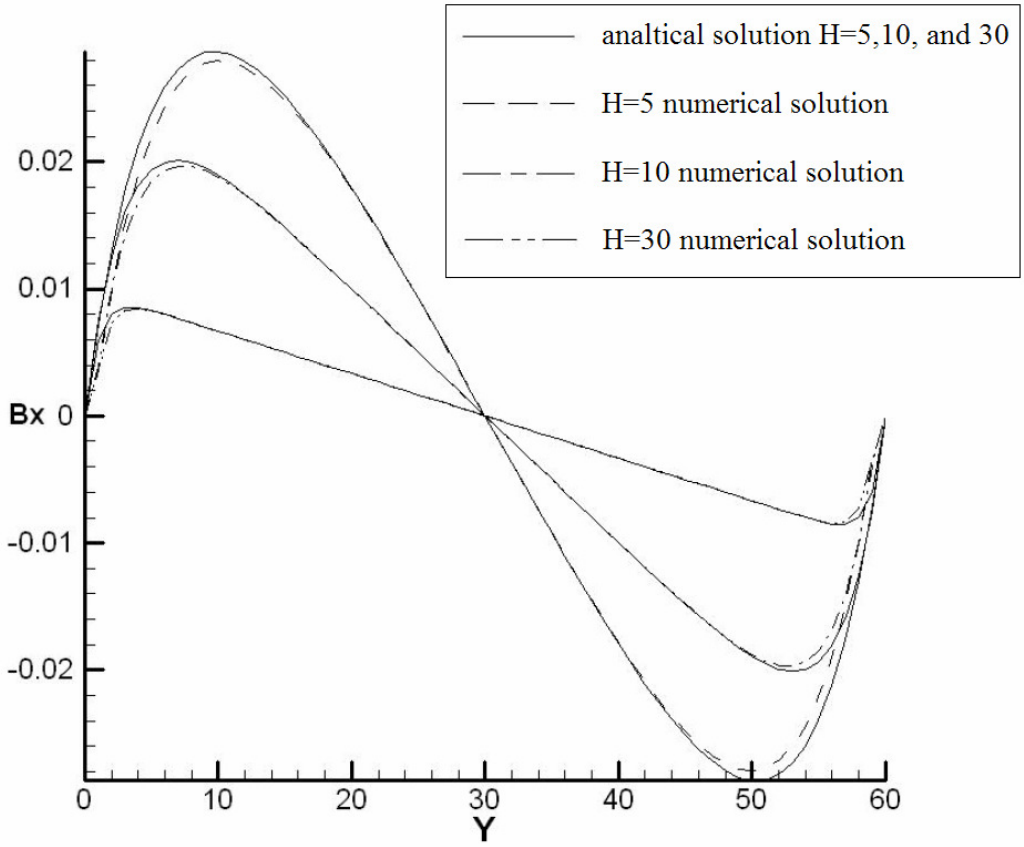

Figure 29. Axial Magnetic Field Profile of 2-D Hartmann Channel Flow at various H

The results in figures 28 and 29, show that the MHD-LBM, using EEF, performs with good accuracy. The physical trends of figures 28 and 29, show how the Hartmann layers (boundary layers) are inversely proportional to the Hartmann number. This trend is verified by theoretical analysis [5] and simulations [12]. This successful test case provides validation for the method, facilitating simulations of more complex MHD flows.

F. Three-Dimensional MHD Taylor-Green Vortex Test Case

This section analyzes the 3-D Taylor-Green vortex problem using the same MHD-LBM method with both SRT and MRT. An analysis between SRT and MRT methods shows that both methods are stable and their results agree for low Reynolds numbers. The SRT method, however, is more prone to instabilities than the MRT method at higher Reynolds numbers. The enhanced stability of the MRT method adds robustness to the MHD-LBM allowing for simulations of high intensity turbulent flow fields.

1. 3-D Taylor Green Vortex Problem

The Taylor-Green Vortex is useful system for studying the generation of small scales and the turbulence generated by three-dimensional vortex stretching. We study decaying isotropic turbulence starting from the Taylor-Green vortex initial conditions.

$$\mathbf{u} = \left[\sin(x)\cos(y)\cos(z), -\cos(x)\sin(y)\cos(z), 0\right] \qquad 0 \le x, y, x < 2\pi \qquad (5.29)$$

$$\mathbf{B} = \left[\sin(x)\sin(y)\cos(z), -\cos(x)\cos(y)\cos(z), 0\right] \qquad 0 \le x, y, x < 2\pi \qquad (5.30)$$

The magnetic and kinetic energies and enstrophies per unit volume are calculated as follows.

$$E_K = \frac{1}{2L^3}\int |u|^2 \, dx \qquad \text{(Kinetic Energy Decay)} \qquad (5.31)$$

$$E_M = \frac{1}{2L^3}\int |B|^2 \, dx \qquad \text{(Magnetic Energy Decay)} \qquad (5.32)$$

$$\Omega_K = \frac{1}{2L^3}\int |\nabla \times u|^2 \, dx \qquad \text{(Kinetic Enstrophy Decay)} \qquad (5.33)$$

$$\Omega_M = \frac{1}{2L^3}\int |\nabla \times B|^2 \, dx \qquad \text{(Magnetic Enstrophy Decay)} \qquad (5.34)$$

Enstrophy is a measure of vanishing vortex-stretching and resulting vorticity conservation (Ω_K) and its cause (Ω_M) and also measures the reduction of the dimensional order of MHD turbulence from 3-D to 2-D. Enstrophy, for the case of incompressible turbulence, corresponds with the dissipation of the system. The length of the computational domain is $L = 2\pi$ and periodic boundary conditions are employed. The grid size is 103^3 . The values of the kinematic viscosities and magnetic diffusivities are varied at $\nu = \sigma = 0.1, 0.05, 0.01$ and 0.006. Figure 30 shows the energy and enstrophy decays of the velocity and magnetic fields. The trendlines of each plot are for the cases of decreasing value of ν and σ from bottom to top in the following order: $\nu = \sigma = 0.1$, 0.05, 0.01, and 0.006.

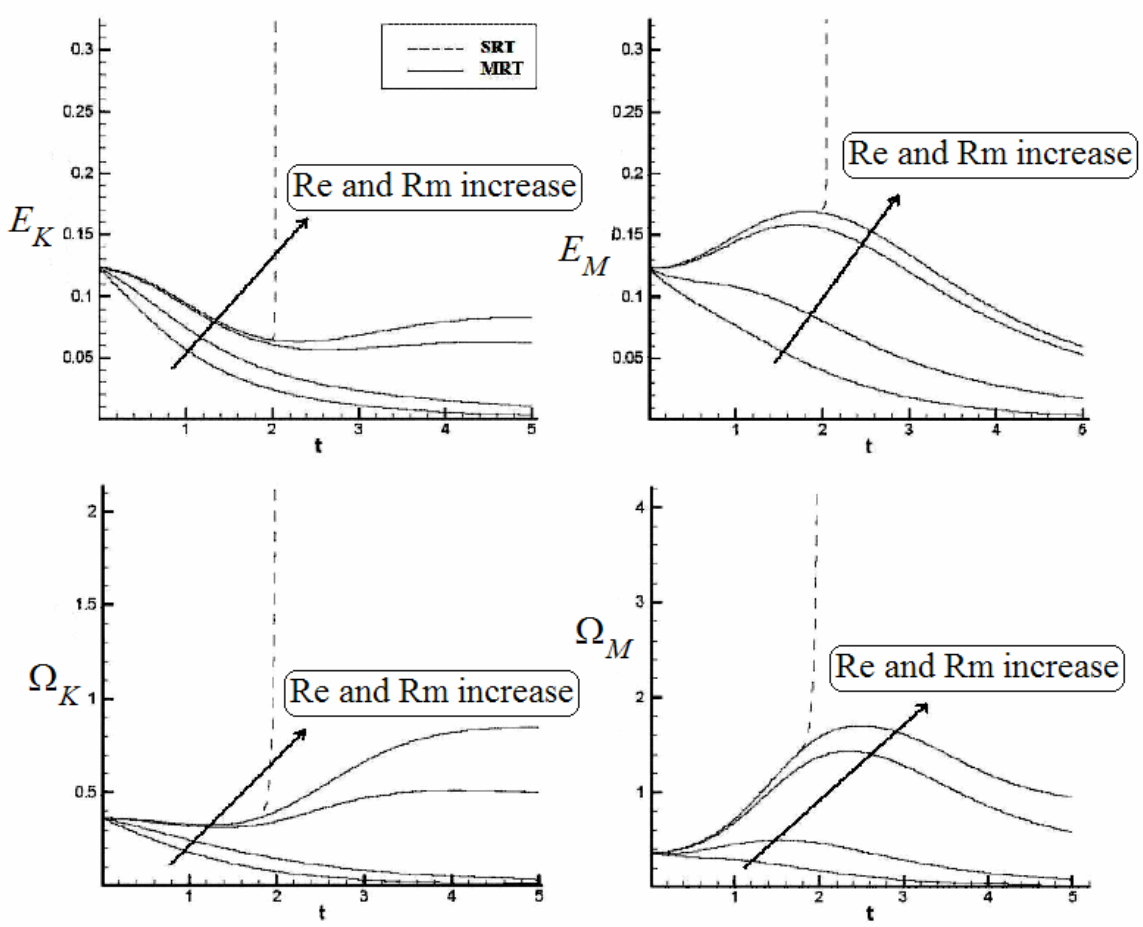

Figure 30. Comparisons of SRT vs. MRT Computations of Turbulent Kinetic/Magnetic Energy and Enstrophy

Fig. 30 shows that low ($\nu = \sigma = 0.1, 0.05$) and intermediate ($\nu = \sigma = 0.01$) Reynolds and magnetic Reynolds number turbulence simulations using both SRT and MRT approaches yield the same results and correct trends. As the Reynolds and magnetic Reynolds numbers increase, the kinetic and magnetic energy density decay trends change. This effect is due to the change in mechanism of energy transfer between magnetic and hydrodynamic parts. At low Reynolds and magnetic Reynolds numbers, the velocity and magnetic fields decay very rapidly as viscous effects dominate. The decay is nearly complete before any significant energy cascade or interaction can occur between the two fields. As the Reynolds and magnetic Reynolds number increase, the viscous effects are negligible at early times. The magnetic energy cascades rapidly to small scales drawing

energy from the kinetic mode. At higher Reynolds and magnetic Reynolds numbers, the early depletion in kinetic energy ($t < 2$) is due to transfer to magnetic energy and not due to viscous dissipation. At intermediate times ($2 < t < 4$), energy is transferred back to the kinetic mode from the magnetic field. Thus during this period, the kinetic energy actually increases and the viscous effects are still insignificant. At late times ($t > 5$), viscous effects start to be felt and both energies begin to decay.

For capturing the complex physics of high Reynolds and magnetic Reynolds number turbulence ($\nu = \sigma = 0.006$), the SRT method is less stable than the MRT method. The trends for both methods match until the magnetic dissipation becomes too large for the SRT method to resolve. At this point, the SRT method breaks down and yields unphysical values, while the MRT method continues to perform in a physically plausible manner. This analysis reaffirms that the MRT method increases the robustness of the MHD-LBM, allowing for simulations of higher Reynolds numbers.

G. Conclusion

This chapter had shown and validated the development of a MHD-LBM that is capable of solving complex MHD flows. MHD-LBM is a modified form of LBM that allows for MHD physics to be studied. By using the MHD-LBM, developed by Dellar [12], and improving its robustness with MRT, an effective method has been formulated for investigating significant MHD physics.

CHAPTER VI

ENERGY EXCHANGE AND CASCADING IN MAGNETOHYDRODYNAMIC DECAYING ISOTROPIC TURBULENCE

A. Introduction

Research in MHD turbulence has been widely performed in 3-D and 2-D. Energy decay, energy spectrum, helicity relationship, anisotropy, and cascade have all been major subjects of MHD turbulence. Shebalin [45-48] and Montgomery [48-51] have shown that a strong mean magnetic field can influence the evolution of flow field structures of an initial isotropic flow field to become anisotropic. Under the influence of a strong mean magnetic field, 3-D turbulent flow fields can exhibit 2-D characteristics. Ting, Matthaeus, and Montgomery [49] have also demonstrated selective decay and dynamic alignment in MHD turbulence as a result from inequalities among the decay rates of kinetic energy, magnetic energy, and cross helicity. Energy decay and cascade have been investigated by Biskamp [52] showing that 3-D isotropic MHD turbulence is governed by similar dynamics as hydrodynamic turbulence with the most important difference being the inverse cascading of the magnetic helicity which shows how the helical magnetic field structures undergo an inverse cascade evolution versus the direct cascade evolution of kinetic helicity. Biskamp also shows that in 2-D, MHD turbulence is governed by different effects than hydrodynamic turbulence due to the enhanced influence of magnetic field on the flow field by the 2-D characteristics of the system.

MHD turbulence encompasses the study of turbulent velocity and magnetic fields. Hydrodynamic turbulence, alone is very difficult to model and understand physically. There are several modes of flow field instability related to fluid viscosity and external characteristics such as heat transfer, pressure gradient, Mach number, and rough external surfaces. All of these factors can influence the onset of instability and turbulence. With the presence of a magnetic field, several more modes exist that deal with slow and fast magneto-sonic waves, and Alfven waves. The added complexity makes modeling and simulations a great challenge. Therefore, it is useful to simplify the system to study

certain turbulence phenomena. For this task a MHD-LBM is used to simulate incompressible homogeneous MHD turbulence at a low Taylor Reynolds and a magnetic Reynolds number of 45. From these simulations, physical effects can still be studied in order to improve the understanding of the physical mechanisms and promote more capable future MHD turbulence models.

MHD turbulence is characterized by the interaction between the flow field coherent structures and the magnetic field. The magnetic field presence exerts an external Lorentz force, which can also be described by magnetic pressure and tension forces. The type of magnetic field effect is typified by the magnetic field configuration. The effect of an external uniform magnetic field and initial random turbulent magnetic field are investigated in order to better understand the MHD turbulence processes. These Lorentz forces, depending on the magnetic field configuration, have the ability to manipulate the coherent structures by generating flows against or in similar manner to the natural hydrodynamic tendencies. The Lorentz force also has the capability of redistributing momentum and energy in the system between the kinetic and magnetic energy modes. Through these effects on energy exchange and vortex structures, the key inertial turbulence driving mechanisms can be weakened or strengthened.

B. MHD Turbulence Physics

The key magnetic field related processes behind incompressible MHD turbulence are all linked to the magnetic tension force component of the Maxwell stress tensor. This Maxwell stress tensor component plays a dominant role in the evolution of vortex structures which manipulate the energy cascade processes. As will be explained in more detail later, this energy cascade process is one of the most important defining characteristics of turbulence. This process outlines the manner in which energy travels between the different vortex eddies of the turbulent fluid, describing the key basic physical processes taking place. The magnetic tension's effect will be quite different between the case of a uniform applied magnetic field and an initial random magnetic field. The difference between these cases arises out of the characteristics of directionality and fluctuation gradients.

1. Energy Spectrum and MHD Turbulence Processes

Turbulence is characterized by a wide disparity of momentum caused by large dominance of inertial forces in the flow over the viscous forces, which lead to a more chaotic nature of the flow field. The chaotic motions create viscous eddies, that exist on many different length scales. The behavior of these viscous eddies will vary at different lengths scales, leading to the transfer of momentum to any direction across length scales. These chaotic motions of fluid particles cause a large amount of mixing in the flow field to occur in all directions, leading to redirection of momentum and thus greater equalization of momentum throughout the flow field (isotropy).

Another important concept is that of the energy cascade mechanism. This mechanism is directly related to the varying length scales throughout which the vortex eddies exist. By its very nature, turbulence consists of motions at different length scales. Even if the initial condition consists of only a few large scales, the cascade mechanism generates smaller or larger scale turbulence. The size of the largest scales of motion, are determined by the geometry, while the size of the smallest scales of motion are dictated by the viscosity. In Kolmogorov theory, the energy spectrum of turbulence gives the distribution of energy among turbulence vortices as function of vortex size [53]. Figure 31 illustrates the energy spectrum. It shows the distribution of turbulent kinetic energy (E) as a function of wavenumber (λ_K), which is analogous to the length scale characterized by the vortex size.

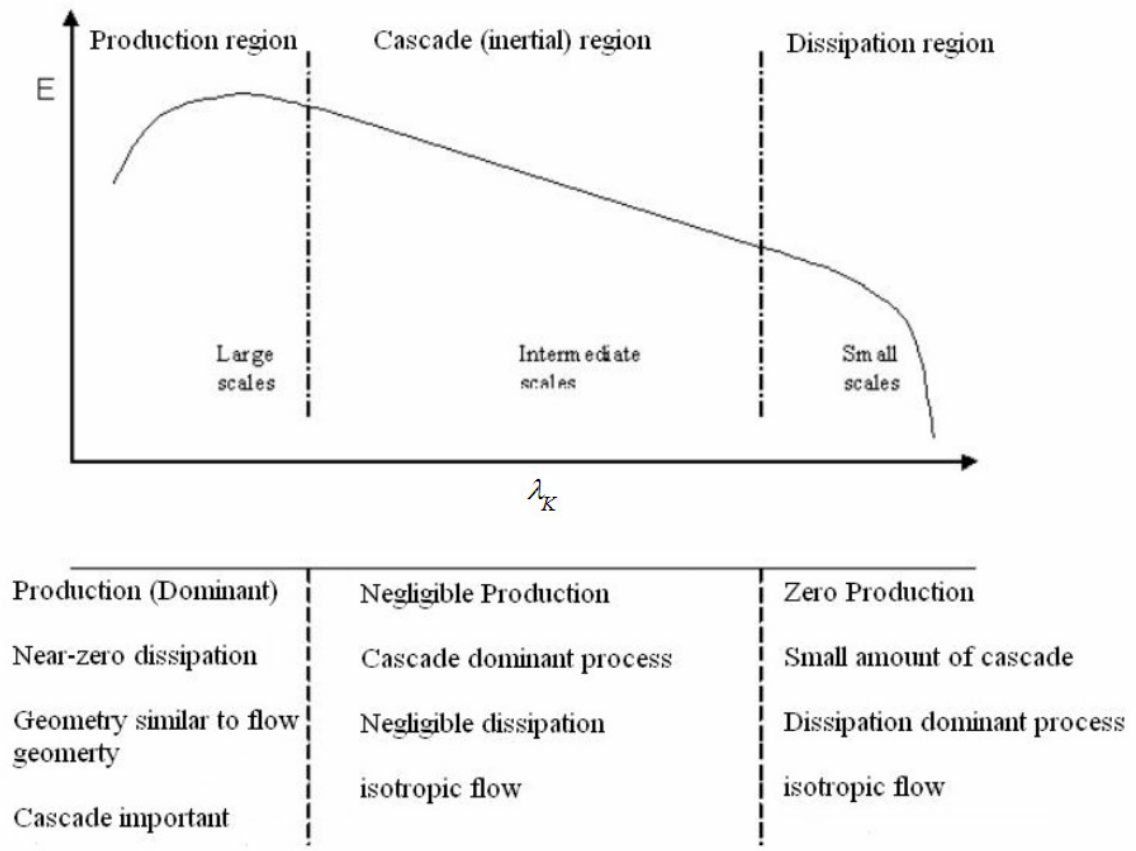

Figure 31. Turbulent Kinetic Energy Spectrum [53]

This energy spectrum is categorized in terms of the following three regions: (i) production, (ii) energy cascade (inertial), and (iii) energy dissipation.

The turbulent kinetic and magnetic energy is pumped into the spectrum at the large length scales through mean production forces (production region). The large length scales in this region correspond to large Reynolds numbers and negligible viscous dissipation effects. These large scale motions induce the generation of other length scales through the transmission of the turbulent kinetic and magnetic energy. The inertial or cascade dominated region, is not dominated by production and inertial forces, but the viscous dissipation is still negligible. Pressure and non-linear transport effects are the most dominant. In the cascade process, the turbulent kinetic and magnetic energies decrease steadily. Physically, the decrease of turbulent kinetic and magnetic energy can be related to the manner in which the fluctuating kinetic and magnetic field gradients

redistribute the momentum of the flow to all directions, isotropizing the flow field. This can also be associated to how the turbulent kinetic and magnetic energy redistributes its energy to different length scales. The dissipation region is dominated by viscous dissipation. Cascading is very minimal as the flow in the small scales has been mostly isotropized before dissipation becomes dominant.

The physical characteristics of these regions can be described in more detail through the MHD Reynolds stress equation.

$$\frac{D}{Dt}\left\langle u_i^{'}u_j^{'}\right\rangle + T_{kij} = \mathrm{P}_{ij} + \Pi_{ij} - \varepsilon_{ij} \tag{6.1}$$

$$\begin{aligned} T_{kij} &= \frac{\partial}{\partial x_k}\left\langle u_i^{'}u_j^{'}u_k^{'}\right\rangle + \frac{1}{\rho}\frac{\partial}{\partial x_k}\left\langle u_i^{'}p^{'}\right\rangle\delta_{jk} + \frac{1}{\rho}\frac{\partial}{\partial x_k}\left\langle u_j^{'}p^{'}\right\rangle\delta_{ik} \\ &+ \frac{1}{\mu_0\rho}\frac{\partial}{\partial x_k}\left\langle u_j^{'}B_k^{'}B_i^{'}\right\rangle + \frac{1}{\mu_0\rho}\frac{\partial}{\partial x_k}\left\langle u_i^{'}B_k^{'}B_j^{'}\right\rangle - \upsilon\frac{\partial^2}{\partial x_k\partial x_k}\left\langle u_i^{'}u_j^{'}\right\rangle \end{aligned} \tag{6.2}$$

$$\begin{aligned} \mathrm{P}_{ij} &= -\left\langle u_j^{'}u_k^{'}\right\rangle\frac{\partial\left\langle U_i\right\rangle}{\partial x_k} - \left\langle u_i^{'}u_k^{'}\right\rangle\frac{\partial\left\langle U_j\right\rangle}{\partial x_k} + \frac{1}{\mu_0\rho}\left\langle u_j^{'}B_k^{'}\right\rangle\frac{\partial\left\langle B_i\right\rangle}{\partial x_k} \\ &+ \frac{1}{\mu_0\rho}\left\langle u_i^{'}B_k^{'}\right\rangle\frac{\partial\left\langle B_j\right\rangle}{\partial x_k} + \frac{1}{\mu_0\rho}\left\langle u_j^{'}\frac{\partial B_i^{'}}{\partial x_k} + u_i^{'}\frac{\partial B_j^{'}}{\partial x_k}\right\rangle\left\langle B_k\right\rangle \end{aligned} \tag{6.3}$$

$$\Pi_{ij} = \left\langle\frac{p^{'}}{\rho}\left(\frac{\partial u_i^{'}}{\partial x_j} + \frac{\partial u_j^{'}}{\partial x_i}\right)\right\rangle - \left\langle\frac{B_k^{'}}{\mu_0\rho}\left(\frac{\partial u_j^{'}}{\partial x_k}B_i^{'} + \frac{\partial u_i^{'}}{\partial x_k}B_j^{'}\right)\right\rangle \tag{6.4}$$

$$\varepsilon_{ij} = 2\nu\left\langle\frac{\partial u_i^{'}}{\partial x_j}\frac{\partial u_j^{'}}{\partial x_i}\right\rangle \tag{6.5}$$

Where $\mathrm{p} = \left(\mathrm{p}_{\mathrm{thermo}} + \frac{\mathrm{B}^2}{2\mu_0}\right)$ is the total pressure, which includes both thermodynamic and magnetic pressure components.

The MHD Reynolds stress equation describes the evolution of the turbulent kinetic energy. This equation identifies important terms in MHD turbulence. The four major terms are the transport terms (T_{kij}), production terms (P_{ij}), pressure-rate-of-strain tensor (Π_{ij}), and the viscous dissipation term (ε_{ij}) [37]. In turbulence, there are two primary processes: (i) forcing and (ii) response [53]. Forcing processes are driven by linear mean inertial effects, $\left(\frac{\partial \langle u_j \rangle}{\partial x_k}, \frac{\partial \langle B_j \rangle}{\partial x_k}, \langle B_k \rangle \right)$. Response processes are characterized by nonlinear turbulent forces.

The production tensor contains forcing processes that add energy to the system at the large length scales of the production region. The type of forcing is dependent on the mean velocity and magnetic fields and has the effect of anisotropizing the turbulent flow. This means that forcing causes direction dependent strain to occur.

The transport terms (T_{kij}) produce non-linear inertial effects. All have only fluctuating components and gradients, corresponding to turbulent response processes. Unlike their mean counterparts, the non-linear fluctuating terms have an isotropizing effect on the turbulent flow field.

The pressure rate of strain term (Π_{ij}), a type of response mechanism, is the collective effect of inertia, thermodynamic, and magnetic pressure on a fluid element of the remainder of fluid. As indicated above, the pressure term includes normal hydrodynamic and magnetic pressure and forces, $\mathrm{p} = \left(\mathrm{p}_{\mathrm{thermo}} + \frac{\mathrm{B}^2}{2\mu_0} \right)$. Both thermodynamic and magnetic pressure exert the same type of force, except the thermodynamic pressure is generated by the fluid's internal energy while magnetic pressure is generated by the Lorentz force. The pressure-rate-strain-tensor is also characterized by turbulent inertial effects $\left(\frac{\partial u_i'}{\partial x_j} \right)$, which unlike mean inertial effects do not anisotropize the flow. Pressure has both linear and nonlinear characteristics that isotropize the turbulent flow field. These separate characteristics allow the pressure to be

decomposed into rapid (linear) and slow (nonlinear) pressure terms. The rapid pressure term is dominant in the production region, while the slow pressure is dominant in the cascade region. By isotropizing the turbulent flow field, what is meant is that pressure, which is not directional by its very nature, will lessen the dependence of direction on the strain and stress in the flow field. This can be easily derived as pressure provides elasticity to the flow by redirecting momentum of the flow to all directions. The momentum is redirected because pressure's isotropizing effect will equalize the distribution of fluid particles in the flow.

The viscous dissipation (ε_{ij}) term, a nonlinear processes, characterizes the length scale at which the turbulent processes are dissipated. At smaller values of kinematic viscosity or higher Reynolds numbers, the length scale at which turbulent kinetic energy is dissipated decreases.

Kinetic energy cascade can either be direct or inverse. In direct cascade, the large scale motions generate small scale motions. In inverse cascade, large scale motions are generated by smaller scale motions. Length scales are important in the study of turbulence because while turbulence appears to be chaotic on large length scales, at smaller length scales, turbulence is much smoother and easier to understand and predict. Overall, it is energy cascade and redirection of momentum that will cause turbulence to appear random and chaotic.

In conventional incompressible turbulence, the cascade will be direct or forward with large scale motions transferring energy to small scale motions. This follows Richardson's description [53] where larger eddies are characterized as generating smaller eddies until the length scale is so small that all the turbulent kinetic energy is dissipated. In two-dimensional incompressible turbulence [54], the cascade is inverse, meaning that small scale motions generate larger scale motions. This phenomenon has been seen in MHD flows with strong uniform mean magnetic fields [45-51]. The cascade process provides a well-ordered description of the formation of eddies and coherent structures in a chaotic turbulent flow field.

In the studies presented in this paper, the only mean field presence is from the magnetic field only, and the turbulence is homogeneous. Because the cases studied are

for homogeneous turbulence, the transport terms are all negligible, $\frac{\partial}{\partial x}\langle\ \rangle \simeq 0$. The assumption of homogeneous turbulence means that averaged fluctuating quantities do not change in space. Therefore, the pressure strain rate term is the only important mechanism in the cascade region.

From a broad viewpoint, modeling turbulence requires both knowledge of the large scale and small scale phenomena. This is why turbulence is viewed at multiple length scales, as previously described. At the larger length scales, when inertial forces are dominant, the outer geometry of the system is important in dictating the geometry of the flow making the flow field easy to compute, however the model is difficult because of the chaotic nature in which the different flow effects can occur. However, at smaller length scales the flow geometry is dictated by universal flow effects. Because the effects are universal, the flow in this regime is easier to understand and model and more difficult to compute. Another important aspect of small length scale versus larger length scale turbulence is that the motion of fluid particles at small length scales are as likely to go in one direction as the other, demonstrating isotropy, while in larger lengths scales the motion of fluid particles is more directional.

2. Energy Decay Laws and Kinetic-Magnetic Energy Interaction

The decay laws for kinetic energy, magnetic energy, kinetic enstrophy, and magnetic enstrophy describe the lifetime of MHD turbulence. The kinetic and magnetic energy decay trends are influenced by the turbulent mixing along with kinetic-magnetic energy interaction. Both energies, without the presence of a source generation, decay at a rate dependent on the Reynolds and magnetic Reynolds number.

$$E_K = \frac{1}{2L^3}\int |u|^2\, dx \qquad \text{(Kinetic Energy Decay)} \qquad (5.30)$$

$$E_M = \frac{1}{2L^3}\int |B|^2\, dx \qquad \text{(Magnetic Energy Decay)} \qquad (5.31)$$

$$\Omega_K = \frac{1}{2L^3}\int \left|\nabla \times u\right|^2 dx \qquad \text{(Kinetic Enstrophy Decay)} \qquad (5.32)$$

$$\Omega_M = \frac{1}{2L^3}\int \left|\nabla \times B\right|^2 dx \qquad \text{(Magnetic Enstrophy Decay)} \qquad (5.33)$$

In the context of turbulence, the quantities *u* and *B* include both mean and fluctuating components.

Kinetic and magnetic energy have a mode of energy exchange between each other. This mode of energy exchange is through the Lorentz force acting on the fluid particles. The following evolution equations for kinetic and magnetic energy show this exchange term. Note that these equations are not written in the form composing of fluctuating and mean components. However, given that these are the fundamental evolution equations, the same physics still exist in the turbulence equations.

$$\frac{\partial}{\partial t}\left(\rho\frac{\mathrm{v}^2}{2}\right) = \mathbf{v}\cdot\nabla\left(\rho\frac{\mathrm{v}^2}{2} - p\right) + \mathbf{v}\cdot\left(\mathbf{j}\times\mathbf{B}\right) + \mathbf{v}\cdot\mu\nabla^2\mathrm{v} \qquad (6.6)$$

$$\frac{\partial}{\partial t}\left(\frac{\mathrm{B}^2}{2\mu_0}\right) = -\frac{\nabla}{\mu_0}\cdot\left(\mathbf{E}\times\mathbf{B}\right) - \eta j^2 - \mathbf{v}\cdot\left(\mathbf{j}\times\mathbf{B}\right) \qquad (6.7)$$

(6.7) is derived by taking the dot product between $\frac{\mathbf{B}}{\mu_0}$ and (3.23), and substituting Ohm's Law (3.13). The Lorentz force work term, $\mathbf{v}\cdot\left(\mathbf{j}\times\mathbf{B}\right)$, shows up in both equations, however they have opposing signs. Therefore, when both equations are summed into the total energy, the Lorentz force work cancels out. This shows how the Lorentz force work term is significant in manipulation of the magnetic and kinetic energies of a flow field. Depending on the sign of this work term, the kinetic/magnetic energy increases or decreases. This type of physical interaction between the kinetic and magnetic energies is

important in MHD generators and accelerators [1-4], which have the effect of either extracting or adding kinetic energy from a flow field by using magnetic field interaction. In MHD turbulence, the evolution of the Lorentz force work can be correlated to the decay of kinetic and magnetic energy.

Two parameters governing the manner of energy decay are the Reynolds and magnetic Reynolds number. Large Reynolds numbers correspond to stronger turbulence and more length scales (greater turbulent energy, energy cascade). Therefore, the rate of turbulent energy dissipation increases. Large magnetic Reynolds numbers correspond to greater interaction between the kinetic and magnetic energies.

3. Two-Dimensional Turbulence

The Kolmogorov description of turbulence applies for three-dimensional turbulence, however two-dimensional turbulence exhibits different trends. The reason for this difference between 2-D and 3-D turbulence is due to the lack of vortex stretching in 2-D turbulence [54]. The following demonstrates the difference in vorticity dynamics between 3-D and 2-D turbulence.

$$\frac{\partial \boldsymbol{\omega}}{\partial t} + \mathbf{v} \cdot \nabla \boldsymbol{\omega} = \nu \nabla^2 \boldsymbol{\omega} \qquad \text{(2-D)} \qquad (6.8)$$

$$\frac{\partial \boldsymbol{\omega}}{\partial t} + \mathbf{v} \cdot \nabla \boldsymbol{\omega} = \boldsymbol{\omega} \cdot \nabla \mathbf{v} + \nu \nabla^2 \boldsymbol{\omega} \qquad \text{(3-D)} \qquad (6.9)$$

The $\boldsymbol{\omega} \cdot \nabla \mathbf{v}$ term is the effect of vortex stretching, while the $\nu \nabla^2 \boldsymbol{\omega}$ term is the net rate of viscous diffusion of vorticity. If viscosity is neglected, then the two-dimensional evolution of vorticity of a particle is conserved, while the three-dimensional evolution of vorticity is dictated by vortex stretching.

$$\frac{D\boldsymbol{\omega}}{Dt} = 0 \qquad \text{(2-D)} \qquad (6.10)$$

$$\frac{D\boldsymbol{\omega}}{Dt} = \boldsymbol{\omega} \cdot \nabla \mathbf{v} \qquad \text{(3-D)} \qquad (6.11)$$

The conservation of enstrophy is derived by taking the dot product of the vorticity equation with vorticity.

$$\frac{\partial}{\partial t}\left(\omega^2\right) + \mathbf{v} \cdot \nabla\left(\omega^2\right) = 2\boldsymbol{\omega} \cdot \nu \nabla^2 \boldsymbol{\omega} \qquad \text{(2-D)} \qquad (6.12)$$

$$\frac{\partial}{\partial t}\left(\omega^2\right) + \mathbf{v} \cdot \nabla\left(\omega^2\right) = \boldsymbol{\omega} \cdot \left(\boldsymbol{\omega} \cdot \nabla \mathbf{v}\right) + 2\boldsymbol{\omega} \cdot \nu \nabla^2 \boldsymbol{\omega} \qquad \text{(3-D)} \qquad (6.13)$$

Neglecting the viscosity, the conservation of enstrophy for two and three-dimensional flows is as follows.

$$\frac{D}{Dt}\left(\omega^2\right) = 0 \qquad \text{(2-D)} \qquad (6.14)$$

$$\frac{D}{Dt}\left(\omega^2\right) = \boldsymbol{\omega} \cdot \left(\boldsymbol{\omega} \cdot \nabla \mathbf{v}\right) \qquad \text{(3-D)} \qquad (6.15)$$

By this relationship between 2-D and 3-D flows, a turbulent flow field can be characterized as two-dimensional whenever the enstrophy is conserved. The two-dimensional characteristic of the vorticity evolution equation also causes the kinetic energy to exhibit inverse cascade. By inverse cascade, what is meant is that the energy is passed on from small scale motions to large scale motions. In inverse cascading, vortices tend to merge into larger ones.

4. Anisotropy in MHD Turbulence

Turbulent flow fields under the influence of magnetic field effects can incur different physical trends which translate to two-dimensional and inverse cascading effects.

Under the influence of a magnetic field, the governing equations of momentum, energy, vorticity, and enstrophy change. The momentum and energy equations and their trends in MHD physics have already been described. The effects that MHD physics has on turbulence, however, can be described in more detail through the effect on vorticity, analogous to the description provided in the previous section.

$$\frac{\partial \boldsymbol{\omega}}{\partial t} + \mathbf{v} \cdot \nabla \boldsymbol{\omega} = -\mathbf{j} \cdot \nabla \mathbf{B} + \nu \nabla^2 \boldsymbol{\omega} \tag{6.16}$$

$$\frac{\partial \boldsymbol{\omega}}{\partial t} + \mathbf{v} \cdot \nabla \boldsymbol{\omega} = \boldsymbol{\omega} \cdot \nabla \mathbf{v} + \mathbf{B} \cdot \nabla \mathbf{j} - \mathbf{j} \cdot \nabla \mathbf{B} + \nu \nabla^2 \boldsymbol{\omega} \tag{6.17}$$

The conservation equations with viscosity neglected are the following.

$$\frac{D\boldsymbol{\omega}}{Dt} = -\mathbf{j} \cdot \nabla \mathbf{B} \tag{6.18}$$

$$\frac{D\boldsymbol{\omega}}{Dt} = \boldsymbol{\omega} \cdot \nabla \mathbf{v} + \mathbf{B} \cdot \nabla \mathbf{j} - \mathbf{j} \cdot \nabla \mathbf{B} \tag{6.19}$$

The overall rate of change of the particle vorticity is not only influenced by the vortex stretching and viscous diffusion, but also by the magnetic tension which occurs through a combination of current and magnetic field stretching.

Analogous to these equations the enstrophy is described as the following.

$$\frac{\partial}{\partial t}\left(\omega^2\right) + \mathbf{v} \cdot \nabla \left(\omega^2\right) = 2\boldsymbol{\omega} \cdot \left(-\mathbf{j} \cdot \nabla \mathbf{B}\right) + 2\boldsymbol{\omega} \cdot \nu \nabla^2 \boldsymbol{\omega} \quad \text{(2-D)} \tag{6.20}$$

$$\frac{\partial}{\partial t}\left(\omega^2\right) + \mathbf{v} \cdot \nabla \left(\omega^2\right) = 2\boldsymbol{\omega} \cdot \left(\boldsymbol{\omega} \cdot \nabla \mathbf{v}\right) + 2\boldsymbol{\omega} \cdot \left(\mathbf{B} \cdot \nabla \mathbf{j}\right) - 2\boldsymbol{\omega} \cdot \left(\mathbf{j} \cdot \nabla \mathbf{B}\right) + 2\boldsymbol{\omega} \cdot \nu \nabla^2 \boldsymbol{\omega} \quad \text{(3-D)} \tag{6.21}$$

Enstrophy is a measure of vanishing vortex-stretching and resulting vorticity conservation. Neglecting the viscosity, the conservation of enstrophy becomes the following.

$$\frac{D}{Dt}\left(\omega^2\right) = 2\boldsymbol{\omega}\cdot\left(-\mathbf{j}\cdot\nabla\mathbf{B}\right) \qquad \text{(2-D)} \qquad (6.22)$$

$$\frac{D}{Dt}\left(\omega^2\right) = 2\boldsymbol{\omega}\cdot\left(\boldsymbol{\omega}\cdot\nabla\mathbf{v}\right) + 2\boldsymbol{\omega}\cdot\left(\mathbf{B}\cdot\nabla\mathbf{j}\right) - 2\boldsymbol{\omega}\cdot\left(\mathbf{j}\cdot\nabla\mathbf{B}\right) \qquad \text{(3-D)} \qquad (6.23)$$

In MHD turbulence, both the two-dimensional and three dimensional vorticity equations have source terms. Because of this trend, 2-D and 3-D MHD turbulence have more similarities than 2-D and 3-D hydrodynamic turbulence [54]. In 2-D MHD turbulence, the turbulent kinetic energy does not always exhibit inverse cascading (2-D turbulence characteristics). However, inverse cascading can occur in 2-D along with 3-D MHD turbulence if a strong mean magnetic field is applied to the system [5,45-51]. A strong mean magnetic field presence provides directionality to the flow field, causing the vorticity strength to intensify in the direction of the applied mean magnetic field. For the case of 3-D MHD turbulence, the inverse cascading is synonymous with anisotropy of the turbulent flow field. The 3-D turbulence is driven towards two-dimensional characteristics. Figure 32 illustrates the anisotropizing effect on vortex structures in MHD turbulence. This figure depicts a random velocity field of random structures, being manipulated by a strong mean magnetic field over time to produce a directional set of vortex structures.

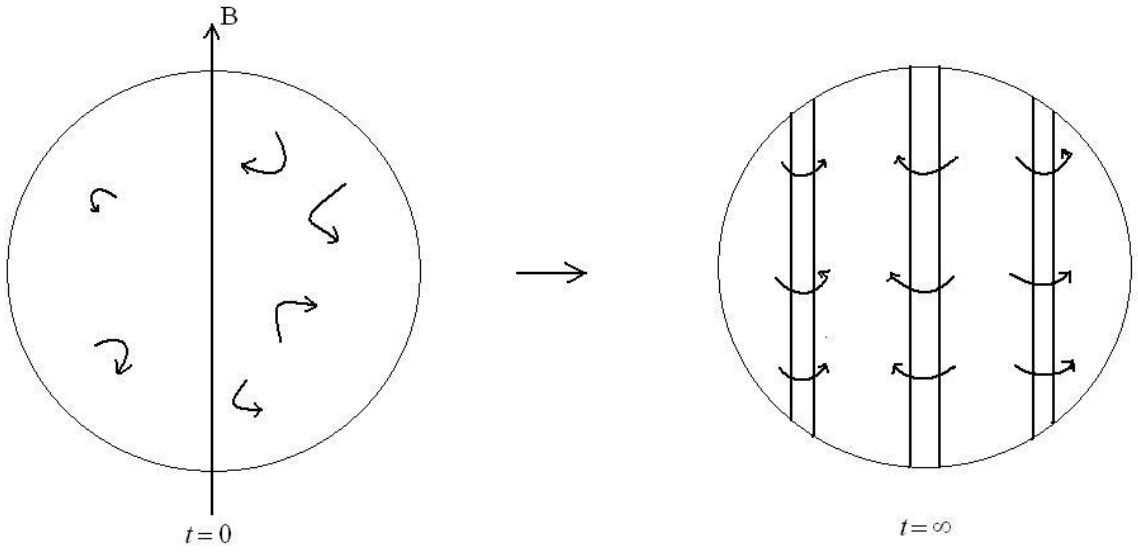

Figure 32. Anisotropic MHD Turbulence [5]

This effect is explained in detail by Davidson [5]. The magnetic tension term, exerted by this strong mean magnetic field, distorts the vorticity structure, as displayed in the vorticity equation above. In this case, the magnetic field and current density stretching terms will generate vorticity structures along with the vortex stretching mechanism. With a strong mean magnetic field, these mechanisms overwhelm the strength of the vortex stretching and create vortex structures more aligned with the mean magnetic field.

Knaepen, Kassinos, and Carati [55] further describe this term as the ratio of the large-eddy turnover time to the Joule time, which is the characteristic time scale for dissipation of turbulent kinetic energy by the action of the Lorentz force. The interaction parameter is also viewed as the measure of the ability of an imposed magnetic field to drive turbulence to a two-dimensional three-component state [55]. The Lorentz force causes the turbulent energy to become concentrated in directions independent of those aligned with the strong mean magnetic field. However, non-linear energy transfer from particle interactions, attempts to drive the flow to an isotropic state. This indicates that past a critical value of the interaction parameter, the Lorentz force is able to drive the turbulence to a state of two-dimensionality.

5. Strain-Rate Analysis in Turbulence

The type of strain on the vortex structures has been shown to describe the energy cascade process in hydrodynamic turbulence [56]. Straining of the vortex structures leads to narrower length scales, corresponding to the direct energy cascade characteristics. Compression of the structure leads to larger length scales, corresponding to inverse energy cascade characteristics.

In tensor notation, the strain-rate tensor is $S_{ij} = \frac{1}{2}\left(\frac{\partial u_i}{\partial x_j} + \frac{\partial u_j}{\partial x_i} \right)$. Numerical investigations have shown that in sufficiently strong hydrodynamic turbulent regimes, the eigenvalues of this tensor will have an approximate average ratio of $(\alpha : \beta : \gamma) \to (3 : 1 : -4)$ [56]. It has also been demonstrated that the vorticity will primarily align itself with the eigenvector of the rate of strain tensor that corresponds to the intermediate eigenvalue (β) [56]. The ratio of the eigenvalues shows that two of them will be positive with the third being negative. This trend is an indication of how the turbulent structure is incurring a straining effect, and thus direct cascade of kinetic energy. In the occurrence of inverse cascade, two of the eigenvalues would be negative, and incurring compression. From this physical trend, the ratio of the eigenvalues of the strain-rate tensor can indicate whether the energy cascade is direct or inverse. Alignment between vorticity and the rate of strain tensor can be computed by taking the dot product of the vorticity with the eigenvector of each eigenvalue and then normalized.

$$\frac{\boldsymbol{\omega} \cdot \boldsymbol{\lambda}}{\sqrt{\omega^2}\sqrt{\lambda^2}} = \cos\theta \quad \boldsymbol{\lambda} \text{ is the eigenvector} \qquad \boldsymbol{\omega} \text{ is the vorticity vector} \tag{6.24}$$

This formula produces values equal to $\cos\theta$. In this way, the angle θ corresponds to how closely aligned the vectors are. If $\cos\theta$ equals 1 or -1, then the vectors are parallel and aligned. If $\cos\theta$ equals zero, the vectors are perpendicular and thus not aligned.

In MHD turbulence, the importance of this analysis in determining energy cascade is diminished because of the extra magnetic field related terms that generate

vortex structures. Later on, the analysis of the vorticity alignment to the velocity strain rate tensor will demonstrate this, in resolving the dominance of the magnetic field in MHD turbulence over the vortex stretching mechanism.

C. MHD DIT Results/Analysis

1. Simulation Parameters

The simulations consist of an initial random isotropic incompressible fluctuating velocity field $\left(u^{'}\right)$, along with an initial random isotropic solendoidal fluctuating magnetic field $(B^{'})$, and a uniform mean magnetic field $\langle B \rangle$. The computational domain is 128^3, and periodic boundary conditions are applied. The key simulation parameters, that are varied, are the initial $B^{'}$, $\langle B \rangle$, kinematic viscosity (ν), and magnetic diffusivity (σ). Cases consist of using an initial random $B^{'}$ and varying strengths of $\langle B \rangle$ applied to the flow at values of .001 and .0025 T. The interaction parameter of these mean magnetic field strengths, are .05 and .3. The viscosity and magnetic diffusivity are .0075, giving a Taylor Reynolds and magnetic Reynolds number of 45.

For these test cases, the MHD Reynolds stress equation can be simplified by the homogeneous condition into two forms where a mean magnetic field is and isn't present.

$$\frac{D}{Dt}\left\langle u_i^{'}u_j^{'}\right\rangle = \mathrm{P}_{ij} + \Pi_{ij} - \varepsilon_{ij} \tag{6.25}$$

$$\Pi_{ij} = \left\langle \frac{p^{'}}{\rho}\left(\frac{\partial u_i^{'}}{\partial x_j} + \frac{\partial u_j^{'}}{\partial x_i}\right)\right\rangle - \left\langle \frac{B_k^{'}}{\mu_0 \rho}\left(\frac{\partial u_j^{'}}{\partial x_k}B_i^{'} + \frac{\partial u_i^{'}}{\partial x_k}B_j^{'}\right)\right\rangle \tag{6.4}$$

$$\varepsilon_{ij} = 2\nu\left\langle \frac{\partial u_i^{'}}{\partial x_j}\frac{\partial u_j^{'}}{\partial x_i}\right\rangle \tag{6.5}$$

1.) Zero Mean Magnetic Field

$$\mathrm{P}_{ij} = 0 \tag{6.26}$$

2.) Uniform Mean Magnetic Field

$$\mathrm{P}_{ij} = \frac{1}{\mu_0 \rho}\left\langle u_j^{'} \frac{\partial B_i^{'}}{\partial x_k} + u_i^{'} \frac{\partial B_j^{'}}{\partial x_k} \right\rangle \langle B_k \rangle \tag{6.27}$$

The difference between the two major cases is that one has no production and the other does, which corresponds to the anisotropizing trends observed when a uniform mean magnetic field is present. The results will include plots of the following: (i) kinetic energy (5.29), (ii) magnetic energy (5.30), (iii) kinetic enstrophy (5.31), (iv) magnetic enstrophy (5.32), (v) Lorentz force work, (vi) enstrophy PDF (6.21), (vii) velocity-strain rate eigenvalues (α, β, γ), and (viii) vorticity alignment with velocity-strain rate eigenvalues.

The computation for the Lorentz force work is as follows.

$$E_{LF} = \frac{1}{L^3} \int \mathbf{v} \cdot (\mathbf{j} \times \mathbf{B}) dx \tag{6.28}$$

2. Results on Magnetic-kinetic Energy Interaction

Figure 33 describes the kinetic/magnetic energy and enstrophy decays. These decays are further described by the Lorentz force energy decay shown in figure 34. Together, these figures depict the nature in which both magnetic and kinetic energy interacts.

a. Random Fluctuating Magnetic Field

For both the case without a magnetic field and with only an initial random fluctuating magnetic field, the kinetic energy and enstrophy decay in a smooth regular manner. The magnetic field fluctuations cause the kinetic energy to decay faster because the magnetic energy is taking away energy from the kinetic mode. This process is seen in figure 33, through the Lorentz force energy decay. Looking at the plots for the initial random fluctuating magnetic field in figure 33, at early times, the kinetic energy decays sharply when the Lorentz force energy is also at negative values. The magnetic energy has a corresponding affect as it has a very slight decay initially. Then at 0.4 eddy turnover times, the magnetic energy starts decaying much faster and the kinetic energy decays at a slower rate. These trends correspond to the positive Lorentz force energy value. This trend continues until all terms reach zero.

The magnetic-kinetic energy interaction can also be seen through the enstrophy decay plots in figure 33. The kinetic enstrophy increases initially and then decays. This initial increase in the vortex stretching is due to the magnetic field generation of vortex structures in the system. This generation of vortex structures is caused by the increase in current density stretching taking place, which is described by the magnetic enstrophy. The evolution equation kinetic enstrophy, shows that current density stretching creates new structures aside from the vortex stretching mechanism. By increasing the peak value of the enstrophy, the magnetic field fluctuations are effectively increasing the amount of length scales for which turbulent kinetic energy is transferred to. This also means that the forward cascading is increasing. At 0.4 eddy turnover times, the kinetic and magnetic enstrophies both reach their peak value. The decay of both enstrophies increase rapidly

at this time, and then the decay of kinetic and magnetic energy reverse trends. The kinetic energy decays at a slower rate, while the magnetic energy decays at a greater rate.

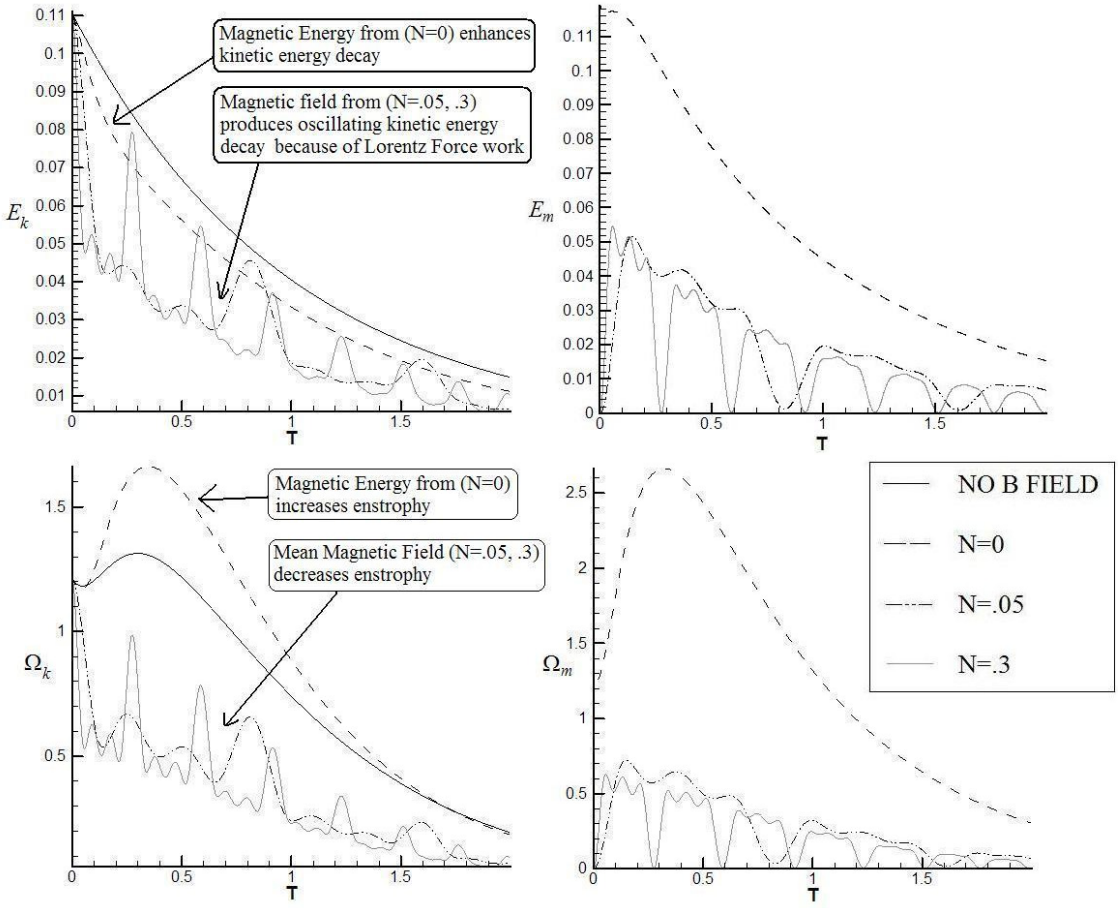

Figure 33. Kinetic/Magnetic Energy and Enstrophy Decay

b. Uniform Mean Magnetic Field

Figure 33 and 34 show that the nature of the kinetic/magnetic energy and enstrophy decays change when a uniform mean magnetic field is applied to incompressible decaying isotropic

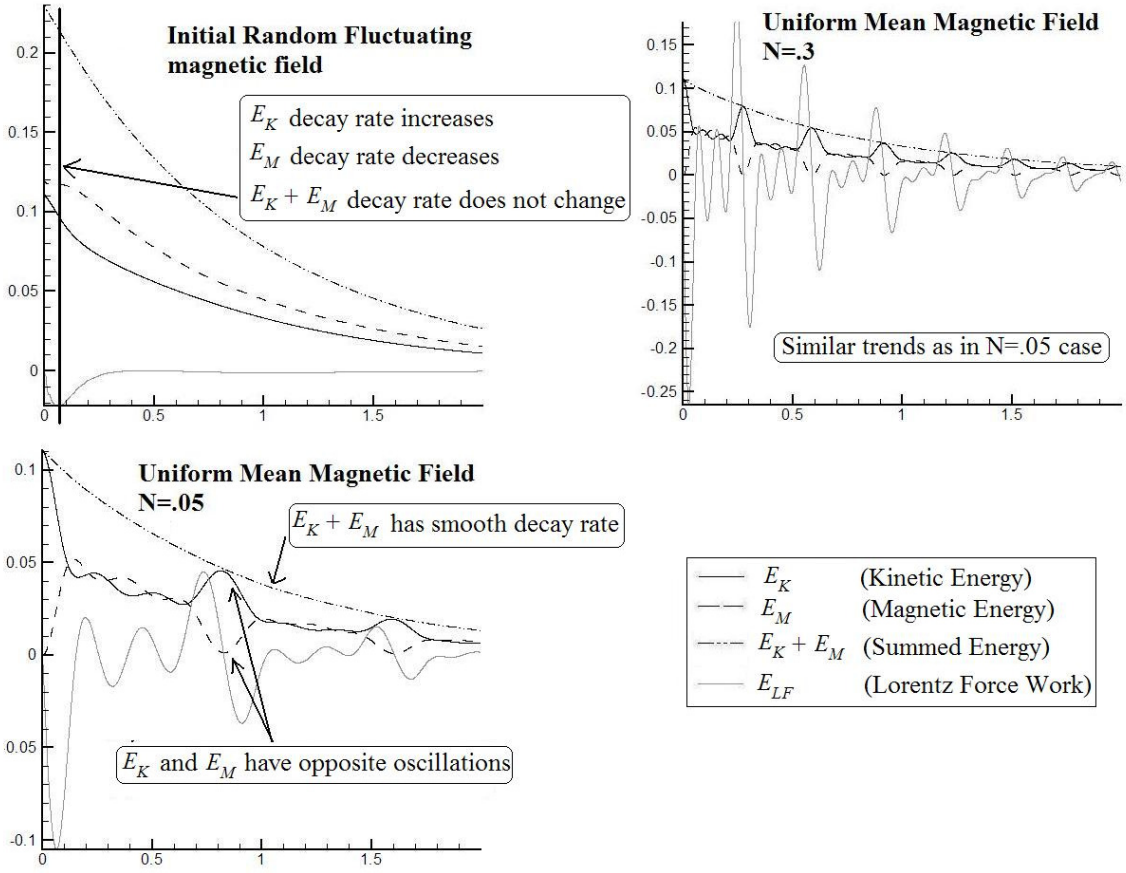

Figure 34. Lorentz Force Work Comparison to Kinetic, Magnetic, and Total Energy

homogeneous turbulence. The turbulent kinetic energy decays faster and oscillates, while the turbulent magnetic field decays at a slower rate and also oscillates. The kinetic energy decays quicker due to the increased damping of velocity fluctuations by the uniform mean magnetic field. With a strong magnetic field applied, the Lorentz force energy increases, causing greater amounts of energy to be absorbed by the magnetic energy mode. This Lorentz force energy also accounts for the oscillations in the energy exchange between the kinetic and magnetic modes. Figure 34 depicts this exchange. It is also notable that the total energy does not oscillate for any of the cases. This trend occurs because the Lorentz force energy terms of the kinetic and magnetic energies cancel each other out, which can be seen in the energy equations. The uniform mean magnetic field acts as a constant elastic magnetic flux band applied to the fluctuating velocity field. Because of the initially isotropic nature of the fluctuating velocity field, the directionality

of the velocity will rapidly vary without any direction being preferred. This leads to the oscillations in the direction of the Lorentz force, causing the oscillating changes in decay of kinetic and magnetic energy. Over time, the amplitude and frequency of the oscillations will decrease. This trend of the oscillations is caused by kinetic energy decay and velocity adjustment to the direction of the mean magnetic field influence. The case of $N = .3$ versus $N = .05$, shows that an increase in the interaction parameter increases the amplitude and frequency of oscillations in the energy decay trends. The increase in magnetic field causes the reactionary Lorentz force to be stronger and quicker in response to the fluctuating velocity field's deformation effect on the magnetic field lines. Comparatively, this physical effect can be compared to a rubber bands resistance to deformation. The stiffer the rubber band (stronger magnetic field), the quicker it opposes deformation and with greater reactionary force.

The kinetic and magnetic enstrophies also decay faster and oscillate with a uniform mean magnetic field applied. Both vortex and current density stretching are inhibited. This trend indicates that the production mechanism created by the mean magnetic field will reduce the amount of length scales for which turbulent kinetic energy is transferred. The forward cascading of turbulence is inhibited.

3. Results of the PDF of Enstrophy Evolution

The total time rate of change of enstrophy describes not only vortex stretching, but the anisotropic tendency of the turbulent flow field. An anisotropic turbulent flow field also indicates the occurrence of inverse energy cascade. Figure 35 contains PDF's of the normalized evolution of enstrophy. The distribution of these PDF's, describe the type of vortex stretching. Figure 36, isolates the physical terms of the normalized evolution of enstrophy. There are three total terms: (i) vortex stretching, (ii) current density stretching, and (iii) magnetic field stretching.

a. Random Fluctuating Magnetic Field

Without any magnetic field applied, the total amount of vortex stretching increases with time. When an initial random fluctuating magnetic field is applied, the vortex stretching increases at a greater rate than without any magnetic field applied. This conclusion is hard to see from figure 35. If figure 35 is looked at closely, it can be seen that the area of under the PDF for the fluctuating magnetic field has a greater positive value than does the normal case without a magnetic field. This result corresponds properly with the increased enstrophy generation shown in figure 33.

Figure 36 shows that with the random fluctuating magnetic field applied, the current density stretching term is marginally dominant over the vortex and magnetic field stretching terms. The current density stretching mechanism weakly favors a positive growth of the enstrophy (straining of vorticity). This characteristic leads to the slightly enhanced direct cascading of kinetic energy.

b. Uniform Mean Magnetic Field

The uniform mean magnetic field has the opposite effect on the enstrophy PDF. Figure 35 shows the PDF shift towards being nearly zero for the case of $N = .05$. This impact of the uniform magnetic field is very significant, as it drives the time evolution of enstrophy towards conservation. This trend depicts the anisotropizing effect the uniform mean magnetic field has. Then for a higher interaction parameter of $N = .3$, the PDF shows a dominant negative trend. This result indicates an greater anistropizing effect of the mean magnetic field. The vorticity is no longer stretching but is actually compressing. The reason for these effects are shown in figure 36, as the current density stretching term is highly dominant in the enstrophy evolution equation. When $N = .05$, there isn't a significant tendency towards negative or positive current density stretching in this plot, corresponding to the conserved state. When $N = .3$, the current density stretching becomes more dominant than for the $N = .05$ case and favors compression (negative stretching) of current density. This trend of compressing the vorticity leads to the inverse cascading of the energy. Larger vortex structures are created from the smaller ones.

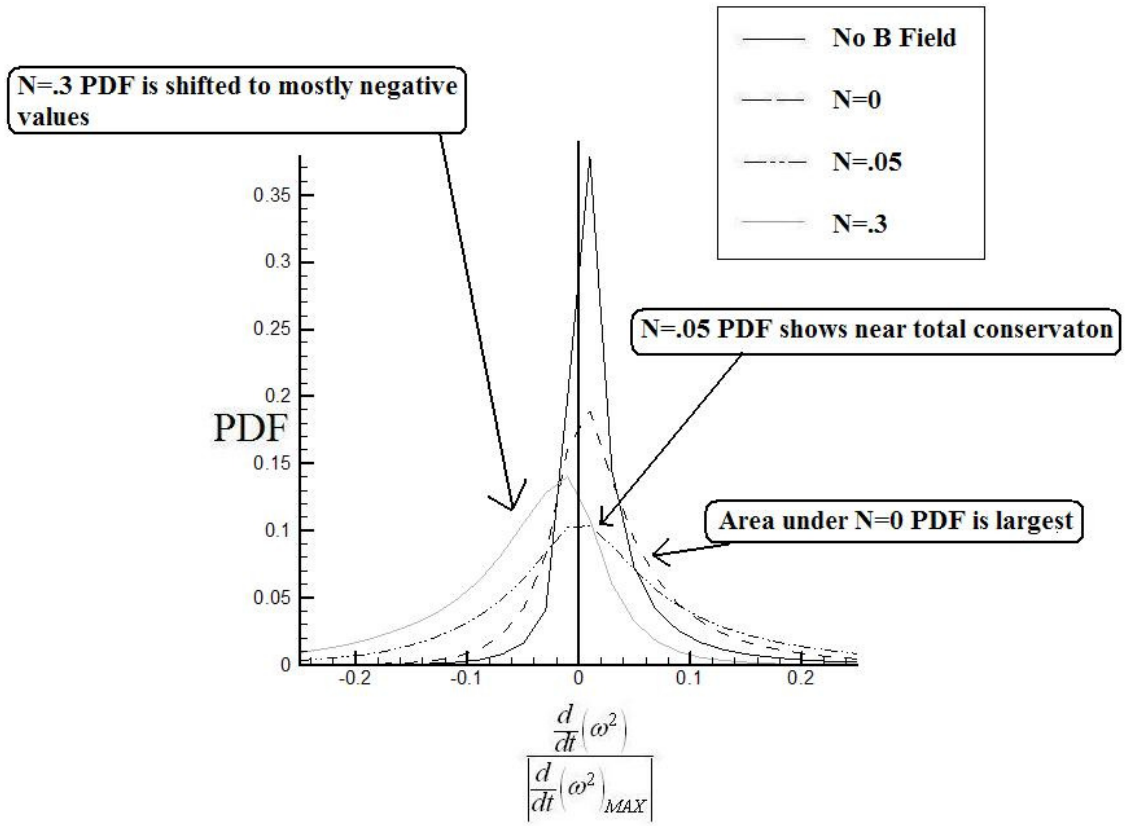

Figure 35. PDF of the Evolution of Enstrophy at Two Eddy Turnover Times

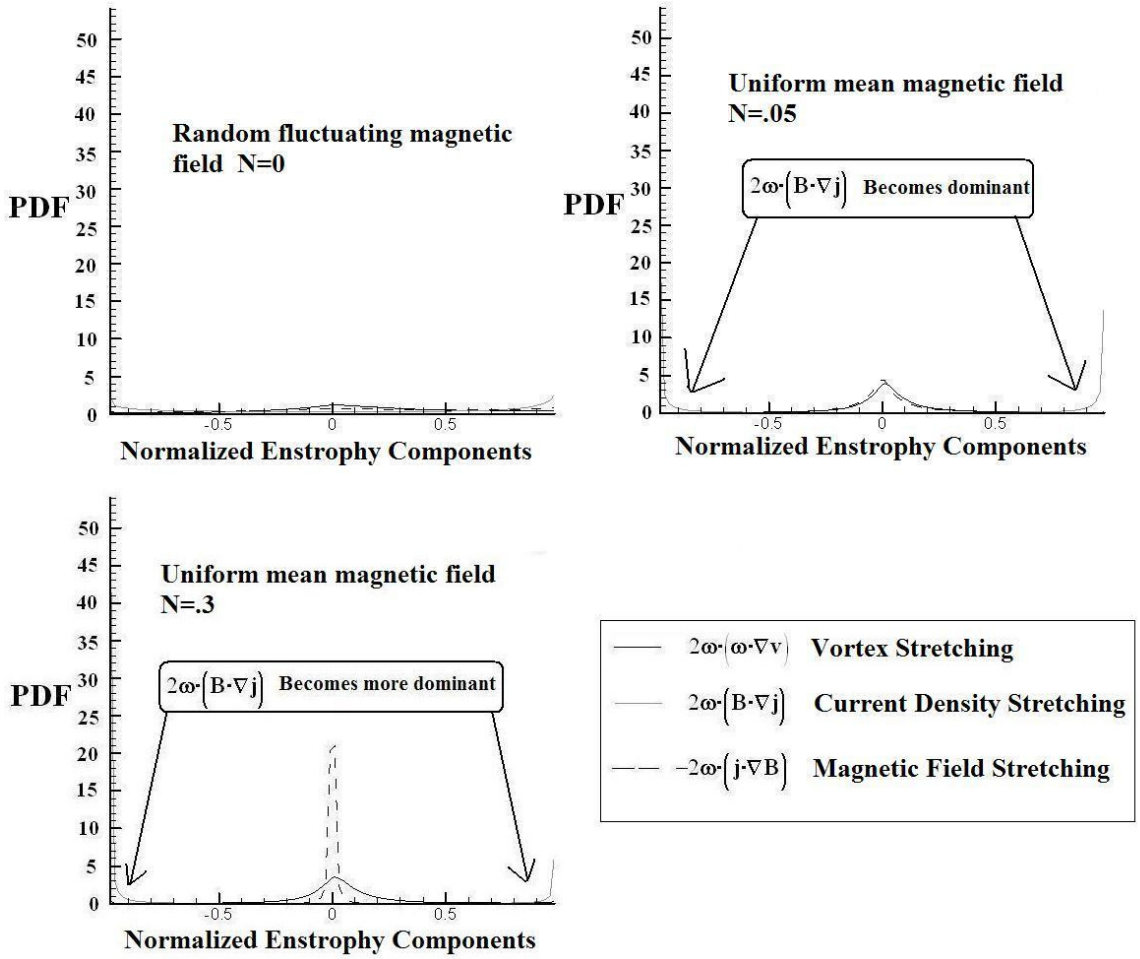

Figure 36. PDF of the Different Components of the Evolution of Enstrophy at Two Eddy Turnover Times

4. Results of Vorticity Alignment to the Strain Rate Tensor

The vorticity alignment to the eigenvalues of the strain rate tensor provides some insight into the direction of energy cascade in hydrodynamic turbulence. In MHD turbulence, however, the vorticity alignment is not related to the direction of energy cascade. The reason is due to the extra source terms related to current density and magnetic field stretching. As shown in figure 36, the current density stretching term is dominant in all MHD turbulence cases presented in this study. Plots of the PDF for the eigenvalues of the velocity strain rate tensor and vorticity alignment to these eigenvalues

are shown in figures 37 and 38. By comparing these figures to the PDF plot in figure 35, it is reaffirmed that the vortex stretching mechanism is not dominant in the enstrophy evolution. This result helps to reveal the importance behind the magnetic field vortex generation terms in MHD turbulence.

a. Random Fluctuating Magnetic Field

With a random fluctuating magnetic field, the PDF trends reverse as compared to the turbulence state without a magnetic field influence. The values of α increase; β decreases, and the value of γ decreases. The alignment of vorticity to α decreases, to β increases, and to γ increases. In hydrodynamic turbulence, these types of trends indicate a change in direction of the inverse cascade. The PDF plots of the enstrophy evolution do not correspond with that trend, as the direct cascading of energy is increased. This indicates that the vortex stretching is not properly characterizing the energy cascade.

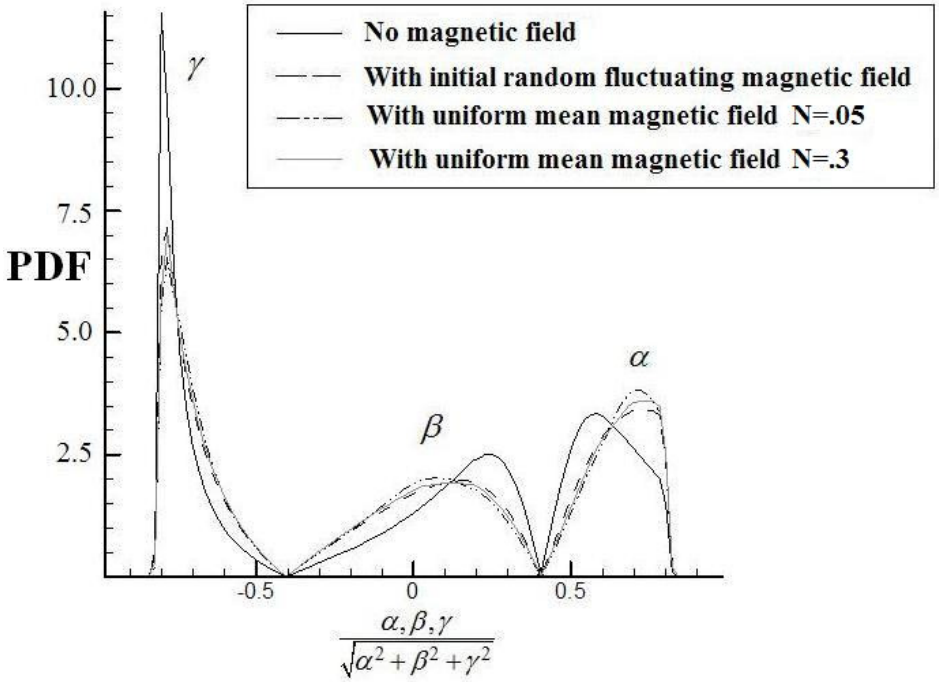

Figure 37. PDF of Eigenvalues of the Velocity Strain Rate Tensor at Two Eddy Turnover Times

b. Uniform Mean Magnetic Field

When a uniform mean magnetic field at an interaction parameter of $N = .05$ is applied, the same trends exhibited for the random fluctuating magnetic field continue to a greater degree. For this case, the vorticity alignment to the eigenvalues of the strain rate tensor, along with the changing values of the eigenvalues, do show some proper characterization of the cascade direction. However, these results don't clearly indicate the approximately conserved state of the enstrophy evolution equation. At a nearly conserved state, inverse cascading should almost be prevalent, and this is not shown by figures 37 and 38. When $N = .3$, the trends in figures 37 and 38 reverse in comparison to those for $N = .05$. The values of α decrease; β increases, and the value of γ increase. The alignment of vorticity to α increase, to β increases, and to γ decreases. This trend in hydrodynamic turbulence would indicate an enhancement of direct cascade between when the interaction parameter increases. Figure 35 of the enstrophy evolution, shows that inverse cascading and anisotropic turbulence is taking dominance in the flow field to an even greater extent than when $N = .05$. Figure 36, also shows that the current density stretching term has greater relative dominance in the enstrophy evolution with the higher interaction parameter. Therefore, it is evident that as the interaction parameter increases, the current stretching mechanism becomes stronger, making the vortex stretching mechanism less characteristic of the cascade property. In the case where $N = .3$,

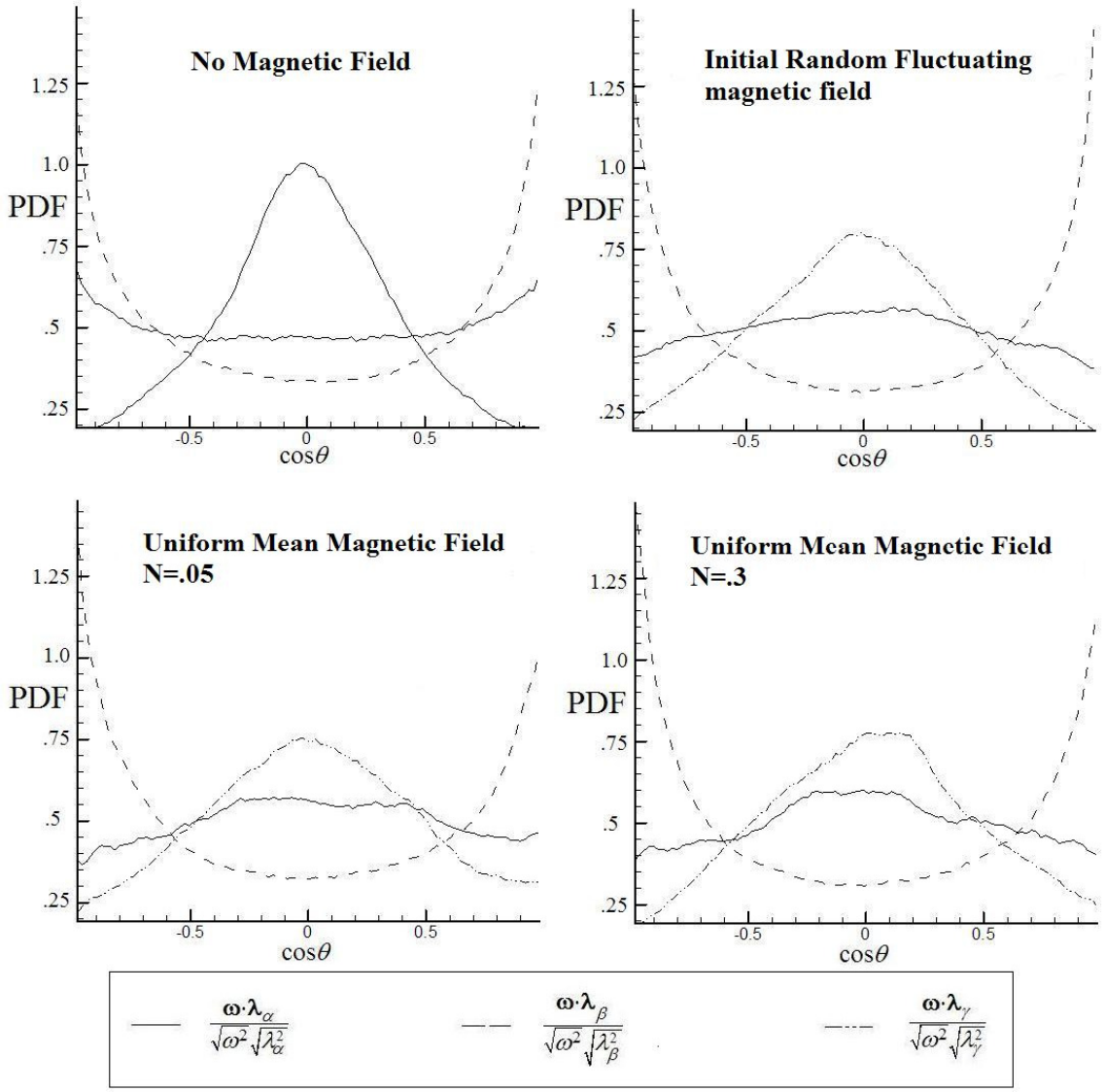

Figure 38. PDF of the Vorticity Alignment to the Eigvenvalues of the Velocity Strain Rate Tensor at Two Eddy Turnover Times

the vortex stretching mechanism is so heavily dominated and insignificant to the enstrophy evolution that it's characteristics no longer correspond to the energy cascade of the MHD turbulent flow.

5. Discussion

The results in figures 33 through 38, clearly show that the magnetic field influence of a uniform mean magnetic field with interaction parameters of $N = .05$ and .3, dominate the vorticity dynamics and energy exchange characteristics. Because these interaction parameters are small, they do not induce very strong anisotropic turbulence, however, they do strongly affect the vortex structures and cause anisotropic tendencies to take place. These trends relate accurately to the MHD Reynolds stress equation. The uniform mean magnetic field creates production terms $\mathrm{P}_{ij} = \frac{1}{\mu_0 \rho}\left\langle u_j^{'} \frac{\partial B_i^{'}}{\partial x_k} + u_i^{'} \frac{\partial B_j^{'}}{\partial x_k} \right\rangle \langle B_k \rangle$ that drive the flow towards anisotropy and inverse cascading.

With a random fluctuating magnetic field, the Lorentz force presence marginally dominates. It drives the turbulent flow field towards stronger turbulent tendencies, indicated by the stronger forward cascade result. This result also correlates with the pressure rate strain term's, $\Pi_{ij} = \left\langle \frac{p^{'}}{\rho}\left(\frac{\partial u_i^{'}}{\partial x_j} + \frac{\partial u_j^{'}}{\partial x_i} \right) \right\rangle - \left\langle \frac{B_k^{'}}{\mu_0 \rho}\left(\frac{\partial u_j^{'}}{\partial x_k} B_i^{'} + \frac{\partial u_i^{'}}{\partial x_k} B_j^{'} \right) \right\rangle$, tendency to increase isotropic tendencies in the flow field. Turbulent flow fields by their nature, increase kinetic energy interaction to all directions.

The energy exchange between the kinetic and magnetic modes depicts how the magnetic field can alter the homogeneous turbulence state. With a random fluctuating magnetic field, the magnetic field absorbs kinetic energy by increasing the amount of vortex eddies in the flow. A strong mean magnetic field will oscillate between absorbing and providing energy to the kinetic mode, which corresponds to trends of MHD turbulence simulations produced by [45-51].

D. Conclusion

Through the analysis of the kinetic/magnetic energy and enstrophy decays, evolution of the enstrophy, and vorticity alignment to the velocity strain rate tensor, the anisotropic effects and cascading mechanisms in decaying isotropic homogeneous turbulence using MHD-LBM can be properly investigated.

The random fluctuating magnetic field enhances forward cascading and increases kinetic energy decay. A random fluctuating magnetic field contributes to the turbulent nature of the flow and increases isotropy in a similar manner as a random fluctuating velocity field.

The uniform mean magnetic field increases kinetic and decreases magnetic energy decay, along with inducing inverse cascading. The Lorentz force energy is captured as the physical mechanism behind the oscillating energy decay trends. These trends are physically caused by the stiff elastic nature of the strong uniform mean magnetic field that creates reactionary forces to the fluctuating velocity field. The current density stretching mechanism dominates the vortex stretching in the vorticity and enstrophy evolution. This current density stretching term compresses the vortex structures leading to anisotropy and inverse cascading.

The MHD Reynolds stress description effectively describes and correlates to the results of the simulations where the mean production terms drive anisotropic flow and fluctuating terms drive isotropy. From past research, it is well-known that mean magnetic fields increase the two-dimensional nature of turbulence. This paper effectively characterizes this nature of turbulence along with inverse cascading by using MHD-LBM and the enstrophy description of the periodic turbulent field.

CHAPTER VII

MAGNETIC FIELD EFFECTS ON AXIS-SWITCHING AND INSTABILITIES IN RECTANGULAR PLASMA JETS

A. Introduction

Rectangular jet (RJ) flow simulations using LBM have been successfully demonstrated by [23 and 24]. In [23], LES-LBM simulations of rectangular jets demonstrated axis-switching and was compared to experimental data [57-63]. In [24], LBM simulations at Reynolds number 150 produced axis-switching. With axis-switching demonstrated by LBM, MHD-LBM is applied to the same problem with an external magnetic field used to influence the RJ flow evolution.

Rectangular jet flow studies have become of great interest due to their unstable natures. Because RJ's are not axis-symmetric, the jet inflow geometry leads to the generation of secondary flows that make the flow field less stable. These secondary flows cause the velocity shear layer growth of the minor axis to exceed that for the major axis. Axis-switching is a result from this instability effect on the shear layer growths. Eventually the RJ becomes unsteady. For low Reynolds number incompressible RJ's, the primary mode of instability is the velocity shear, corresponding to the Kelvin-Helmholtz instability mode. Extensive research in this area has been performed by Grinstein and Gutmark[57-61], Quinn[62], and Tsuchiya [63]. All have studied the axis-switching, entrainment, and turbulence of RJ's. Rectangular jets have been found to improve combustion, reduce jet noise radiation, and reduce infrared plume signature. The inherent instability makes RJ's more susceptible to flow control. For this reason, the flow control effects caused by a strong external magnetic field presence are studied. Results show that a magnetic field presence causes jet flow deceleration, prevents axis-switching, and delays unsteadiness. The details of these results are further illuminated by the magnetic-kinetic energy interaction, the magnetic field influence on the vorticity dynamics, and Lorentz force affect on the Kelvin-Helmholtz instability.

B. Rectangular Jet Characteristics

1. RJ Flow Regimes

Rectangular jet flow is characterized by three major regimes in figure 39: (i) Potential Core (PC), (ii) Characteristic Decay (CD), and (iii) Axis-symmetric Decay (AD).

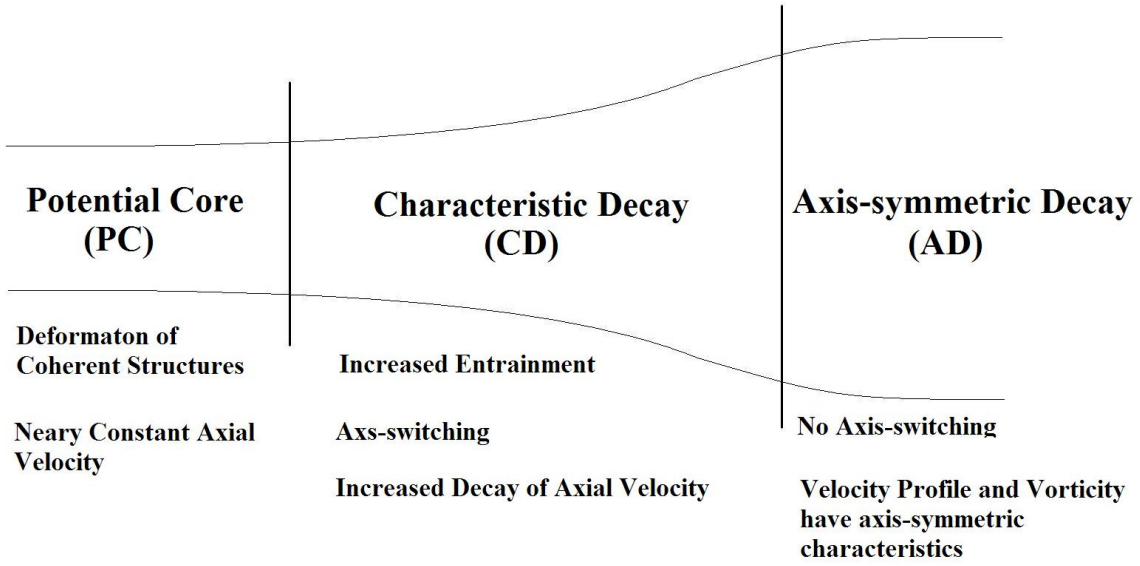

Figure 39. Description of RJ Flow Regimes

The PC regime is nearest the jet exit, and is characterized by little or no axial velocity decay. The jet profile in this regime is similar to that of the exit geometry. The generation of large scale coherent structures outside of the jet also occurs in this regime. In RJ's, the non axis-symmetric geometry generates corner vortices. These vortices deform the coherent structures generated by the RJ. Grinstein and Gutmark [57-61] note in their study of RJ's that the asymmetric vorticity distribution is deformed out of the plane normal to the jet axis, leading to a complex self-induced convective velocity field.

The CD regime is characterized by geometric effects of the RJ flow. The geometric effects, which cause the deformation of the coherent structures in the PC regime, finally have their notable effect on the jet flow. In the CD regime, the axial velocity decays more rapidly, the jet flow profile changes shape, axis-switching occurs, and mixing is increased. The deformation of the vortex structures breaks the axis-symmetric growth of the shear layers with the shear layer of the minor axis growing faster than the shear layer of the major axis. These effects also require a Reynolds number large enough to facilitate the unstable vortex evolution. The value of the Reynolds number depends on the geometry of the jet flow. Krothapalli, Baganoff, and Karamcheti [64] discuss and show that when the aspect ratio increases for RJ's, the axis-switching occurs closer to the jet exit, and mixing increases.

The AD regime begins at the point where the shear layers of both major and minor axes converge on each other. In this regime, the jet profile is axis-symmetric, and the characteristics of vorticity and entrainment are indicative of axis-symmetric flow fields. Axis-switching no longer occurs in this regime.

2. Vortex Dynamics in Axis-Switching

The key physical mechanism causing axis-switching is the deformation of the coherent structures near the jet exit. As previously explained, the deformation is caused by the creation of secondary flows by the corner vortices. This deformation causes the azimuthal and streamwise vortices to interact, redistributing energy between the two flow structures. This can be better understood by comparing the vortex dynamics of an axis-symmetric (circular) jet to the RJ. In circular jets, vortex interaction and merging causes the shear layer growth along with the formation of small-scale structures. In RJ's, the vortex self-induction is more important than the vortex merging process. What this means is that the self-induced vortices are stronger in RJ's and act against the vortices generated by the jet core. In circular jets, the vortices in the jet core are dominant and merge with the self-induced vortices to maintain the axis-symmetric jet structure. The vorticity ($\boldsymbol{\omega}$) evolution equation can describe the physical mechanisms in more detail.

$$\frac{\partial \boldsymbol{\omega}}{\partial t} + \mathbf{v} \cdot \nabla \boldsymbol{\omega} = \boldsymbol{\omega} \cdot \nabla \mathbf{v} + \nu \nabla^2 \boldsymbol{\omega} \tag{6.8}$$

Where $\frac{\partial \boldsymbol{\omega}}{\partial t} + \mathbf{v} \cdot \nabla \boldsymbol{\omega} \Rightarrow \frac{\mathrm{D}\boldsymbol{\omega}}{\mathrm{Dt}}$ is the total rate of change of the vorticity. $\boldsymbol{\omega} \cdot \nabla \mathbf{v}$ is the vortex stretching mechanism, and $\nu \nabla^2 \boldsymbol{\omega}$ is the viscous diffusion of vorticity. $\mathbf{v}$ is the velocity and ν is the viscosity.

The vortex stretching mechanism contains the effects of the self-induced and merging vortex processes. The viscous diffusion of vorticity acts against the instability of the flow. Once the vortex stretching mechanism in RJ's becomes strong enough as compared to the viscous diffusion of vorticity, axis-switching can occur. This corresponds to the onset of axis-switching at higher Reynolds numbers. Figure 40 illustrates the RJ profile in the CD regime with low and high Reynolds numbers, describing how the Reynolds number has a dominant influence on the occurrence of axis-switching. The direction of the secondary flows generated at the corners corresponds with the unequal shear layer growth that causes axis-switching.

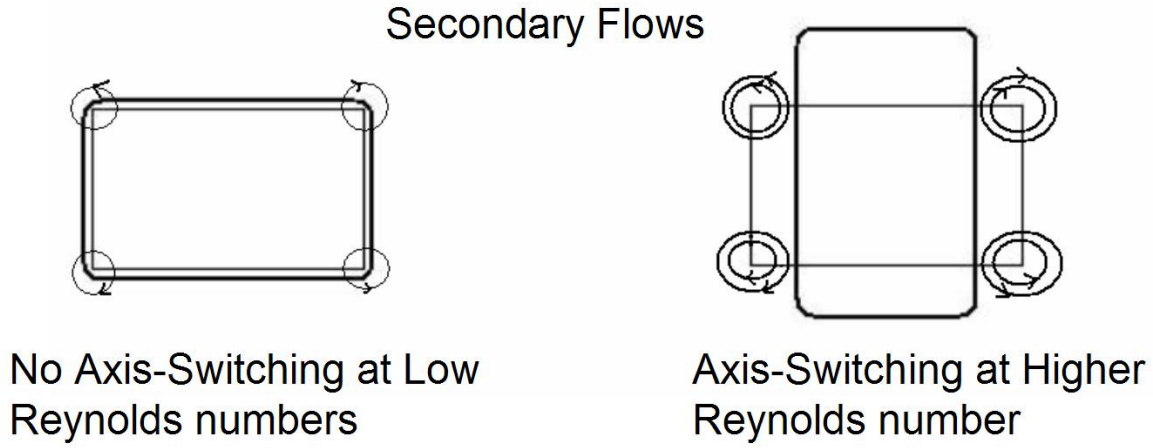

Figure 40. Comparison of Jet Flow Profiles at Low and High Reynolds Numbers

Studies by Grinstein and Gutmark [57-61] show that varying methods can be used to cause axis-switching in jet flows ranging from elongated geometries, nozzles with corners, and axial vorticity generators. All of these methods work because they disturb the axis-symmetric vortex development of the jet. In the same manner, axis-switching has been prevented by using external vortex generating methods. Grinstein and Gutmark [57-61] demonstrate how axis-switching can be prevented by placing tabs on the outer portion of the jet exit. These tabs, depending on their distribution, generate other streamwise vortices that counter those generated by the jet exit corners. It is important to note that this method can be used to both inhibit and induce axis-switching depending on the distribution of the tabs.

3. Kelvin-Helmholtz Instability

In incompressible, low Reynolds number RJ flow, the Kelvin-Helmholtz instability mode is dominant in dictating the stability of the RJ. Kelvin-Helmholtz instability is driven by velocity shear. Taking the non-dimensionalized vorticity equation, the Orr-Sommerfeld equation can be derived to assess the stability properties of the RJ flow.

$$\frac{\partial \bar{\boldsymbol{\omega}}}{\partial t} + \bar{\mathbf{v}} \cdot \nabla \bar{\boldsymbol{\omega}} = \bar{\boldsymbol{\omega}} \cdot \nabla \bar{\mathbf{v}} + \frac{1}{\mathrm{Re}} \nabla^2 \bar{\boldsymbol{\omega}} \quad \text{(non-dimensionalized vorticity equation)} \tag{7.1}$$

$$(c - V)\left(\phi'' - k^2 \phi\right) + V'' \phi = \frac{i}{k\,\mathrm{Re}} \left(\nabla^2\right)^2 \phi \quad \text{(Orr-Sommerfeld equation)} \tag{7.2}$$

The bar symbol is for a mean flow, c is the phase velocity; V is the velocity profile; ϕ is a velocity potential function, and k is the wave vector. The viscosity has a damping effect on the Kelvin-Helmholtz instability, and the Reynolds number can be used to describe the criteria for instability. For Reynolds numbers larger than some critical Reynolds number, which is dependent on the geometry of the flow, the flow field Kelvin-

Helmholtz mode will become unstable. This property is used to determine transition to turbulence at low Reynolds number.

C. MHD Physics

MHD effects on RJ flows are characterized by the magnetic field effect on the vortex structures, the magnetic-kinetic energy interaction, and the magnetic tension exerted on the flow field by the elastic magnetic field lines. Experimental observations in jet casting, show that a strong mean magnetic field presence will decelerate the jet flow. Davidson notes that the "flow spreads laterally along the field lines, evolving from a jet into a sheet" [5]. He further observes that the current is recycled to either side of the jet and "actually accelerates previously stagnant fluid" far downstream. Eventually, a counter-flow can be generated by transverse vortices. Davidson has also performed a theoretical/experimental analysis of vorticity development under uniform magnetic field influences. He finds that uniform magnetic fields can damp vortices, create reverse vortex flow, elongate the structure, and make vortices unstable.

1. Magnetic-kinetic Energy Interaction

The deceleration of jet flows is seen through the exchange between magnetic and kinetic energies by the Lorentz force work. The Lorentz force work term was already described and analyzed in turbulence simulations of the previous chapter.

$$\frac{\partial}{\partial t}\left(\rho\frac{\mathrm{v}^2}{2}\right)=\mathbf{v}\cdot\nabla\left(\rho\frac{\mathrm{v}^2}{2}-p\right)+\mathbf{v}\cdot\left(\mathbf{j}\times\mathbf{B}\right)+\mathbf{v}\cdot\mu\nabla^2\mathrm{v} \tag{6.6}$$

$$\Updownarrow$$

$$\frac{\partial}{\partial t}\left(\frac{\mathrm{B}^2}{2\mu_0}\right)=-\frac{\nabla}{\mu_0}\cdot\left(\mathbf{E}\times\mathbf{B}\right)-\eta\mathrm{j}^2-\mathbf{v}\cdot\left(\mathbf{j}\times\mathbf{B}\right) \tag{6.7}$$

The decay of kinetic energy in MHD homogeneous decaying isotropic turbulence was greatly influenced by the Lorentz force work. Overall, a magnetic field presence increased the kinetic energy decay rate. However, fluctuations in the decay rate did occur. This effect shows that the kinetic energy absorbed energy from the magnetic mode at times, depending on the direction of the Lorentz force. This effect will also be seen in RJ flows. In the core region of the RJ, the flow is decelerated because the magnetic energy mode absorbs kinetic energy. There are other parts of the RJ flow, in which previously stagnant fluid become energetic because the magnetic energy is absorbed by the kinetic mode at those locations.

2. Magnetic Field Influence on Vorticity

The presence of the Lorentz force not only affects the momentum and energy distributions, but it also affects the vortex structures in flow fields. The following equation provides the physical terms involved in the MHD vorticity equation.

$$\frac{\partial \boldsymbol{\omega}}{\partial t} + \mathbf{v} \cdot \nabla \boldsymbol{\omega} = \boldsymbol{\omega} \cdot \nabla \mathbf{v} + \mathbf{B} \cdot \nabla \mathbf{j} - \mathbf{j} \cdot \nabla \mathbf{B} + \nu \nabla^2 \boldsymbol{\omega} \qquad (6.17)$$

This equation includes two new source terms created by current density and magnetic field stretching. These terms can manipulate, damp, and enhance the vortex stretching effect by the velocity field depending on the magnetic field applied.

Davidson [5] gives a comprehensive analysis of uniform magnetic field effects on vortex structures. This analysis does not directly apply to jet flow vortices, but they do have similarities.

Figure 41 provides Davidson's theoretical description [5] of the effect of a strong and weak uniform magnetic field on a vortex aligned parallel with the magnetic field.

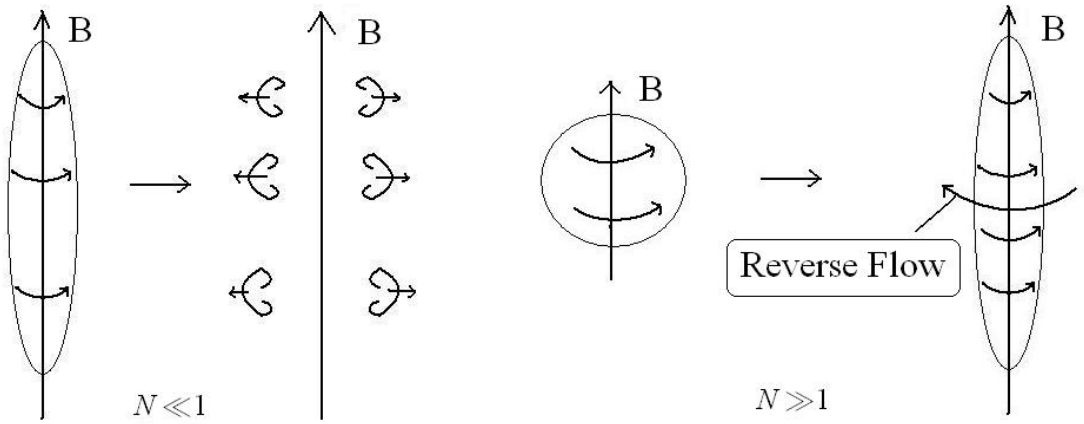

Figure 41. Effect of Strong and Weak Magnetic Fields on Vortcity Aligned Parallel to a Uniform Magnetic Field [5]

In the cases of a weak magnetic field ($N \ll 1$), the vortices are weakened and possibly damped out. In the presence of a strong magnetic field (N>>1), reverse flow is generated around the vortex structures acting against the vortices generated by the vortex stretching mechanism.

Figure 42 illustrates Davidson's description [5] of the effect of a strong and weak mean magnetic field on a vortex aligned transversely with the magnetic field.

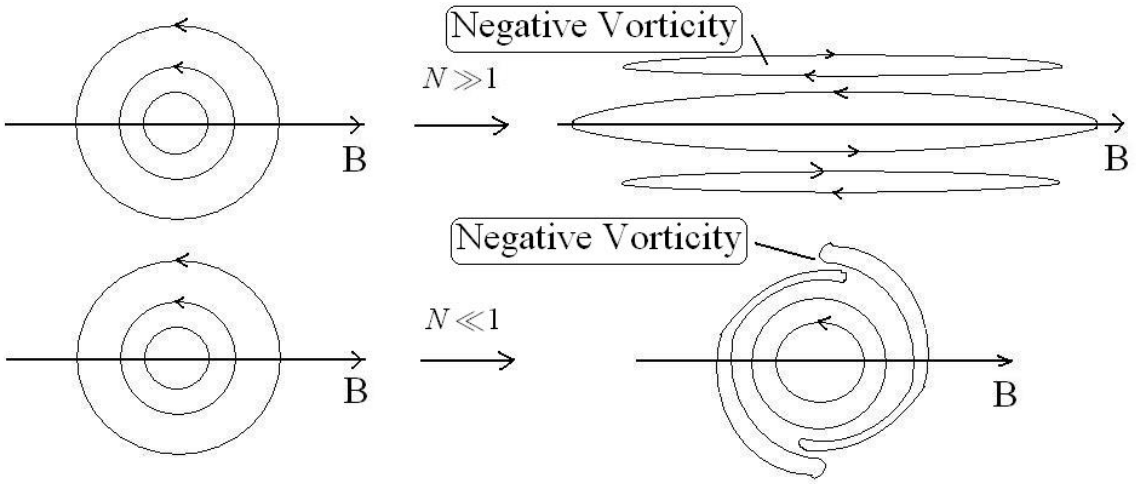

Figure 42. Effect of Strong and Weak Magnetic Fields on Vorticity Aligned Transverse to a Uniform Magnetic Field [5]

In the cases of a weak magnetic field ($N \ll 1$), the vortices are destabilized and weakened. In the presence of a strong magnetic field (N>>1), the vortex structure is elongated in the direction of the applied magnetic field.

Figure 43 provides some experimental observations of the vorticity evolution under the effect of a weak and strong magnetic field aligned both parallel and transversely to the vortex [65].

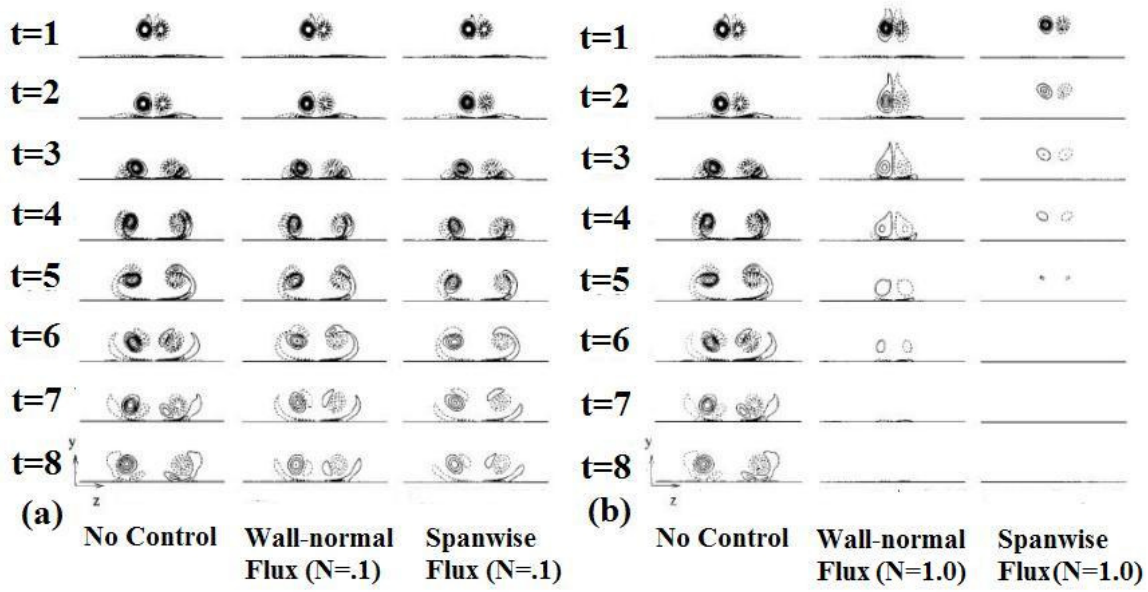

Figure 43. Experimental Observations of Weak and Strong Parallel and Transverse Magnetic Fields on Vorticity [65]

The left hand side observations noted by (a) are for a weak magnetic field influence ($N = .1$), while the right hand side observations noted by (c) are for a strong magnetic field influence ($N = 1$). The columns specified as "No Control" have no magnetic field exerted. The columns specified as "Wall-normal Flux" are for a transversely aligned magnetic field, while the columns specified as "Spanwise Flux" are for a parallel magnetic field.

When $N = .1$, there isn't much effect taking place on the vortex structure. For both transverse and parallel magnetic fields, the vortex structure is weakened. In this case, the magnetic field is not strong enough to damp out the vorticity or change it's alignment. For the case of $N = 1$, the vortex structure is damped out for both transverse and parallel magnetic fields. The parallel magnetic field damps out the vortex immediately, while the transverse magnetic field elongates the structure in the magnetic field direction before it damps out. These experiments provide validation to Davidson's theoretical conclusions, however the reverse vortex structure was not observed for the

case of the strong magnetic field. The reason is likely attributed to the fact that the magnetic field influence is not strong enough to cause such an effect.

This analysis of the magnetic field effect on vorticity is very important in understanding how the magnetic field affects axis-switching. The similarity between these observations to what occurs in MHD RJ flows, explains the magnetic field impact on the secondary flows that generate the instability in RJ's.

3. Magnetic Field Influence on Kelvin-Helmholtz Instability

In section B, the Kelvin-Helmholtz instability mode was explained for incompressible flows. With the addition of the Lorentz force, this mode is no longer dictated by just the Reynolds number.

$$\frac{\partial \bar{\boldsymbol{\omega}}}{\partial t} + \bar{\mathbf{v}} \cdot \nabla \bar{\boldsymbol{\omega}} = \bar{\boldsymbol{\omega}} \cdot \nabla \bar{\mathbf{v}} + \frac{2}{\beta}\left(\bar{\mathbf{B}} \cdot \nabla \bar{\mathbf{j}} - \bar{\mathbf{j}} \cdot \nabla \bar{\mathbf{B}} \right) + \frac{1}{\mathrm{Re}} \nabla^2 \bar{\boldsymbol{\omega}} \tag{7.3}$$

$$(c - V)\left(\phi'' - k^2 \phi\right) + V'' \phi + \frac{2}{\beta}\left(B\left(\psi'' - k^2 \psi\right) - B'' \psi \right) = \frac{i}{k\,\mathrm{Re}} \left(\nabla^2\right)^2 \phi \tag{7.4}$$

$\bar{\mathbf{j}}$ equals $\nabla \times \bar{\mathbf{B}}$, and ψ is the magnetic potential function. The non-dimensionalized magnetic induction equation is also utilized for MHD flow in analyzing stability.

$$\frac{\partial \bar{\mathbf{B}}}{\partial t} + \bar{\mathbf{v}} \cdot \nabla \bar{\mathbf{B}} = \bar{\mathbf{B}} \cdot \nabla \bar{\mathbf{v}} + \frac{1}{Rm} \nabla^2 \bar{\mathbf{B}} \tag{7.5}$$

$$(c - V)\psi + B\phi = \frac{i}{kRm} \left(\nabla^2\right)^2 \psi \tag{7.6}$$

An analysis of these stability equations is performed by Biskamp [52]. Biskamp's analysis is limited to the application of an external uniform magnetic field. For this case,

the magnetic field must be parallel to the flow in order to have an effect on the instability mode. The resultant Lorentz force, of a perpendicular magnetic field, is parallel to the flow and does not affect the transverse motion, which is responsible for the perturbed vortex structures that cause instability.

The stability equations for vorticity and the magnetic field with the dissipation terms neglected are combined.

$$\frac{d}{dx}\left(\left[\left(c-V\right)^2-v_a^2\right]\frac{df}{dx}\right)-k^2\left[\left(c-V\right)^2-v_a^2\right]f=0\,,\quad f=\frac{\beta\psi}{kB} \tag{7.7}$$

$v_a = B\left(x\right)$ (Alfven velocity)

This equation can be integrated to give the following.

$$\left[\left(c-V\right)^2-v_a^2\right]\frac{df}{dx}\Big|_{-\varepsilon}^{\varepsilon} \tag{7.8}$$

The velocity profile can be defined to provide a stability criteria for this equation.

$$V\left(x\right)=\begin{cases}V_1 & x<0\\ V_2 & x>0\end{cases} \tag{7.9}$$

$$\left(c-V_1\right)^2+\left(c-V_2\right)^2-2v_a^2=0 \tag{7.10}$$

$$c=\frac{1}{2}\left(V_1+V_2\right)\pm\sqrt{v_a^2-\frac{1}{4}\left(V_1-V_2\right)^2} \tag{7.11}$$

Therefore, a parallel magnetic field with an Alfven speed of $v_a>\frac{1}{2}\left|V_1-V_2\right|$ stabilizes the Kelvin-Helmholtz mode. The Alfven velocity must be greater than the velocity change across the vortex sheet. This stabilization is due to the magnetic field-line bending that

absorbs energy from the sheared velocity. More energy is absorbed than released in this situation.

Another important characteristic to note in determining the stability criteria for MHD flows under the influence of a parallel magnetic field is the parameter β. Physically, β is the ratio of the kinetic energy to magnetic energy. It is already known that if the Alfven velocity, which corresponds to the value of the parallel magnetic field, is larger than the change in velocity across a vortex sheet, the Kelvin-Helmholtz mode will be stable. Therefore a critical value of β can be defined, depending on the flow geometry, such that if $\beta > \beta_{crit}$ then the Kelvin-Helmholtz mode is stable.

Figure 44 is taken from Biskamp [52], and shows an experimental comparison between an unstable un-magnetized jet on the left hand side to a magnetized jet on the right hand side.

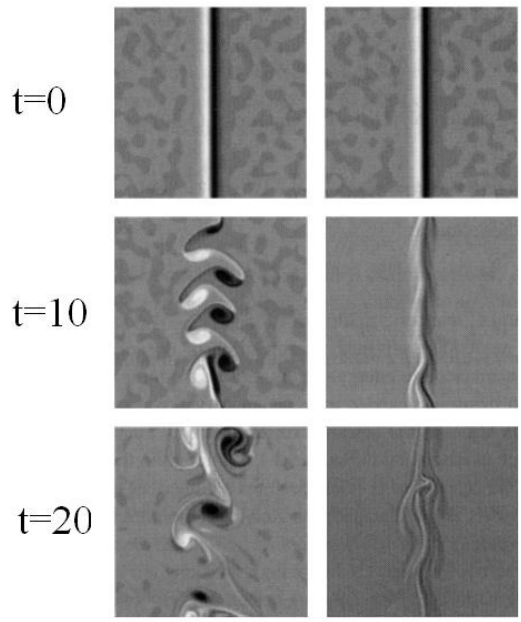

Figure 44. Jet Flow Comparison of Unstable Jet with Magnetically Damped Unstable Jet [52]

A parallel magnetic field is exerted on the jet of the right hand side and damps out the Kelvin-Helmholtz instability. The viscosity and magnetic resistivity, while not being

incorporated in the stability analysis, determines the width of the sheets, however, the dynamics do not change.

The Lorentz force effect on the Kelvin-Helmholtz mode instability is important in understanding how a strong magnetic field prevents unsteady flow, transition, and turbulence. From this stability analysis, it is evident that a strong magnetic field, parallel to the flow, damps the instability by absorbing the kinetic energy of the sheared velocity and transmitting the sheared velocity perturbation as an Alfven wave.

D. Simulation/Results

1. MHD RJ Simulation Parameters

The RJ simulations follow from the simulations performed by Yu and Girimaji [23 and 24] except that MHD physics along with a strong externally applied magnetic field are now included. This means that a rectangular computational domain consisting of a uniform velocity field coming out of a rectangular jet exit area with an externally applied magnetic field is devised. The following are the initial and boundary conditions for the velocity and magnetic field.

a. Velocity Field

- Initial value of zero everywhere except at jet exit
- Constant uniform velocity at jet exit
- Bounceback boundary condition for uniform flow at jet exit

$$f_1 = 6w_1\rho\boldsymbol{e}_1 \cdot \boldsymbol{u} + f_2 \tag{7.12}$$

- Bounceback boundary condition for stationary wall at x=0 plane around jet exit

$$f_1 = f_2 \tag{7.13}$$

- Periodic (at rest) boundary condition for all non-axial boundaries

$$f_1^1 = f_1^{n+1}, \quad f_1^n = f_1^0, \tag{7.14}$$

with planar nodes going from 0 to n+1

- Extrapolation (fully developed) boundary condition at far downstream plane

$$f_1^{n+1} = f_1^n \tag{7.15}$$

Figure 45, provides an illustration of the computational domain in terms of the velocity field boundary conditions.

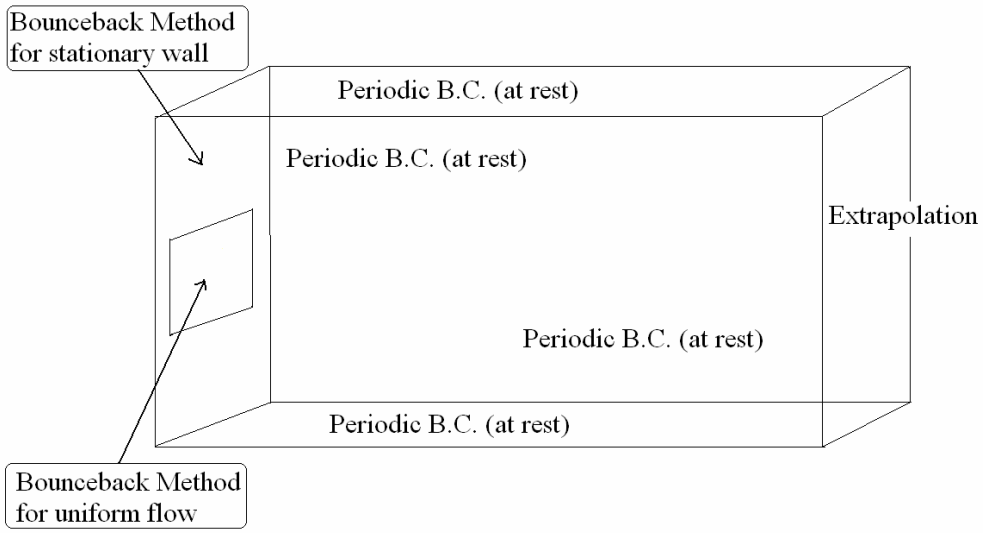

Figure 45. Boundary Conditions for Velocity Field

b. Magnetic Field

- Initial value of zero everywhere

- Conducting boundary condition at jet exit (same as bounceback for uniform flow)
- Insulating Wall boundary condition on the wall at x=0 plane around jet exit

$$f_1 = -f_2 \tag{7.16}$$

- Periodic (at rest) boundary condition for all non-axial boundaries
- Extrapolation (fully developed) boundary condition at far downstream plane
- Constantly applied external magnetic field generated by a circular current loop, calculated by the Biot-Savart Law

$$\mathbf{B} = \frac{\mu_0 I}{4\pi}\int \frac{d\mathbf{l}\times\mathbf{r}}{|\mathbf{r}|^3} = \frac{\mu_0}{4\pi}\int \frac{\mathbf{I}\times\mathbf{r}}{r^2}dl = \frac{\mu_0}{4\pi}\int \frac{\mathbf{j}\times\mathbf{r}}{r^2}d\tau \tag{3.9}$$

- An alternate constantly applied external uniform magnetic field is also applied for some cases

Figure 46, provides an illustration of the computational domain in terms of the magnetic field boundary conditions.

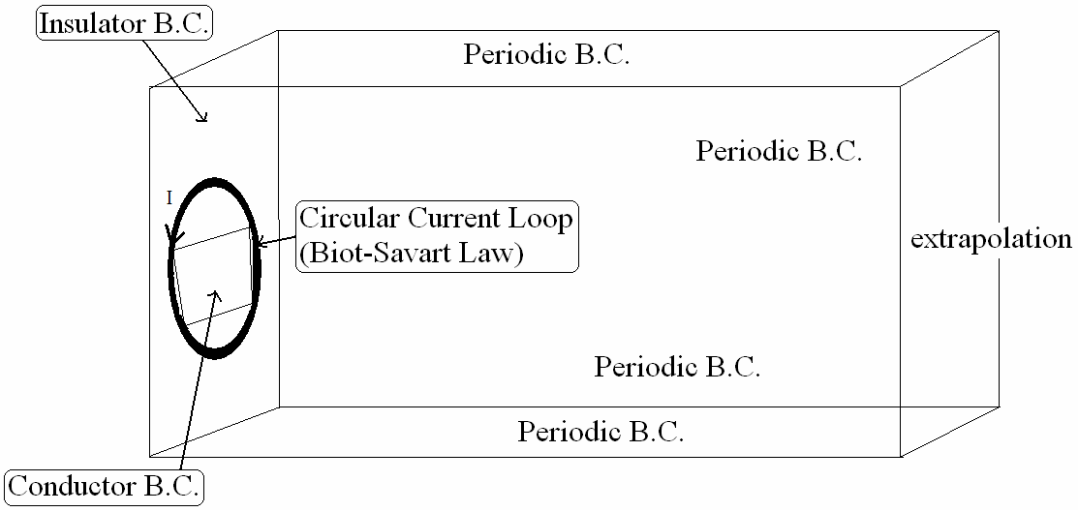

Figure 46. Boundary Conditions for Magnetic Field

Other important computational parameters are as follows.

- Computational Domain size of 160x120x80 for $\mathrm{Re} = 10$
- Computational Domain size of 320x180x160 for $\mathrm{Re} \geq 150$
- Computational dimensions of jet exit are 12x8 for Re=10 and 24x16 for $\mathrm{Re} \geq 150$
- Physical dimensions of jet exit are 1.5 m x 1.0 cm
- Jet flow deceleration is studied at Re=10 with Rm of 1, 5, 20, and 40
- Axis-switching is studied at Re=150 and Rm=5
- Unsteadiness is studied at Re=160, 165, and 170 with Rm=5
- When Re=10, *I* is varied between 0 (no B field), 1.875 A (weak B field) and 5.625 A (strong B field)
- When $\mathrm{Re} \geq 150$, *I* is varied between 0 (no B field), 14.05 A (weakest B field), 21.1 A (weak B field), 24.6 A (strong B field), and 28.13 A (strongest B field)
- Several cases of a strong uniform magnetic field with strengths of .125 T^{-2} are applied in the positive x, y, and z directions.
- $\frac{U_\infty}{c} = .1$ at jet exit, c is the isothermal speed of sound $c = \sqrt{RT}$

- $\nu = .15 \frac{cm^2}{s}$

c. Simulation Case Studies

The simulations are comprised into five major areas of study: (i) RJ Axis-switching and Entrainment trends (ii) Uniform Magnetic Field Influence on Re=150 RJ Flow, (iii) Magnetic damping of Re=10 RJ Flow using a Circular Current Loop, (iv) Circular Current Loop Influence on RJ Vorticity and Axis-Switching, and (v) Circular Current Loop Influence on Unsteadiness. The section provides a physical study that directly relates to experimental and theoretical analysis. The purpose of the first area of study is to compare normal RJ trends at AR=1.5 and Re=150 to experimental RJ trends at AR=1.5 and Re=15800. While this study does not present an exact comparison, it does show that reasonable physical trends related to the unstable nature of RJ's are demonstrated by LBM. The second area of study is to provide some verification to the MHD RJ results of this paper. In the jet flow deceleration study at Re=10, the dependence of the external magnetic field strength generated by a circular current loop and magnetic Reynolds number on the jet plume is described. The study of the influence of a circular current loop on axis-switching and vorticity dynamics is the most important area. Axis-switching was found to occur at Re=150 by Yu and Girimaji [24], therefore, the Reynolds number is set to 150 and the current strengths in the circular current loop are varied as previously specified. In the final area of study, the Reynolds number is varied from 160 to 170 to assess a range in which unsteadiness can be prevented by the magnetic field generated by a circular current loop.

2. Hydrodynamic RJ Axis-switching and Entrainment trends

This section compares results of axis-switching and entrainment for the Re=150 LBM simulations to that of experimental RJ results of AR=1.5 and Re=25900. Before showing MHD-LBM RJ results, this comparison is useful in providing physical

justification for the hydrodynamic physical processes taking place in the LBM RJ simulations.

As previously discussed, axis-switching occurs when the shear layer growth in the minor axis is greater than the shear layer growth of the major axis. The phenomenon of axis-switching is seen in the jet profile. For the case of rectangular jets, the jet profile shifts 90 degrees. Jet flow profiles are plotted in the streamwise plane at various locations from the jet exit plane. The profiles are determined by plotting the half-width velocity profiles. This means that all computational nodes with a velocity greater than or equal to half the maximum velocity of that streamwise plane are included in the jet profile.

Figure 47 shows the RJ flow profiles of an experimental study (AR=1.5, Re=25900) [63], LES-LBM study (AR=1.5, Re=25900) [23], and the current study (AR=1.5, Re=150) at the following distances: .1H, 1.5H, 4H, and 10H from the jet exit (H=height of jet exit). The height dimension (H) of the jet is in the minor axis direction. This figure compares experimental results (A) [63] to numerical results (B) [23] using LES-LBM. This comparison shows that LES-LBM is capable of capturing axis-switching at reasonable accuracy. The numerical results of this thesis (C) show similar trends to parts A and B. It is not known whether these trends are precisely accurate with Re=150, AR=1.5 RJ, due to a lack of experimental data. Comparing the jet profile trend (Re=150) to that of the other results, provides encouraging trends indicating axis-switching.

Figures 48 and 49 compare the half-width velocity profiles of experimental data (AR=1.5, Re=15800) [63] to the study of this thesis (AR=1.5, Re=150). These profiles represent the entrainment (jet spread) of the RJ. From comparing figure 48 to 49, a similar trend is seen between the Re=150 and Re=15800 cases. The trendline for 2Y/H starts off initially greater than 2Z/H (PC region). The trendline for 2Y/H proceeds to decrease, corresponding to the slowed growth rate of the major axis versus the minor axis (CD region). Later on, the 2Y/H trendline increases again (AD region). Numerical data does not have parameters or a distance matching the experimental data. The similar trends in the results of figures 48 and 49, however, show that the LBM RJ Re=150 simulation is demonstrating axis-switching.

The comparisons between the experimental [63] and numerical results of RJ flow in figures 47 through 49, indicate that the axis-switching phenomena is able to be captured by LBM simulations of RJ at Re=150 and AR=1.5. While the accuracy with experimental data isn't known, the proper physical axis-switching phenomenon is taking effect. This physical verification of the axis-switching phenomena provides a basis for further studies of flow control impact on axis-switching.

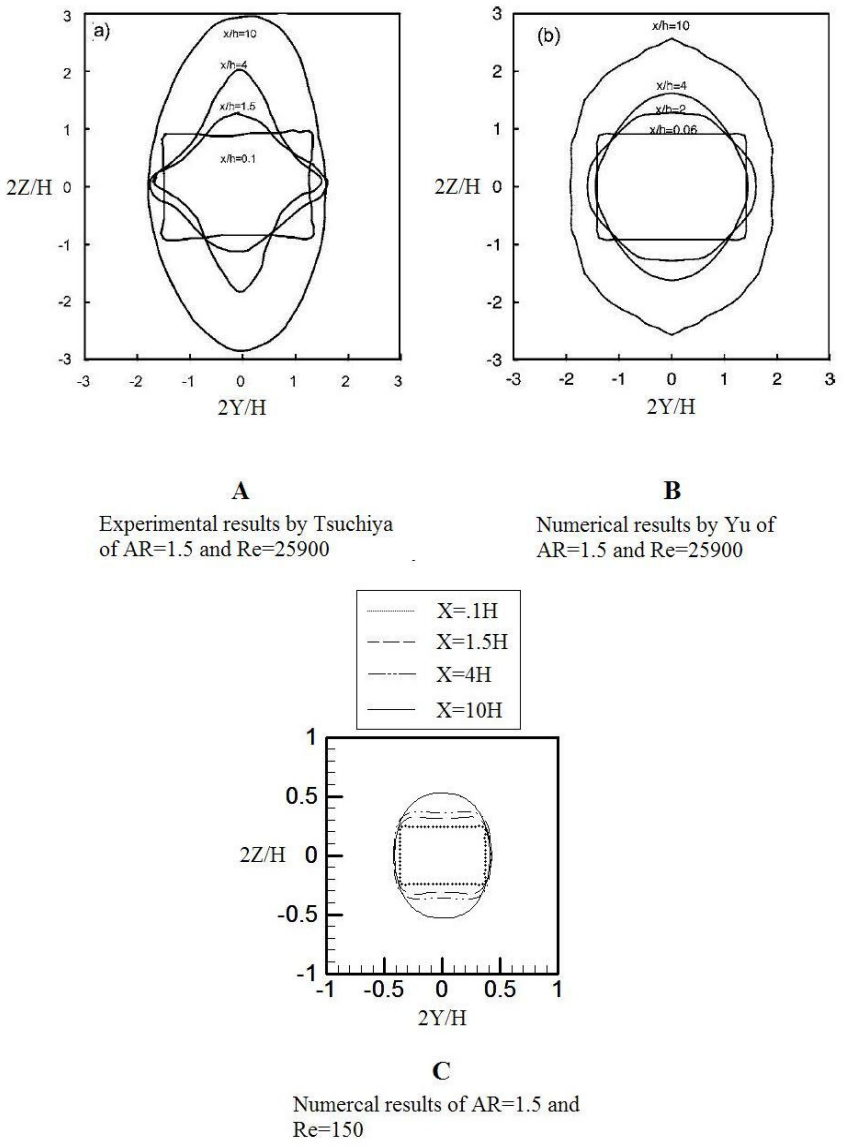

Figure 47. Comparison of Jet Profile Trends [23 and 63]

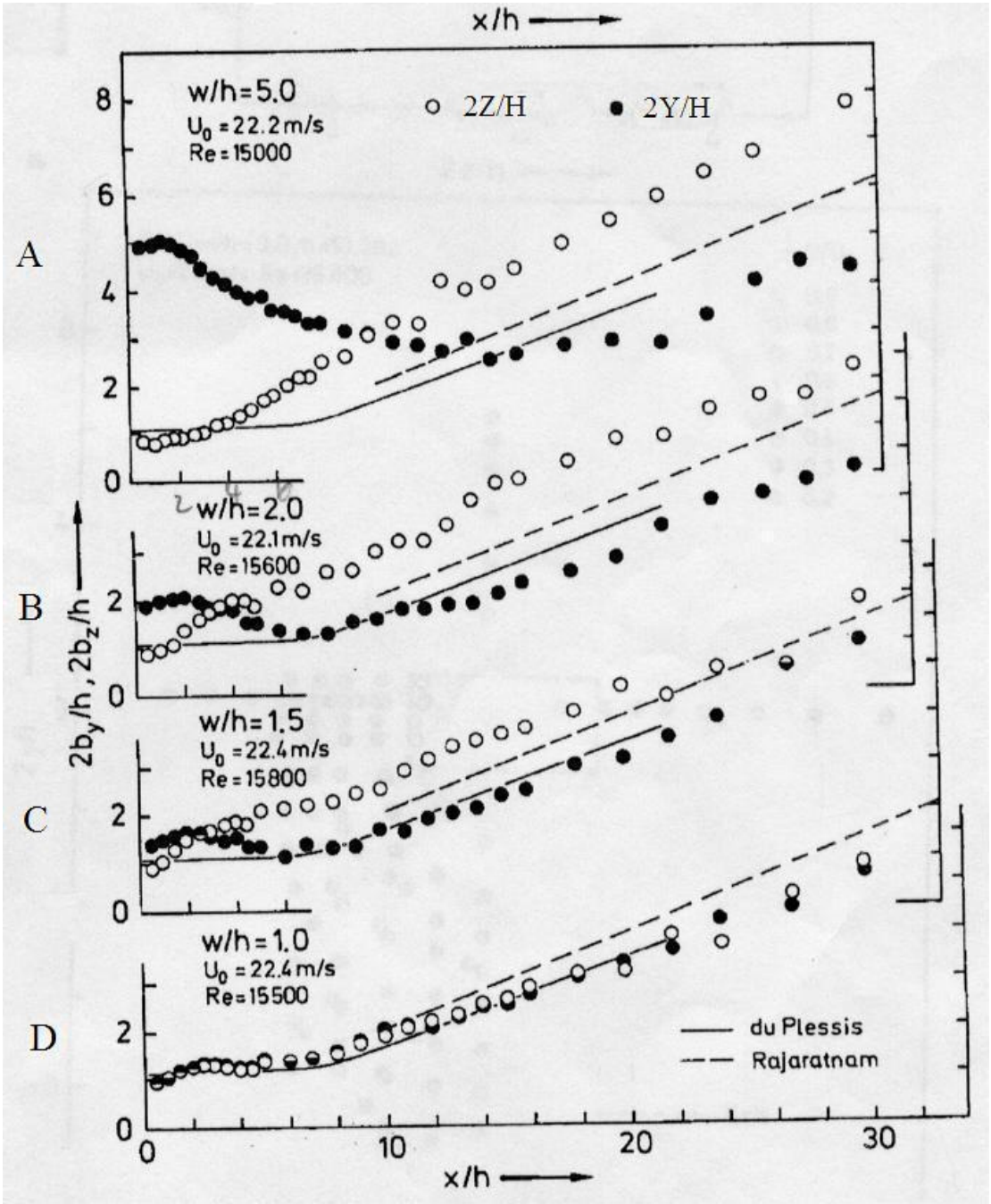

Figure 48. Experimental Results of Velocity Half-Width Profile for RJ at varying Re and AR [63]

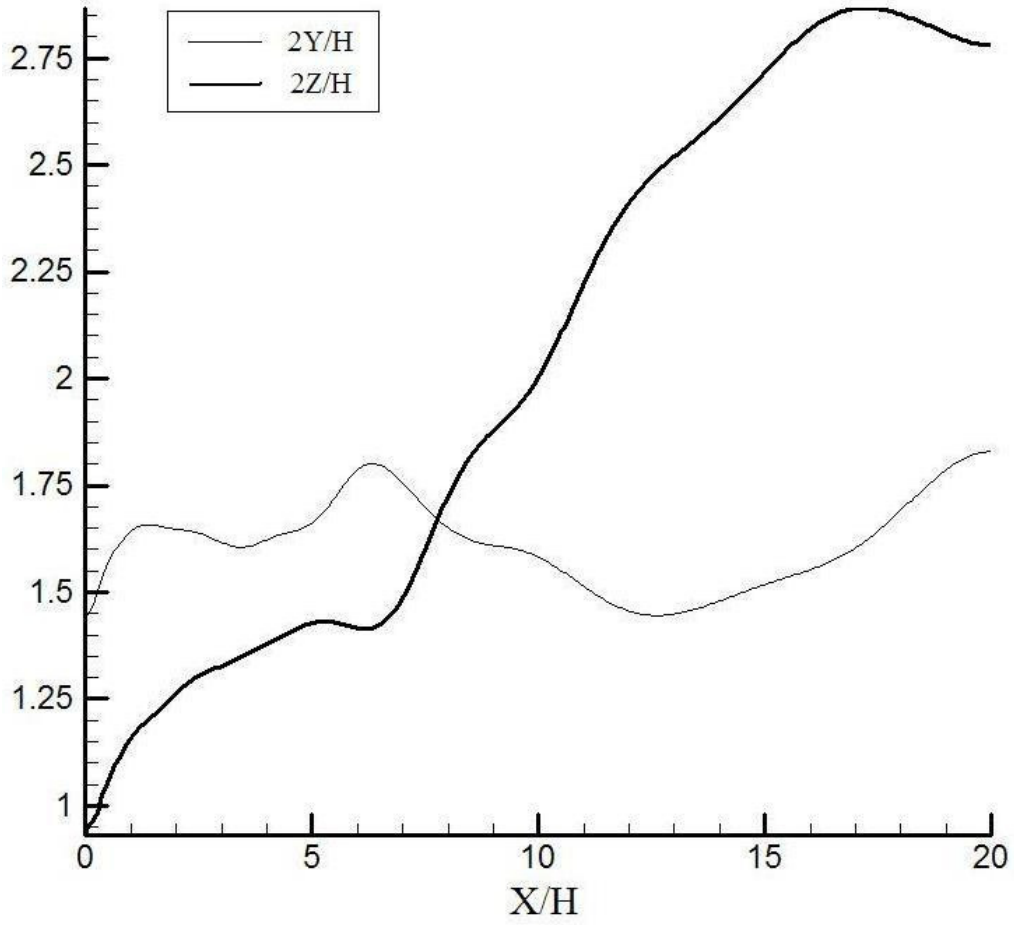

Figure 49. Numerical Result for Half-Width Velocity Profile at AR=1.5 and Re=150

3. Uniform Magnetic Field Influence on Re=150 RJ Flow

This section presents results that provide a good physical study into the effects of a strong uniform magnetic field on RJ vortex and flow field structures. The axial velocity and vorticity are analyzed with a constant magnetic field in the y and z directions. The uniform velocity at the jet exit for these simulations is 22.5 cm/s, and the viscosity is .15 cm^2/s. The uniform magnetic field is .125 T^{-2}. The results of this section have a strong correlation to the theoretical and experimental studies of [5 and 66].

Figure 50 shows the effect on the RJ plume by a constant uniform applied magnetic field.

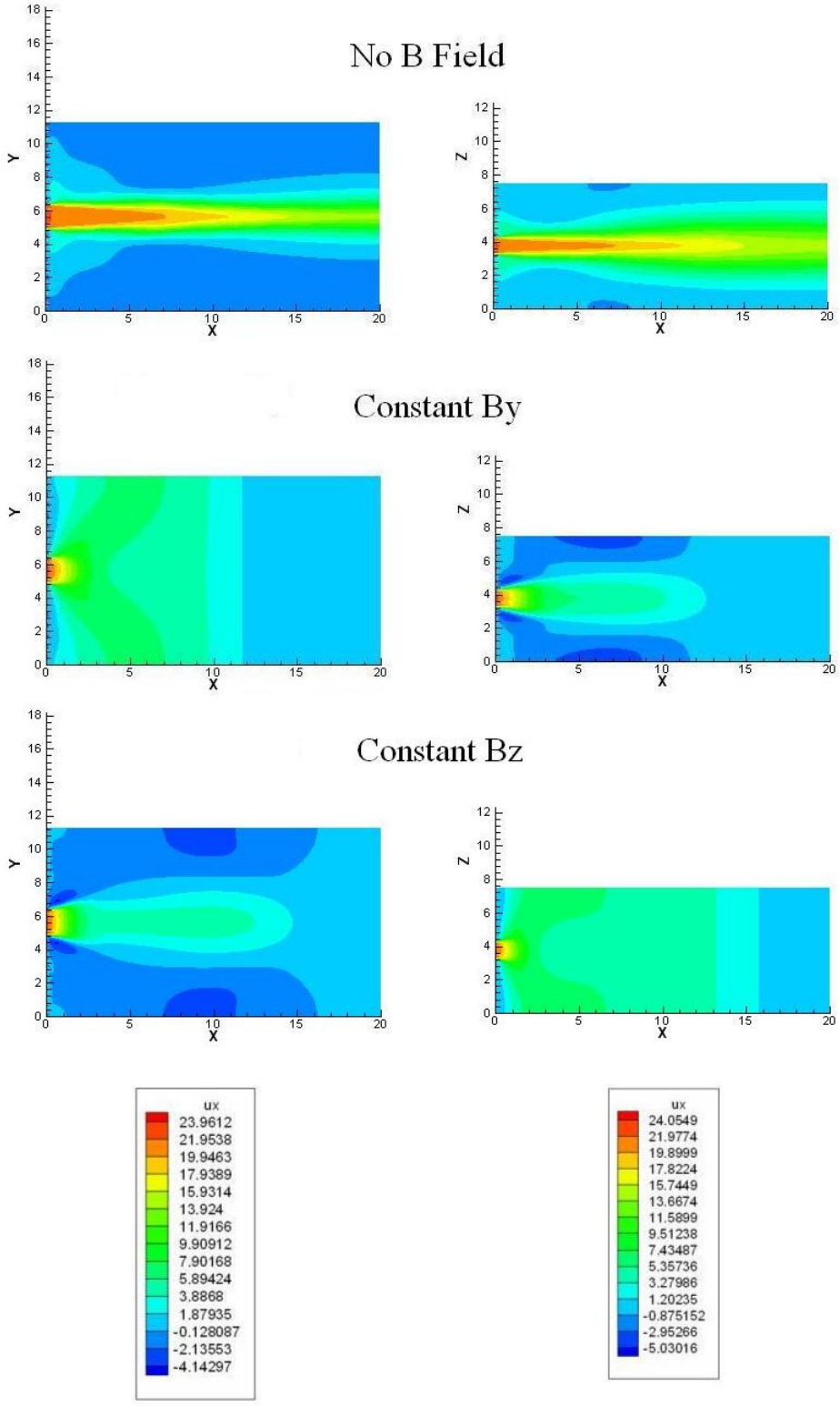

Figure 50. Comparison of Axial Velocity Contour in X-Y and X-Z Planes with and without Uniform Magnetic Field

The result indicates that the plume structure will be elongated in the direction of the uniform magnetic field, along with incurring damping effects like shown in the previous section. The reason for the elongation can be explained by the magnetic tension affect on the RJ plume. The magnetic tension is spreading out the momentum in the direction of the magnetic field, and resisting the axial motion of the plume. Figure 50 also shows that for the plane of the jet that is not elongated incurs reverse flow effects. This effect is seen by the negative velocity contour value that shows up outside of the plume.

This simulation hasn't been experimentally validated; however, Davidson [5] has done theoretical analysis, and Harada [66] has performed experiments for jet casting. In jet casting, a circular (axis-symmetric) jet is produced under the influence of a uniform transverse magnetic field. Physically, the simulations of this section are only different because of the RJ geometry, but the same effects should occur. [5 and 66] find that the jet plume structure is elongated in the direction of the uniform magnetic field, which agrees with the results of this simulation. Figure 51 contains drawings provided by Davidson that theoretically explain and justify the physical effects taking place.

Figure 51.a shows the spatial evolution of the jet and elongation of the plume in the direction of the magnetic field. Figure 51.b illustrates how the jet draws in fluid from the far field, and that the reverse flow produces an outward flow of mass near the wall. These physical effects on the jet flow can be seen in the results of figure 51.

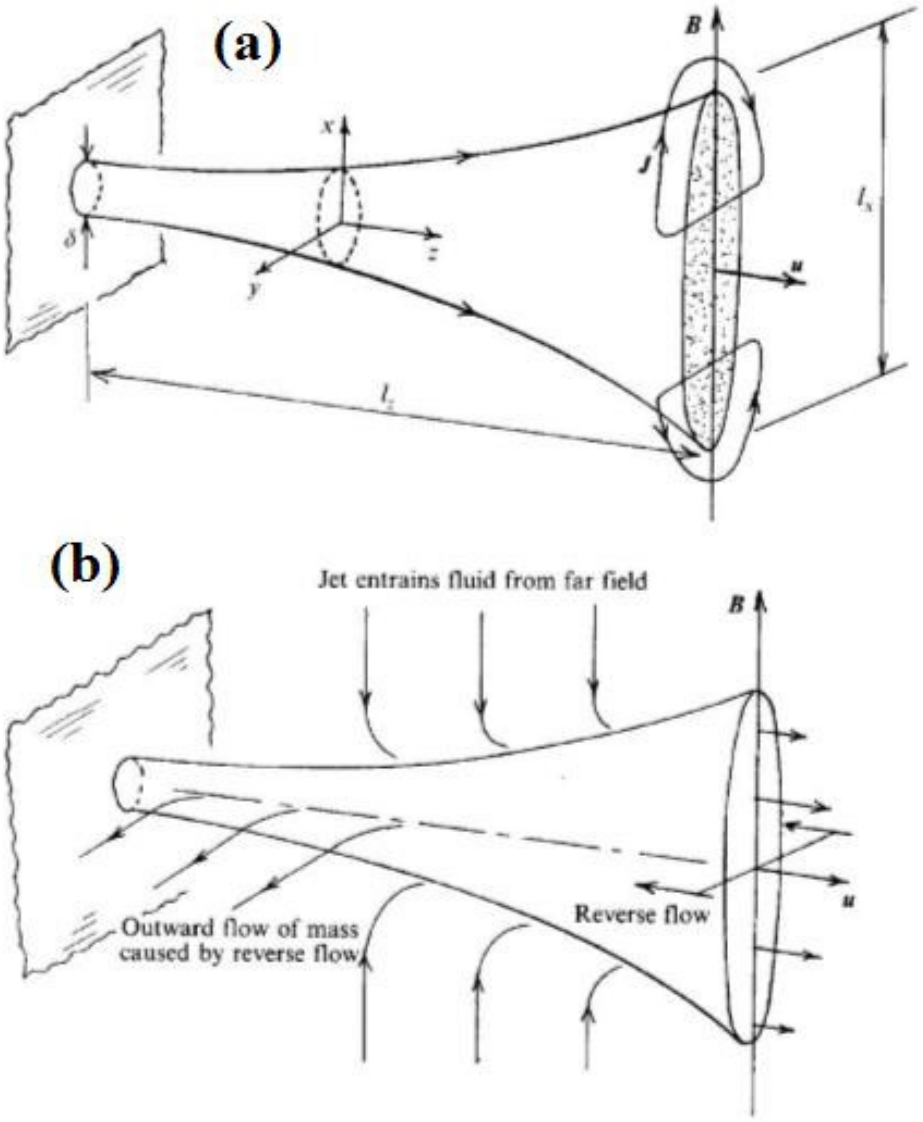

Figure 51. Theoretical Analysis of MHD Jet Produced by Sidewall Injection [5]

Davidson [5] describes the effect of the uniform magnetic field as rearranging the angular momentum of the flow so as to reduce the global kinetic energy. The flow reaches a steady state when the angular momentum is uniform in the direction of the magnetic field lines. This rearrangement can be analyzed by the change in the axial vortex structures.

Figure 52 shows that the axial vortex structures located five jet exit height lengths away from the jet exit (X=5H). The axial vortex structures are clearly elongated in the direction of the applied uniform magnetic field. These trends also correspond to experimental and theoretical studies on vortices by uniform magnetic fields, provided earlier in the paper.

This comparison to Davidson's studies provides physical verification of the RJ simulations being performed, giving some credibility for the results to be presented further in this study.

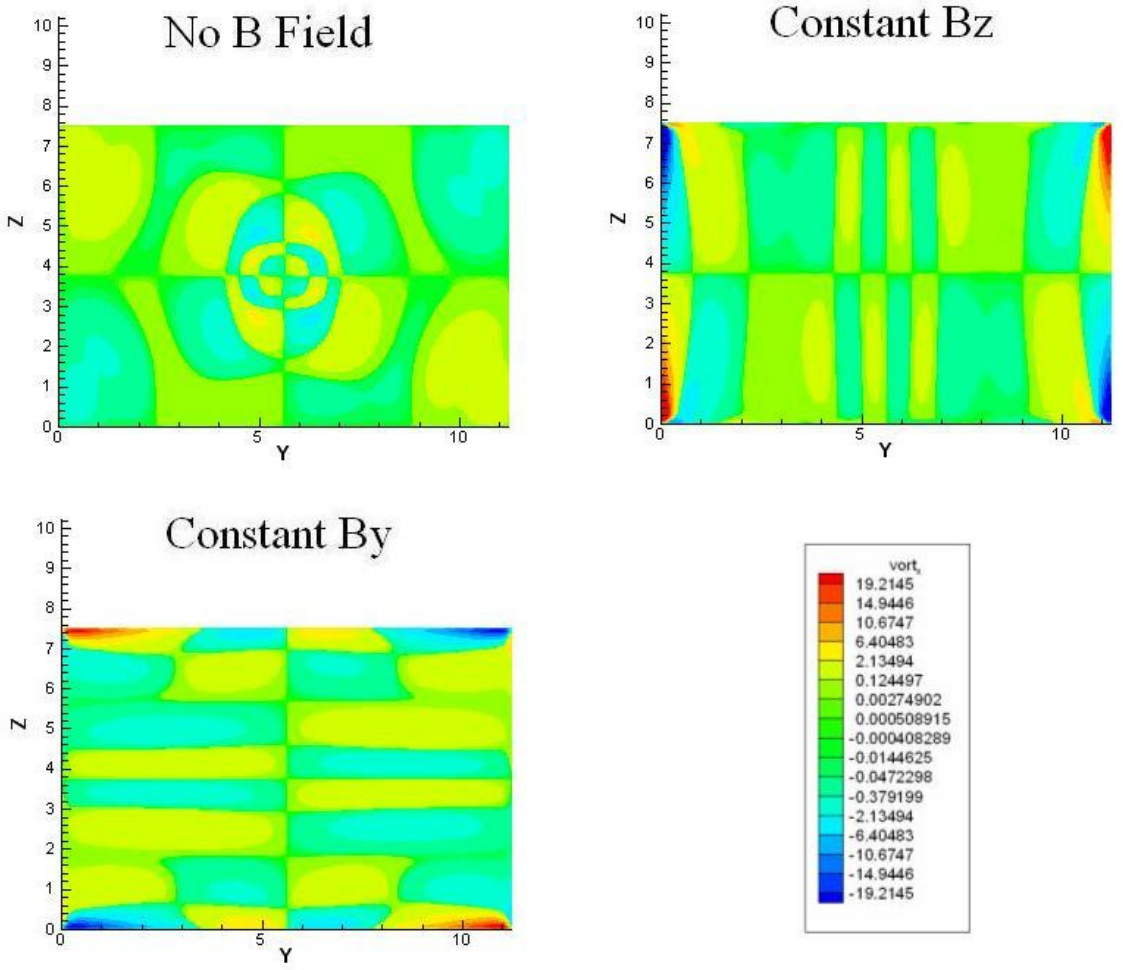

Figure 52. Comparison of Axial Vorticity Contour in Y-Z plane with and without Uniform Magnetic Field at X=5H

4. Magnetic deceleration of Re=10 RJ Flow Using a Circular Current Loop

This section analyzes laminar Re=10 jet flow at varying magnetic field strengths and magnetic Reynolds numbers. The uniform velocity is 1.5 cm/s. The ratio of kinetic to magnetic energy, β is used to characterize the magnetic field influence at various magnetic field strengths.

a. 3-D MHD Results with Varying External Magnetic Field Strengths

This section analyzes the jet flow deceleration by changing the circular current loop strengths to vary the external magnetic field values. The results in figures 47 and 48 show a trend in the decay of axial velocity and increased entrainment that indicate the redirection of momentum and energy taking place. Figure 53 shows the decay of the axial velocity and how the decay rate increases with a stronger magnetic field. The axial velocity contours in figure 54 visualize the increased damping effect that increasing the magnetic field strength has on the jet flow. $\beta = 3.5$ corresponds to a current of $I = 1.875$ A, and $\beta = .4$ is for $I = 5.625$ A This deceleration effect is most apparent when comparing the cases of no external magnetic field to when a strong magnetic field $\beta = .4$ is applied. Physically, this effect is taking place because the Lorentz force is redistributing momentum and energy.

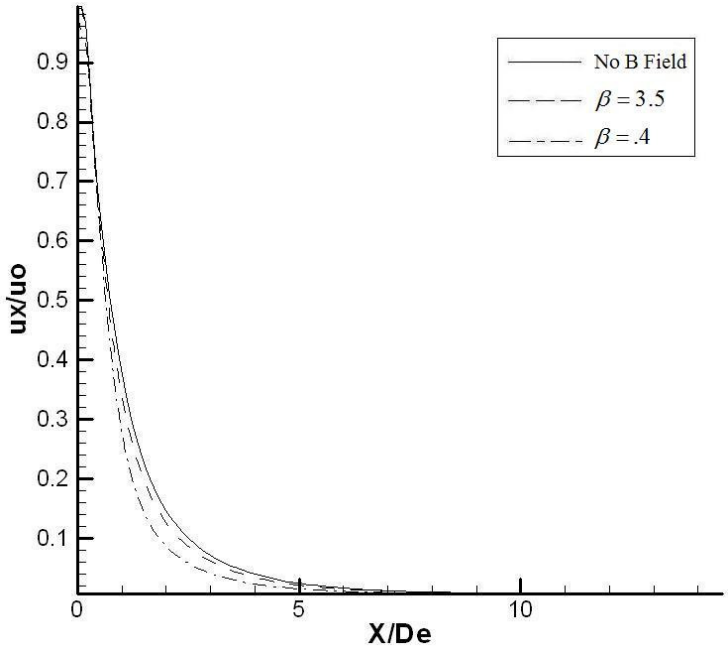

Figure 53. Jet Centerline Axial Velocity Distribution for Various Current Strengths

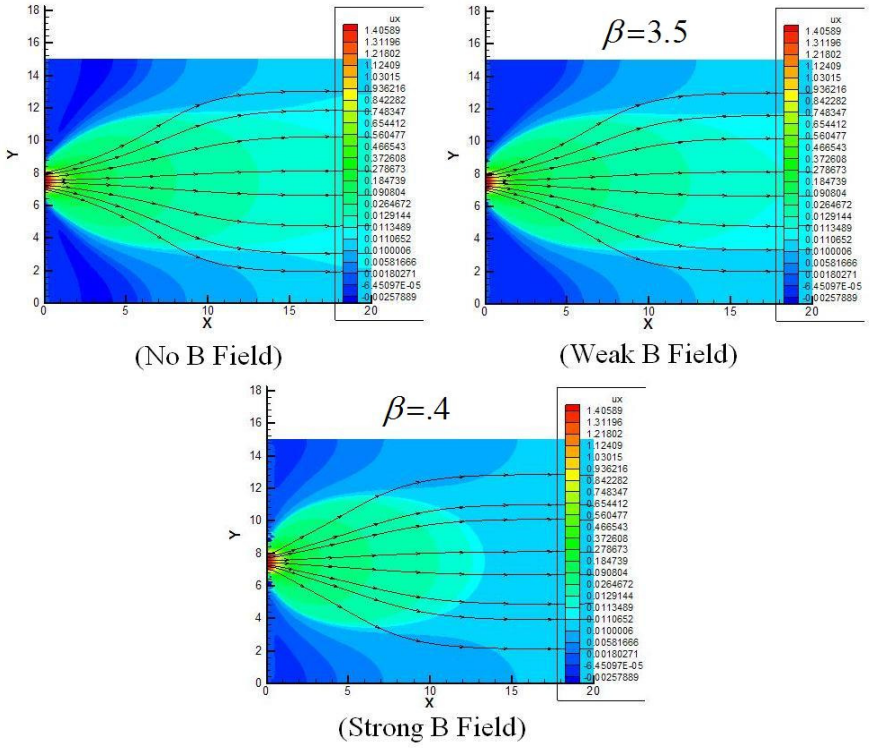

Figure 54. Axial Velocity Contour and Streamline Plots for RJ with Varying Current Strengths

Figure 55 shows the axial magnetic field contour and magnetic field lines of the weak and strong magnetic field RJ flow cases. Remembering the description of the magnetic tension effect on jet flow in chapter III (figures 16 and 17), this figure illustrates the adverse effect that the magnetic field tension will have. The direction of the exerted magnetic field tension acts against the direction of the jet flow, causing an adverse reactionary force. A stronger magnetic field, for the case of the circular current loop, corresponds to a stronger magnetic tension. Therefore as the current strength increases, the adverse force increases and enhances the deceleration. This adverse reactionary force can also be characterized by rearranging the angular momentum in such a way that causes the decrease in the kinetic energy [5].

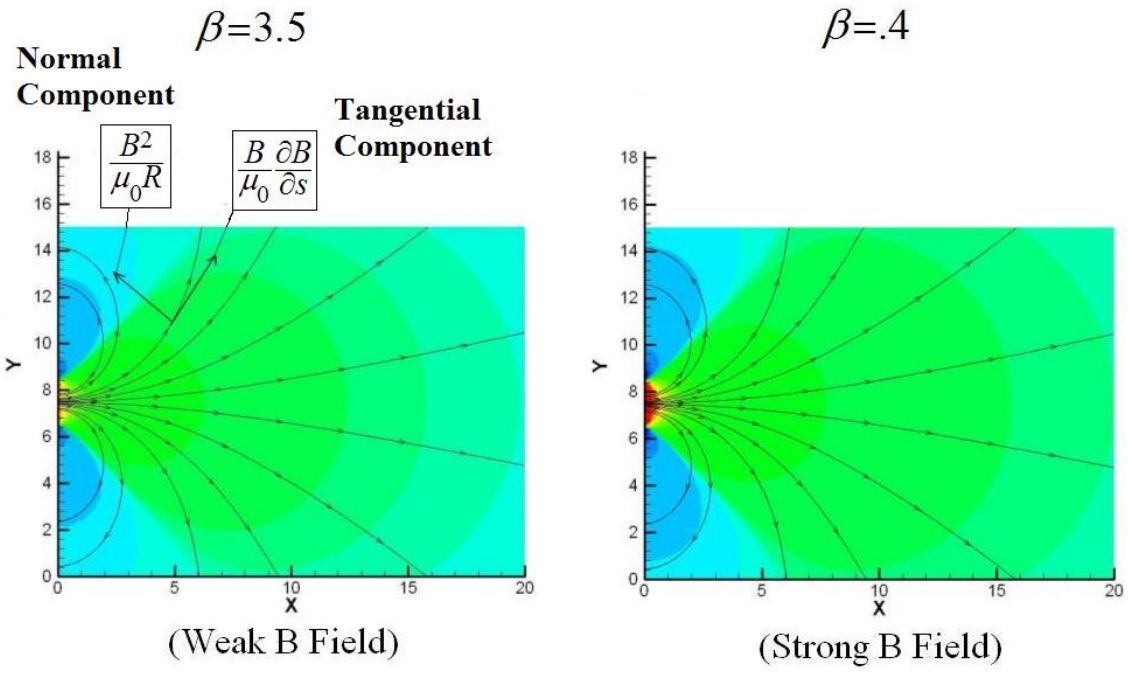

Figure 55. Magnetic Field Lines and Axial Contour Plots for Strong and Weak Magnetic Field RJ Flow Cases

This deceleration effect also corresponds to the exchange of energy from the kinetic to magnetic modes. In this case, the magnetic field lines are stretched causing the velocity to decrease and magnetic field to increase. Therefore the magnetic energy is drawing strength from the kinetic energy.

b. 3-D MHD RJ Results with Varying Magnetic Reynolds Number

This section analyzes the effect of varying the magnetic Reynolds number on the jet flow damping while keeping the current of the circular loop at a constant value of 1.875 A ($\beta = 3.5$). Figures 56 and 57 show that changes in the magnetic field due to the magnetic Reynolds number have a small impact on the velocity field for this Re=10 case. One notable trend is seen for the Rm=40 case of the decay plot for the axial centerline velocity. In this plot, the axial centerline velocity slightly increases right outside of the jet exit. Further downstream the axial centerline velocity decays at a more rapid rate to a value smaller than that of the case without a magnetic field presence. This occurs because the change in Rm changes the magnetic field configuration. The reason for the two different regions in the jet flow trends can be explained by the magnetic field, as shown in figure 58. The results show stretching of the magnetic field lines and an increase in value of the induced magnetic field as magnetic Reynolds number increases.

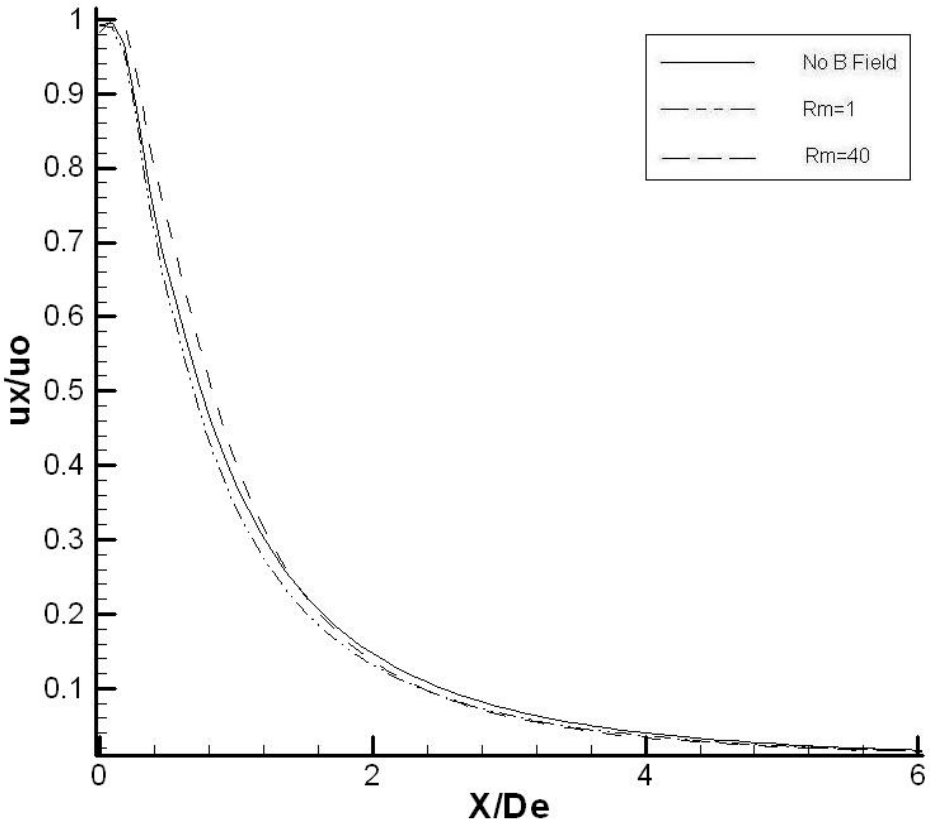

Figure 56. Jet Centerline Axial Velocity Distribution for Various Magnetic Reynolds Numbers

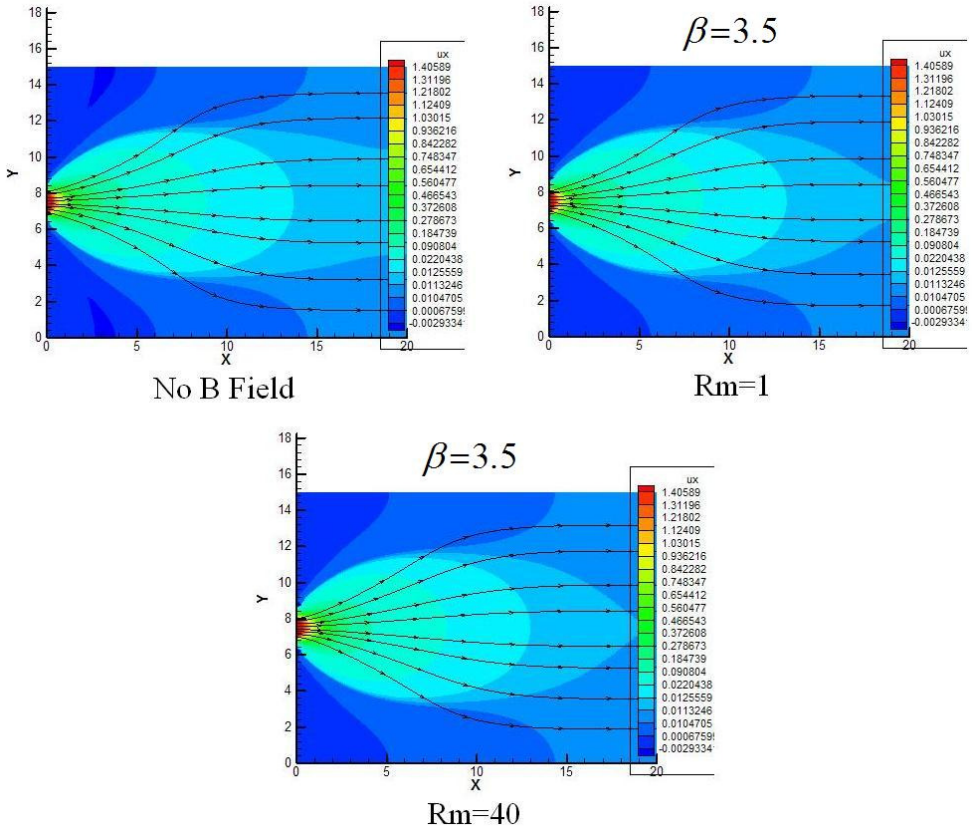

Figure 57. Axial Velocity contour and Streamline Plots for RJ with Varying Magnetic Reynolds Numbers

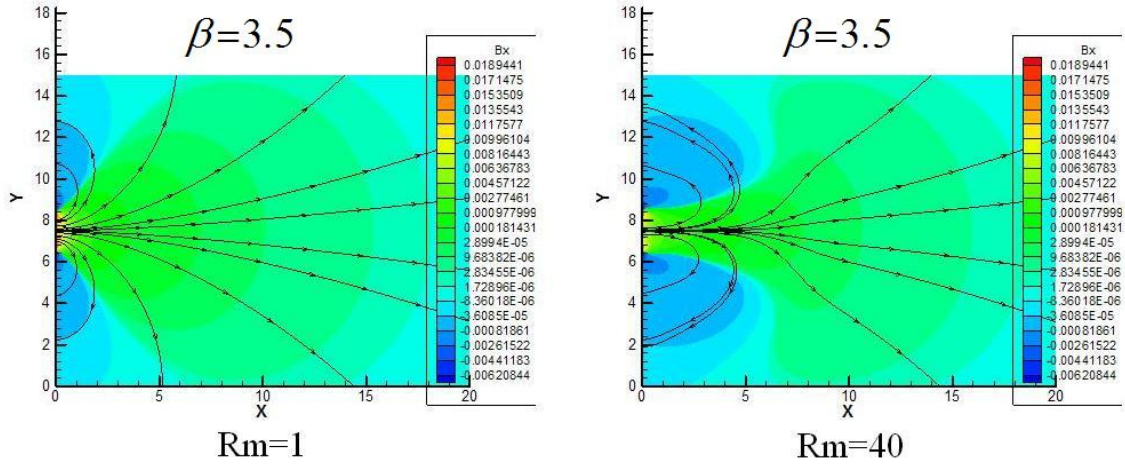

Figure 58. Magnetic Field Lines and Axial contour Plots for Rm=1 and Rm=40 RJ Flow Cases

Figure 58 shows that for Rm=40, the curvature in the magnetic field lines near the inlet, become sharper, corresponding to an acceleration of the flow field. This effect correlates with the axial velocity decay characteristics near the jet exit. The magnetic field lines are stretched out from their previous configuration of the Rm=1 case because, at larger Reynolds numbers, the magnetic field is more highly coupled to the velocity field. Physically this means that the magnetic field is being stretched by the flow of the molecules. Davidson [5] provides justification of these physical effects in his observation of the elongation of the jet as mentioned earlier. Further down the flow field, the curvature of the magnetic field lines for Rm=40 curve inwards while extending out away from the axial direction corresponding to an adverse effect on the flow field. This trend properly corresponds with velocity decay characteristics far away from the jet exit. The reason for this change in the magnetic field is because the induced magnetic field is gaining strength from the effect of higher coupling to the velocity field.

Figure 59 shows the change in the ratio of the induced to the external magnetic fields as the magnetic Reynolds number is increases along the centerline of the jet flow. At the region near the inlet in the core of the jet flow, where the magnetic field lines become sharper, the induced magnetic field is strengthening the axial magnetic field, making the overall magnetic field gradient more favorable. Physically, this can be correlated to the strength of the axial momentum of the jet flow in that region, showing that the coupling to the velocity field is enhancing the magnetic field affect on the flow.

These results show that the magnetic Reynolds number can be an important parameter to consider when studying effects on jet flow because this parameter alters the evolution of the induced magnetic field.

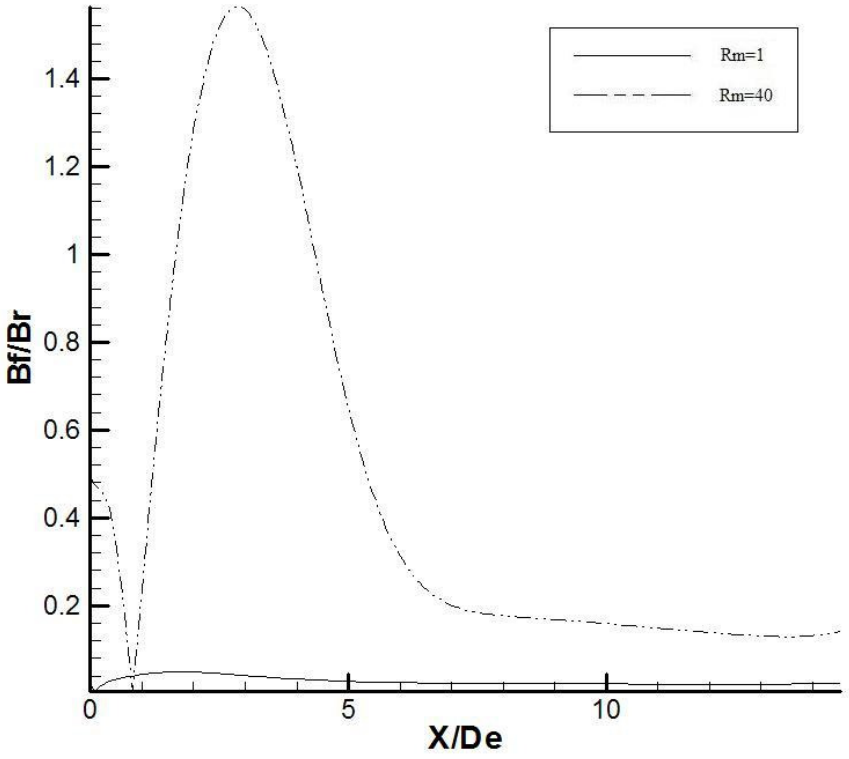

Figure 59. Ratio of Induced to Externally Applied Magnetic Field at Rm=1 and Rm=40

5. Circular Current Loop Influence on RJ Vorticity and Axis-Switching

This section analyzes laminar Re=150 jet flow at varying magnetic field strengths. The various current strengths correspond to the following β and N values.

- $I = 14.0625$ A $\Rightarrow \beta$=13.38, $N = 0.747$
- $I = 21.0938$ A $\Rightarrow \beta$=5.95, $N = 1.681$
- $I = 24.61$ A $\Rightarrow \beta$=4.37, $N = 2.288$
- $I = 28.125$ A $\Rightarrow \beta$=3.35, $N = 3.0$

These parameters, for each current strength, are useful in describing the magnetic field dominance over the kinetic energy and vorticity dynamics of the RJ flow. The uniform velocity is 22.5 cm/s. The jet flow profiles at varying magnetic field strengths

generated by a circular current loop are analyzed to see the affect on axis-switching. Then the magnetic field effect on vorticity development is shown to explain the physical mechanisms behind the prevention of axis-switching. This section concludes with a discussion about the driving mechanism behind the magnetic field effect on the vortex structures and jet profile.

a. Prevention of Axis-Switching by the influence of a Circular Current Loop

Jet flow profiles are plotted in the streamwise plane at various locations from the jet exit plane. The profiles are determined by plotting the half-width velocity profiles. This means that all computational nodes with a velocity greater than or equal to half the maximum velocity of that streamwise plane are included in the jet profile.

Figure 60, shows how the RJ flow profile appears at various distances from the jet exit, scaled by the jet exit height (H). At X=H, 3H, and 8H, the RJ profile is oval shaped and elongated with the major axis. At X=11H, the RJ profile becomes elongated with the minor axis. This differential growth in the shear layers between the major and minor axis is the axis-switching phenomena. For this case, the axis-switching is 90 degrees, which agrees with experimental trends found by Grinstein and Gutmark [57-61] for RJ's. Tsuchiya [63] did experimental work with AR=1.5 RJ's and found axis-switching to occur at 10H from the jet exit. His flow field parameters were very different and therefore can not be directly compared to these simulations. The similar trend is, however, encouraging as the physical effects of axis-switching appear to be effectively demonstrated by the lattice Boltzmann method.

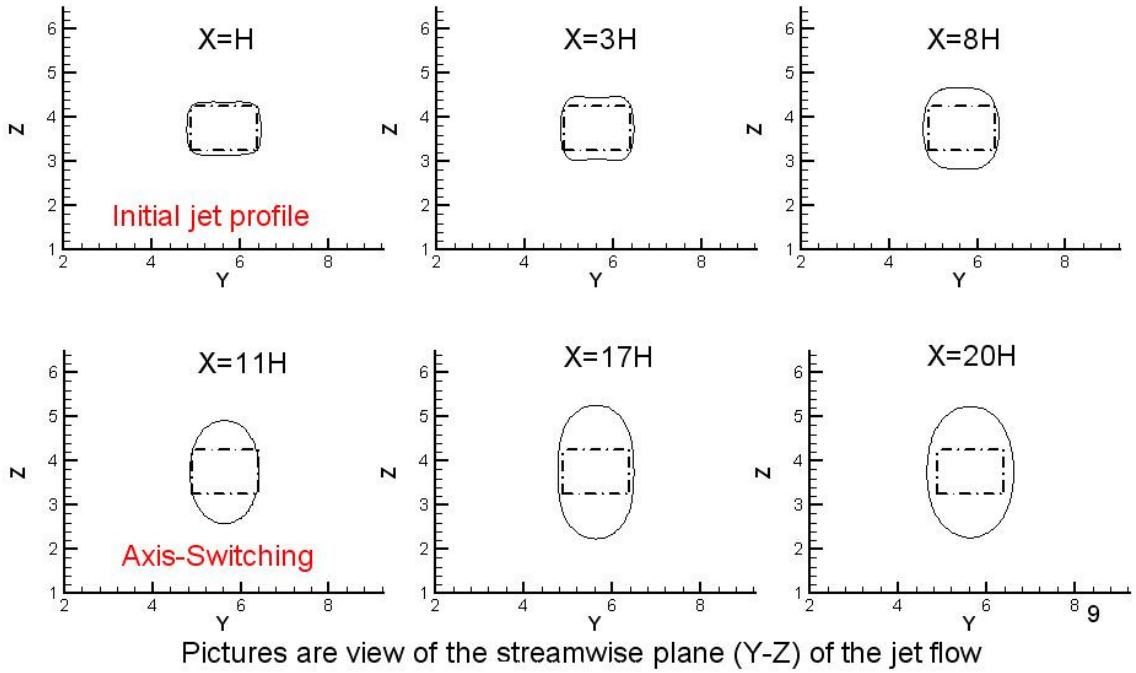

Figure 60. RJ Flow Profiles for Re=150 and No Magnetic Field Influence

Figure 61, shows the RJ flow profile under the influence of a magnetic field with β=4.37 and $N = 2.288$. This is roughly the required magnetic field influence, with a circular current loop, to prevent axis-switching. Starting at X=3H, the jet profiles all look more elongated in the major axis direction. After X=llH, the profile becomes axis-symmetric. Due to the magnetic field, the evolution of the vortex structures changes causing the shear layer growth in the major axis to be faster than that for the minor axis.

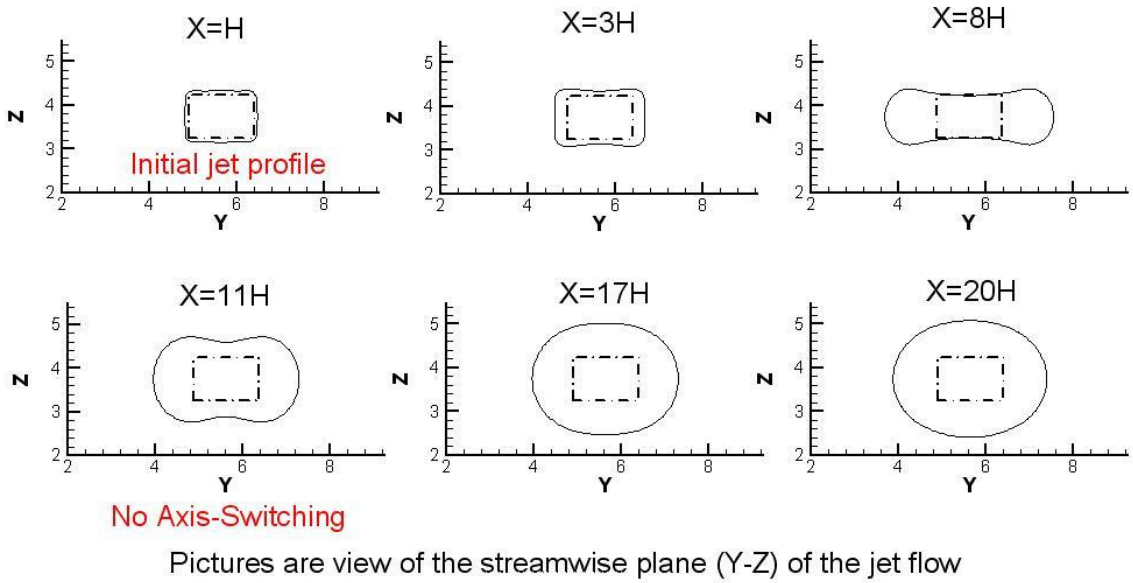

Figure 61. RJ Profiles for Re=150 Under Magnetic Field Influence at Rm=5

These results have not been experimentally validated, however, an analysis of the vortex structures correspond to similar experimental trends.

Figure 62, shows the RJ flow profile under the influence of a magnetic field with β=3.35 and $N = 3.0$. This stronger magnetic field presence causes even more elongation of the RJ profile in the major axis direction, and the profile does not become axis-symmetric by 20H away from the jet exit.

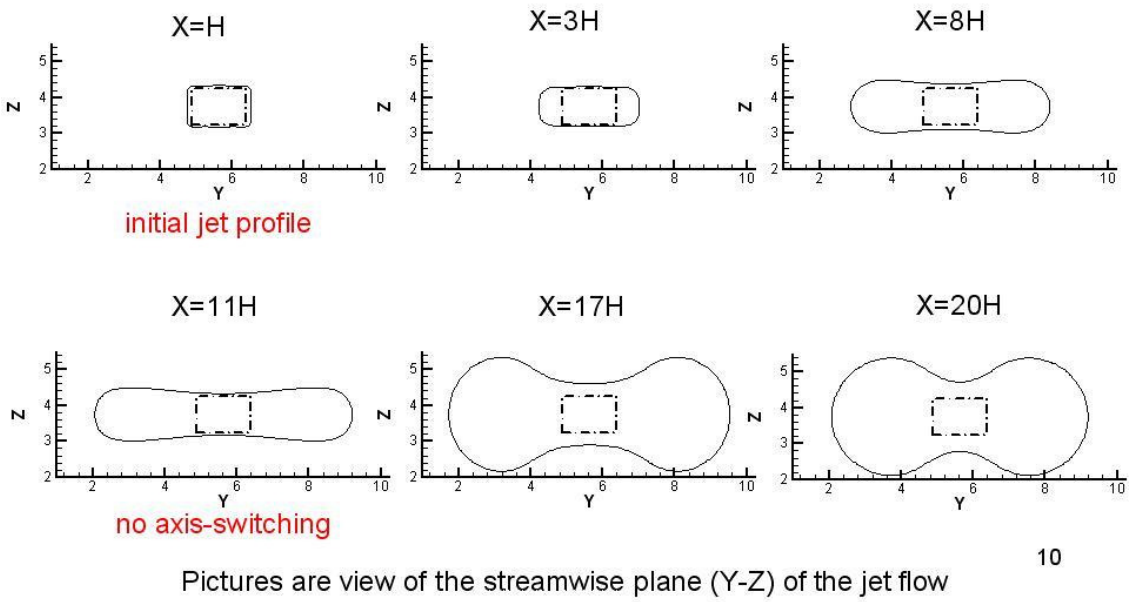

Figure 62. RJ Flow Profiles for Re=150 Under Strong Magnetic Field Influence at Rm=5

b. Axial Vorticity Dynamics under influence of a Circular Current Loop

In order to understand why a strong circular current loop magnetic field prevents axis-switching, the axial vortex structures generated by the RJ must be analyzed. For the case of normal RJ flow, it is already known from experimental studies that secondary flows deform the coherent structures [57-63]. It is also known theoretically that a strong magnetic field presence can generate other secondary flows and affect the evolution of the vortex stretching mechanism [5].

Figure 63 shows an axial vorticity contour plot at X=11H from the jet exit for five difference current strengths. The magnetic field effects are very notable between each plot of this figure. For the weakest magnetic field (β=13.38 and $N = 0.747$), the vortex structures are damped out. This effect on a vortex structure by a weak magnetic field influence is verified by Davidson [5]. When β=5.95 and $N = 1.681$, the vorticity alignment is changing and the vorticity strength is increasing. For a strong magnetic field (β=4.37 and $N = 2.288$), the vorticity alignment changes and becomes strong enough to prevent axis-switching. Then with an even stronger magnetic field presence

(β=3.35 and $N = 3.0$), the intensity of the vortex structures increases. The reverse flow alignment of the vortex structure with the strong magnetic fields corresponds to Davidson's observation of reverse flow with strong interaction parameters.

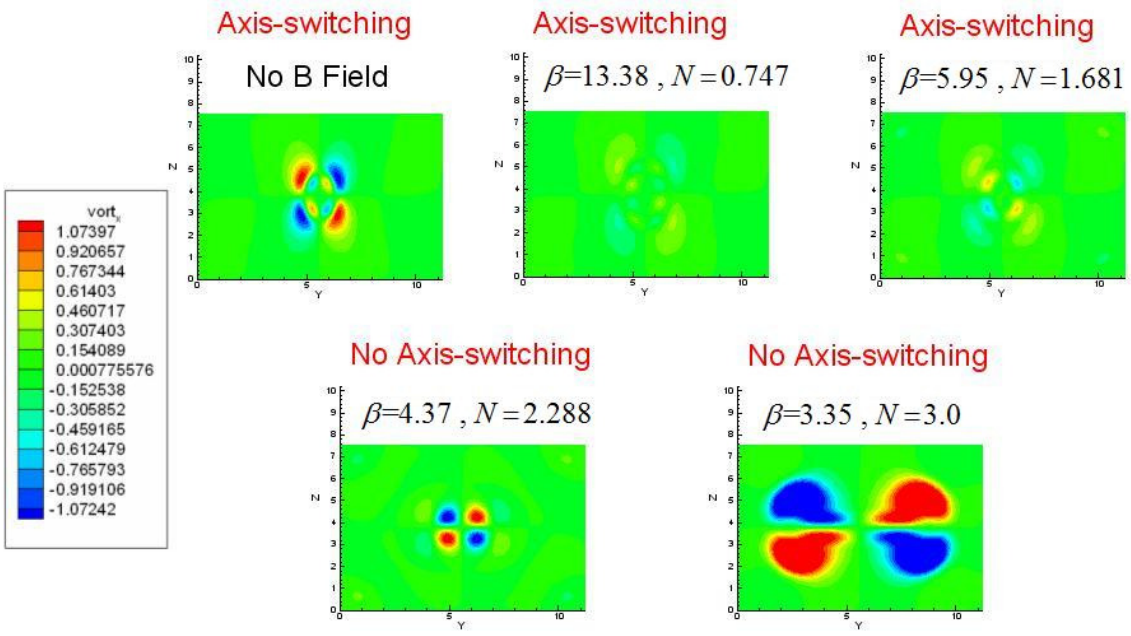

Figure 63. Axial Vorticity Contour Plot at X=11H for Varying Magnetic Field Influences

In figure 64, axial vorticity contour plots at X=3H, 5H, and 8H for RJ without a magnetic field and with a strong magnetic field (β=3.35 and $N = 3.0$) are shown.

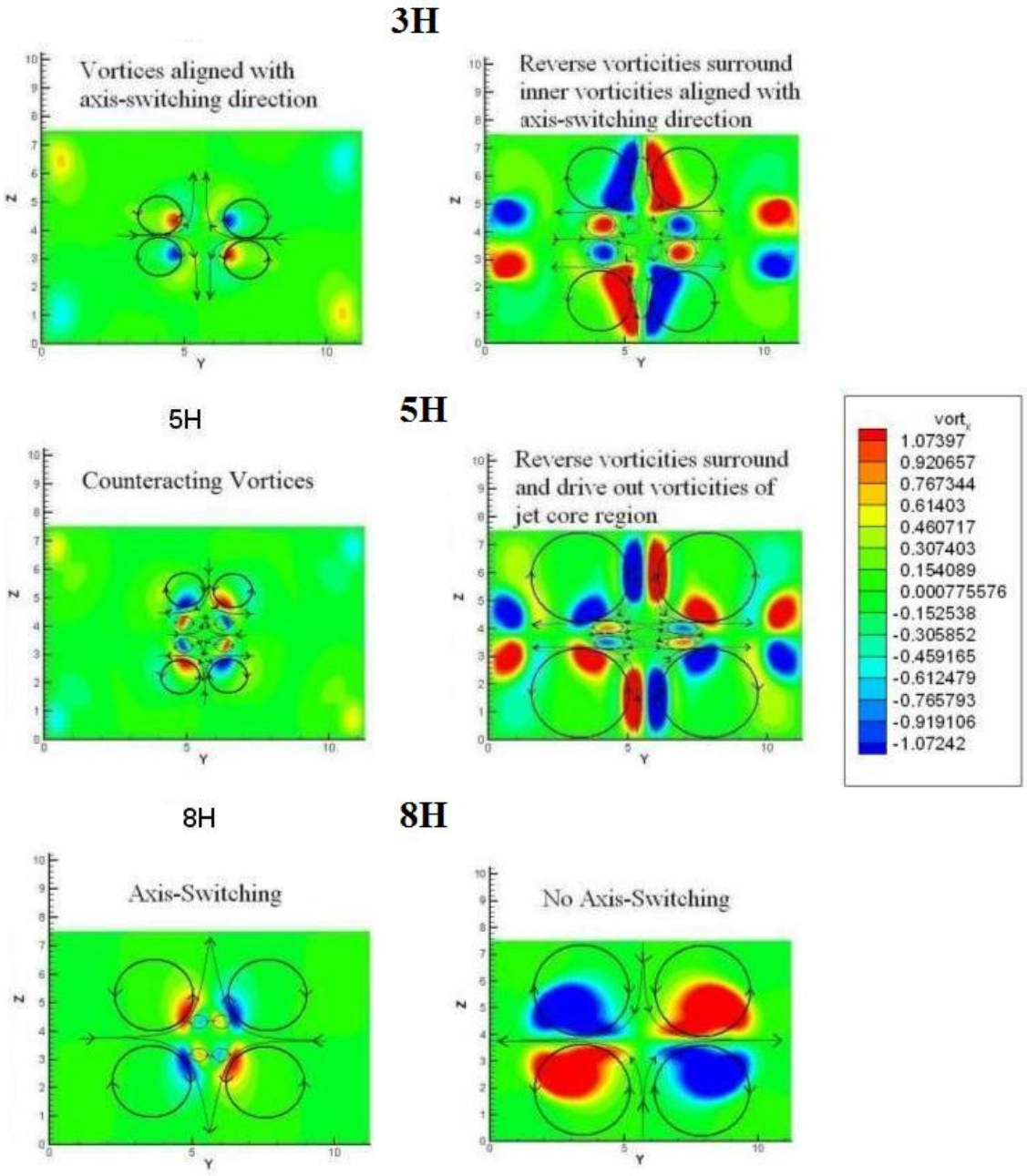

Figure 64. Axial Vorticity Contour Plot with and without a Strong Magnetic Field at X=3H, 5H, and 8H

The flow circulation lines are drawn on the figure, externally, to provide a clear view of the direction of circulation of the fluid. Figure 64 helps to understand the spatial development of the vorticity of the RJ. At X=3H, the strong magnetic field appears to

generate reverse flow vortex structures around the inner vortex structures of the jet core region, which are aligned with the minor axis direction. At X=5H, the reverse vortex structures both weaken the inner vortices of the jet core region and merge with them. Then at X=8H, the reverse vortex structures are dominating the entire plane, preventing axis-switching.

Figure 65 illustrates how the direction of the RJ axial vorticity dictates the shear layer growth.

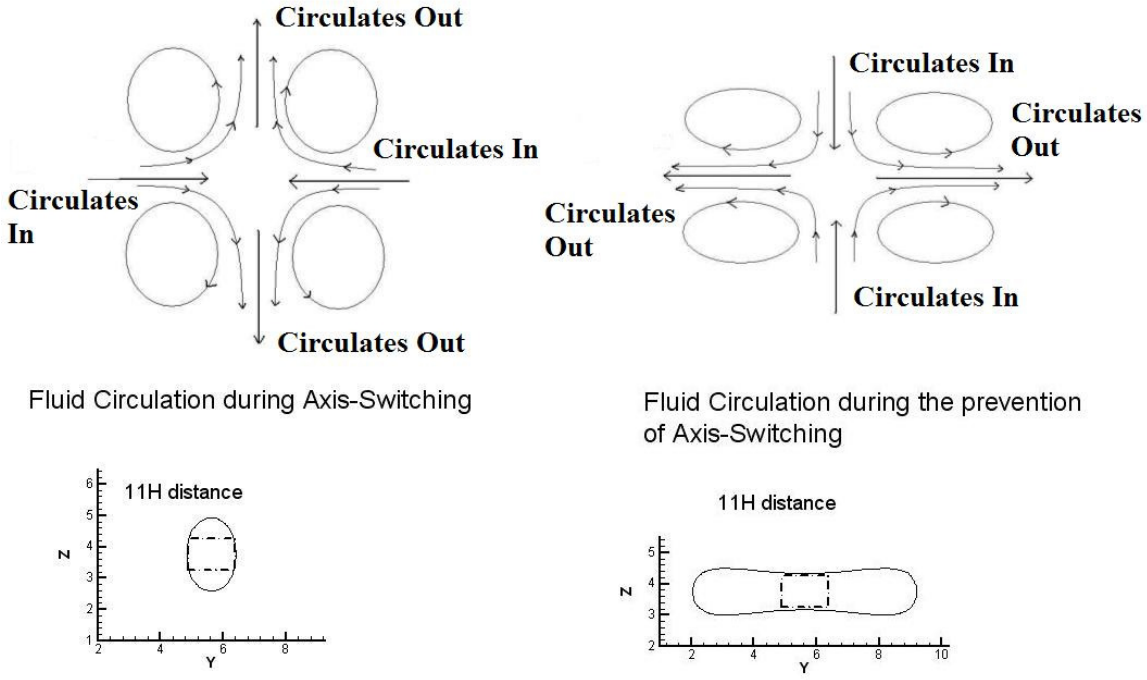

Figure 65. Illustration of Relationship between RJ Axial Vorticity and Axis-Switching

For the case without a magnetic field, the vorticity at X=11H, will draw fluid from the major axis and circulate it to the minor axis. When a strong circular current loop is present, fluid from the minor axis is drawn inwards and circulates in the major axis. The change in the vortex structure deformation caused by the circular current loop is responsible for this process, and the direction of the vortices corresponds with the associated jet profiles.

c. Y/Z Vorticity Dynamics under influence of a Circular Current Loop

Thus far, effects on the axial vorticity have been evaluated and used to explain the occurrence and prevention of axis-switching. The y and z components of vorticity are now analyzed to provide a different perspective of the change in growth of the shear layers due to the magnetic field. These traits are another way of analyzing the jet flow profile and axis-switching phenomena.

Figures 66 and 67 provide the z and y vorticity component contours. The z-vorticity is plotted in the x-y plane at the center of the computational domain, while the y-vorticity is in the x-z plane at the center of the domain. The z component of vorticity corresponds with the shear layer growth in the major axis direction (y), and y-vorticity represents the shear layer growth in the minor axis direction (z).

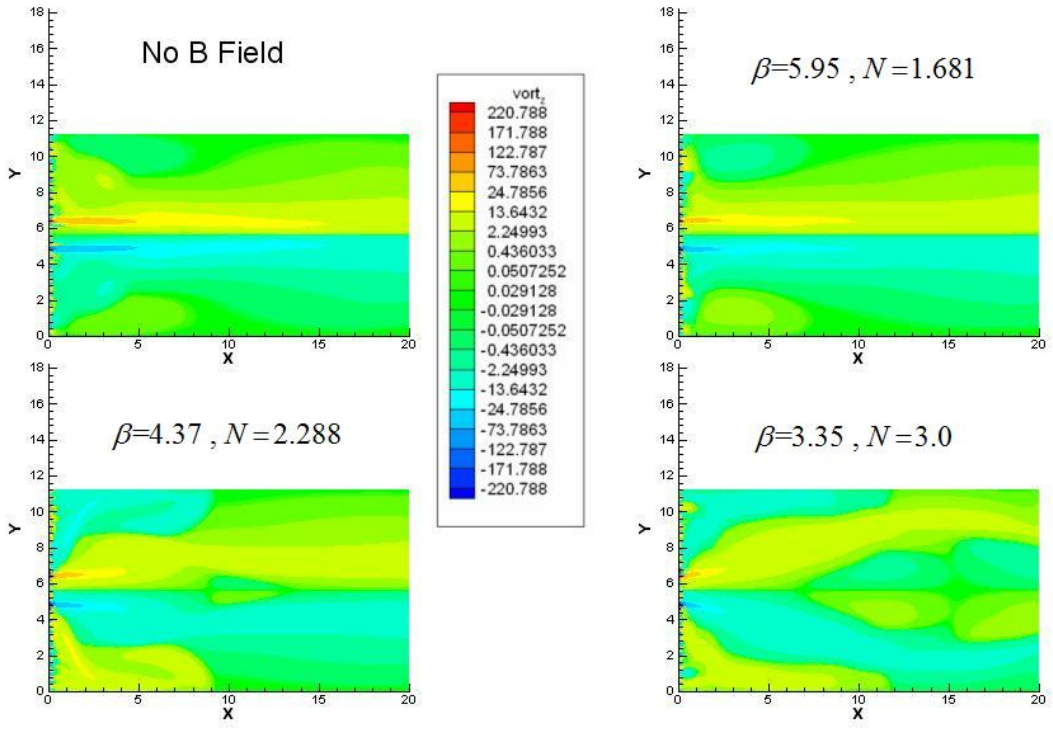

Figure 66. Z-Component Vorticity Contour Plot of X-Y Plane for Various Magnetic Field Influences

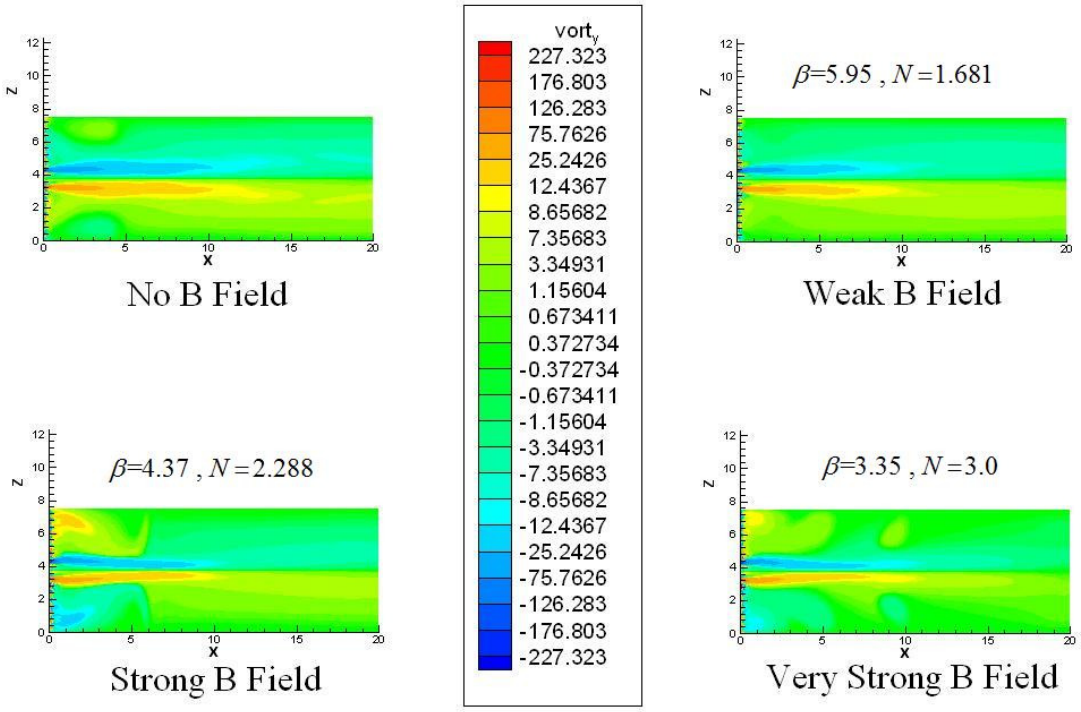

Figure 67. Y-Component Vorticity Contour Plot of X-Y Plane for Various Magnetic Field Influences

Without a magnetic field influence, the y and z-vortices squeeze inwards initially in the potential core region. Then in the characteristic decay regime, the vortices spread outwards gradually. In the axis-symmetric decay region, the vortices do not significantly spread anymore. In the characteristic decay region where both vortices spread outwards gradually, the y-vorticity spreads outwards at a greater rate than the z-vorticity. This trend means that the shear layer in the minor axis direction is growing at a greater rate than the shear layer in the major axis direction. This physical effect agrees with the axis-switching phenomena taking place.

When the weak magnetic field is present (β=5.95 and $N = 1.681$), there is a slight change in the z and y vortices. The y-vorticity squeezes inwards and the z-vorticity spreads outwards. The change is small enough that the shear layer of the minor axis still grows faster than the shear layer of the major axis. When the magnetic field strength increases further (β=4.37 and $N = 2.288$), the z-vorticity spreads outward greater than the y-vorticity does. Coincidentally, axis-switching is no longer occurring,

corresponding to the larger shear layer growth of the major axis. When the magnetic field strength increases again (β=3.35 and $N = 3.0$), the z-vorticity continues to spread out further, while the y-vorticity squeezes inward even more. The shear layer growth of the major axis becomes much greater than that of the minor axis. This change in shear layer growth causes the jet profile to become very elongated in the major axis direction as shown in figure 62.

Figure 66, along with describing the shear layer growth of the major axis, also shows the development of reverse z vortex structures downstream of the jet exit. These vortex structures develop in the characteristic decay region and correspond to the outward spread of the z-vorticity. These reverse vortex structures force out the z-vorticity of the jet core, which causes the jet profile to stretch outwards in the major axis direction.

Figure 68 is a comparison of the axial velocity contour, in the x-y and x-z planes at the center of the computational domain, between RJ flow without magnetic influence and with a strong magnetic field presence (β=3.35 and $N = 3.0$).

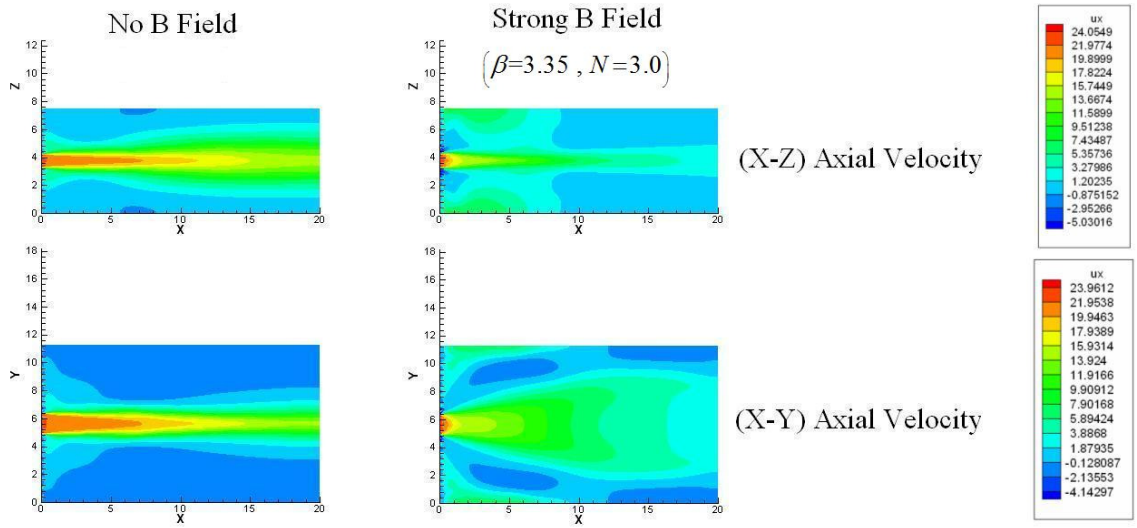

Figure 68. Comparison of Axial Velocity Contour in X-Y and X-Z Planes with and without Magnetic Field Influence

In the x-z plane, the axial velocity contour or jet plume damps and thins out in the minor axis direction by the strong magnetic field. In the x-y plane, the axial velocity contour damps out and stretches in the major axis direction. These effects correlate with the associated y and z vortices, showing a strong effect on the jet plume structure by the circular current loop.

6. Circular Current Loop Influence on Unsteadiness

This final results section further analyzes a circular current loop's effect on flow field instabilities through the prevention of RJ unsteadiness. In normal RJ simulations, unsteadiness begins at about Re=160. When a strong current giving β=3.35 and $N = 3.0$ is applied to a circular current loop for the same RJ simulation, unsteadiness begins at approximately Re=170.

Figure 69 demonstrates the effect that a strong magnetic field exerted by a circular current loop has on unsteady RJ flow. For this case, unsteadiness is approximately delayed until Re=170. At Re=170 for the strong magnetic field case, the oscillation in the RJ plume is extremely small. Unsteadiness hasn't exactly set in yet, however, it is beginning at Re=170.

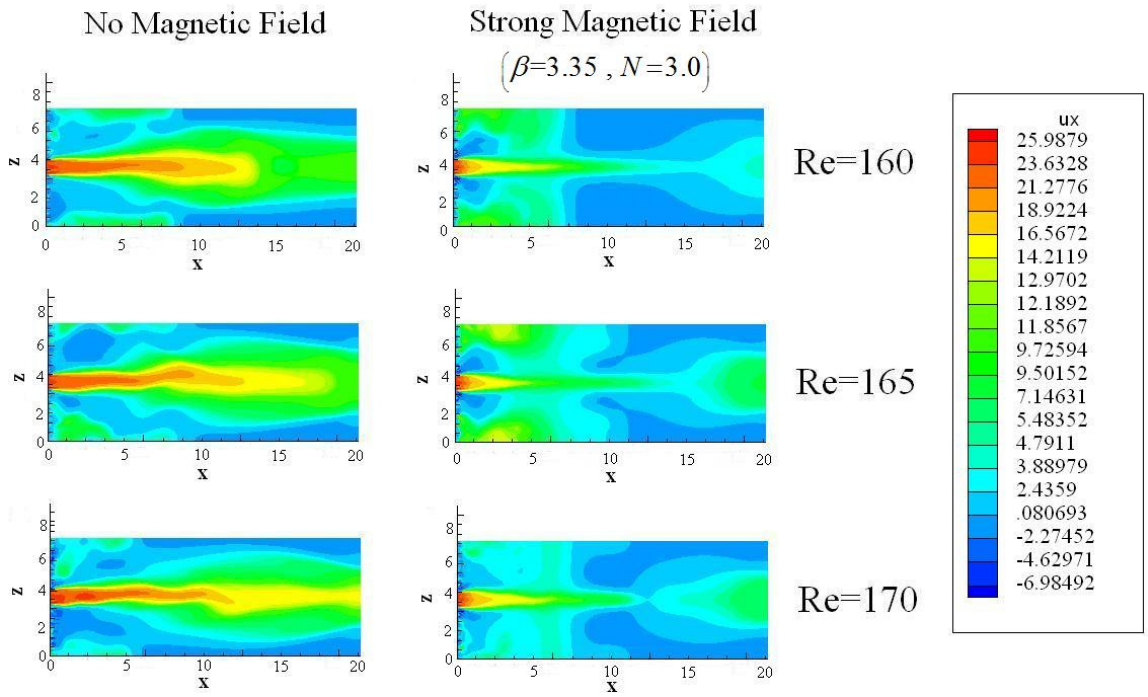

Figure 69. Axial Velocity Contour Plots for Unsteady RJ Flow with and without Magnetic Field Influence

For the normal Re=160 RJ flow case, the velocity shear releases a sufficient amount of energy to overcome the viscous damping effect and create instability in the flow field. This mode of instability related to velocity shear is Kelvin-Helmholtz instability. Biskamp [52] has studied stabilizing jets and vortex sheets using magnetic fields. He found that a strong magnetic field parallel to the flow stabilizes the Kelvin-Helmholtz mode. This damping of the perturbations is due to the magnetic field line bending that absorbs kinetic energy from the sheared velocity. Figure 69 can be compared to figure 44. In figure 44, Biskamp compares the instability of an un-magnetized to a magnetized jet. A parallel magnetic field is exerted on the jet of the right hand side and damps out the Kelvin-Helmholtz instability. Figure 44 presents results of similar trends to that of figure 69. The simulations, in the case of figure 69, have all three magnetic field components, however, the axial magnetic field is the most dominant component. Therefore, a circular current loop is capable of damping out the Kelvin-Helmholtz instability mode and delaying the onset of unsteadiness.

E. Conclusion

The kinetic-magnetic energy interaction and the magnetic tension are the key physical mechanisms in MHD RJ flow. These mechanisms cause jet flow damping, deform and elongate vortex structures, and damp perturbations that prevent unsteadiness. The Lorentz-force work mechanism is the key term in describing how the kinetic and magnetic energy interact. This characteristic of MHD flows is extremely important as jet damping is a common application and because the Kelvin-Helmholtz instability mode is damped by the absorption of the kinetic energy by the magnetic field. The results demonstrate that a circular current loop will cause these effects of jet flow damping and the prevention of unsteadiness.

The magnetic field impact on the vorticity development in RJ's describes how the vortex structures are reversed from their natural orientations, driven by the vortex stretching. Earlier in this paper, observations and works in [57-63] noted that in axis-symmetric jets the merging vortex behavior is more dominant than the self-induced vortices. Grinstein and Gutmark [57-61] also demonstrate that tabs can be used to create streamwise vortices that prevent axis-switching. In this case, the strong magnetic field presence is creating streamwise vortices that are preventing the axis-switching. The vortex merging behavior exhibited in the strong magnetic field case also demonstrates similar vortex behavior as in axis-symmetric jets. Overall, the presence of the circular current loop, surrounding the rectangular jet exit, seems to have the effect of maintaining the natural geometric profile or exaggerating it in the direction of the preferred (major) axis.

These studies of the impact of the magnetic field generated by a strong circular current loop, on inherently unstable RJ's, show strong potential for magnetic field flow control applications to plasma jets. The effective control of the shear layer growths, flow and vortex structures, along with kinetic-magnetic energy manipulation, in the simulations indicate that magnetic field influence is extremely vital in future plasma jet research.

CHAPTER VIII

CONCLUSION

The physical description and application of magnetohydrodynamics in homogeneous turbulence and rectangular jet flows are presented in this thesis. From both of these studies, the most significant physical mechanisms in this context of MHD arise from the kinetic/magnetic energy interaction and magnetic field influence on vorticity structures.

This thesis demonstrates the kinetic theory description of plasmas, and uses that description to formulate the numerical simulation scheme (MHD-LBM). This approach, while having limitations, provides a different methodology in which to describe MHD flows. The potential advantage of using a kinetic theory based modeling approach is that it has the possibility of being extended into a wider spectrum of regimes aside from continuum. As kinetic theory based models are improved, rarefied gas regimes will be more readily modeled using approaches fundamentally similar to LBM.

In the simulations of MHD homogeneous turbulence, MHD-LBM produces encouraging physical results. With only a random fluctuating magnetic field influence, forward cascading increased. This occurs because the fluctuating magnetic field adds to the isotropic trends of the turbulence. Under the influence of a uniform mean magnetic field, the vorticity structures are dominated by current density stretching. This mean production force drives the turbulence towards a quasi two-dimensional state, causing inverse cascading. This two-dimensional characteristic, generated by a mean magnetic field, is a well-studied and documented phenomena. This study shows that MHD-LBM can attain proper physical trends in studying MHD turbulence.

The MHD RJ flow simulations demonstrate strong magnetic field influence on the structure of a plasma RJ exhaust. The basic physics in this case is the same as in the homogeneous turbulence simulations. The kinetic/magnetic energy exchange produces jet flow deceleration and also damps out the Kelvin-Helmholtz instability mode that induces unsteadiness. The axis-switching phenomena is strongly affected by the magnetic field impact on vorticity development in the RJ structure. By applying a strong

axis-symmetric magnetic field, from the circular current loop, the initial RJ flow profile is maintained due to the direction of the vorticity structures generated by the external magnetic field.

These key physical mechanisms, affecting both homogeneous turbulence and RJ flow, show that, in plasma flows, MHD offers a potentially effective means of flow control and manipulation. Through further MHD studies, different applications of MHD flow control can be developed and utilized to enhance technology in various areas such as propulsion and power generation.

REFERENCES

[1] Kuranov, A. L., and Sheikin, E. G., Magnetohydrodynamic Control on Hypersonic Aircraft Under the Ajax Concept, AIAA Paper 2003; 40(2): 174-182.

[2] Lipinski, Ronald J., Sergey, O. Macheret, Shneider, Mikhail N., and Miles, Richard B., Electron-Beam-Generated Plasmas in Hypersonic Magnetohydrodynamic Channels, AIAA Paper 2001; 39(6): 1127-1138.

[3] Macheret, M., Shneider M. N., and R. B. Miles. Potential Performance of Supersonic MHD Power Generators, AIAA-2001-0795, In: 39th AIAA Aerospace Sciences Meeting and Exhibit.

[4] Magnetohydrodynamic Power Generator. Encyclopedia Britannica. 2005. Encyclopedia Britannica Premium Service. 11 Dec. 2005, Available from http://www.britannica.com/eb/article-45896.

[5] Davidson, P. A. An Introduction to Magnetohydrodynamics, Cambridge, England, Cambridge University Press, 2001.

[6] Goedbloed H. and Stefaan Poedts, Principles of Magnetohydrodynamics, Cambridge, England, Cambridge University Press, 2004.

[7] Martinez-Sanchez M. and J. E. Pollard. Spacecraft electric propulsion – an overview. Journal of Propulsion and Power 1998;14: 688-99.

[8] He, X. and Luo, L.-S. Lattice Boltzmann model for the incompressible navier-stokes equation, J. Stat. Phys. 1997a. 88: 927.

[9] He, X. and Luo, L.-S. Theory of the lattice Boltzmann method: From the Boltzmann equation to the lattice Boltzmann equation a priori derivation of the

lattice Boltzmann equation, Phys. Rev. E. 1997c. 56: 6811.

[10] He, X., Luo, L.-S. and Dembo, M. Some progress in lattice Boltzmann method: Reynolds number enhancement in simulations, Physica A 1997. 239: 276.

[11] Breyiannis, G. and Valougeorgis, D. Lattice kinetic simulations in three-dimensional magnetohydrodynamics, Phys. Rev. E. 2004. 69: 1-4.

[12] Dellar, P. Lattice kinetic schemes for mhd, Journal of Computational Physics 2002. 179: 95126.

[13] Richard, J. C. Lattice-Boltzmann models of ion thruster cathode 3d mhd flows, number H37-00015, American Physical Society Annual March 2005 Meeting.

[14] Richard, J. C. and Shah, P. Lattice-Boltzmann models of ion thrusters, number 23, In: 1st International Conference for Mesoscopic Methods in Engineering and Science (ICMMES). July 26-29, 2004, Braunschweig, Germany. Available from www.icmmes.org.

[15] Richard, J. C. and Young, B. Multi-species lattice-Boltzmann models of xe, xe+, xe++, e- flow through ion thruster optics, number AIAA-2006-5006, In: 42nd AIAA/ASME/SAE/ASEE Joint Propulsion Conference, July 9-12, 2006, Sacramento, California.

[16] Richard, J. C., Young, B. and Shah, P. Lattice-Boltzmann models of xe+ flow in ion thrusters, number AIAA-2005-3689, In: 41st AIAA/ASME/SAE/ASEE Joint Propulsion Conference, July 10-13, 2005, Tucson, Arizona.

[17] Luo, L.-S. and Girimaji, S. S. Lattice Boltzmann model for binary mixtures, Phys. Rev. E. 2002. 66: 035301.

[18] Luo, L.-S. and Girimaji, S. S. Theory of the lattice Boltzmann method: Two-fluid model for binary, Phys. Rev. E. 2003. 67: 036302.

[19] Yu, H., Luo, L.-S. and Girimaji, S. S. Scalar mixing and chemical reaction simulations using lattice Boltzmann method, Int. J. Computat. Eng. Sci. 2002. 3: 71.

[20] He, X. and Doolen, G. Lattice Boltzmann method on a curvilinear coordinate system: Vortex shedding behind a circular cylinder, Phys. Rev. E. 1997a. 56: 434–440.

[21] Yu, D., Girimaji, S. S. and Luo, L.-S. Dns of homogenous turbulence subject to periodic plane-shear rate using lattice Boltzmnann method, Bulletin of the American Physical Society 2003a. 48(10): 91.

[22] Yu, H., Girimaji, S. S. and Luo, L.-S. Lattice Boltzmann simulations of decaying homogenous isotropic turbulence, Bulletin Of The American Physical Society 2003b. 48(10): 91.

[23] Yu, H. and Girimaji, S. S. Near-field turbulent simulations of rectangular jets using lattice Boltzmann method, Physics of Fluids 2005.

[24] Yu, H. and S. S. Girimaji. Lattice Boltzmann equation simulation of rectangular jet (AR=1.5) instability and axis-switching. Physica A 2006;362:151–57.

[25] Guo, Z., Zheng, C. and Shi, B. Discrete lattice effects on the forcing term in the lattice Boltzmann method, Phys. Rev. E. 2002. 65: 046308.

[26] He, X. and Doolen, G. Lattice Boltzmann method on curvilinear coordinates system: Flow around a circular cylinder, J. Comput. Phys. 1997b 134: 306–315.

[27] He, X., Luo, L.-S. and Dembo, M. Some progress in lattice Boltzmann method: Part i. nonuniform mesh grids, J. Comput. Phys. 1996. 129: 357.

[28] Premnath, K. N. and Pattison, M. J. Computation of mhd flows using the lattice Boltzmann method, Santa Barbara, California, MetaHeuristics LLC, 2005.

[29] Tokomak Reactors. 15 Nov. 2006 Available from http://www.upei.ca/~physics/p261/projects/fusion1/tokamaks.htm.

[30] Hill, Phillip and Carl Peterson. An Introduction to Mechanics and Thermodynamics of Propulsion, Reading, Massachusetts, Addison Wesley Publishing Company Inc., 1992.

[31] Wilbur, Paul J., Rawlin, Vincent K., and J. R. Beattie. Ion thruster development trends and status in the United States, AIAA J. Propulsion and Power, 1998. 14(5): 708-715.

[32] Arefiev, Alexey V. and Boris N. Breizman. Theoretical components of the VASIMR plasma propulsion concept. Phys Plasmas 2004;11: 2942-2949.

[33] Magnetoplasmadynamic Thrusters. NASA FACTS 2004. Glenn Research Center. FS-2004-11-022-GRC. Available from www.nasa.gov/centers/glenn/about/nasafact.html.

[34] Pulsed Plasma Thrusters. NASA FACTS 2004. Glenn Research Center. FS-2004-11-023-GRC. Available from www.nasa.gov/centers/glenn/about/nasafact.html.

[35] Zona, Kathleen. DS1: How the ion engine works. Science and Technology. NASA. 11 Oct. 2006 Available from http://www.nasa.gov/centers/glenn/about/history/ipsworks.html.

[36] Anderson J. Hypersonic and High Temperature Gas Dynamics. New York: McGraw-Hill Inc.; 1989.

[37] Vincenti, Walter G. and Charles H. Krueger, Jr. Introduction to Physical Gas Dynamics, Malabar, Florida, Krieger Publishing Company; 2002.

[38] Harris S. An introduction to the theory of the Boltzmann equation. New York: Holt Rinehart and Winston INC; 1970.

[39] Griffiths, David J. Introduction to Electrodynamic Third Edition., Upper Saddle River, New Jersey, Prentice-Hall Inc,1999.

[40] Blanford, Roger and Kip Thorne. Part V Plasma Physics. PH 136: Applications of classical physics. 13 Jul. 2006. Available from http://www.pma.caltech.edu/Courses/ph136/yr2002/chap19/0219.1.pdf.

[41] Helander, Per and Dieter J. Sigmar. Collisional Transport in Magnetized Plasmas, Cambridge, England, Cambridge University Press, 2002.

[42] Woods, L. C. Physics of Plasmas, Weinheim, Germany, Wiley-VCH Verlag GmbH & Co., KGaA, 2004.

[43] d'Humi´eres, D., Ginzburg, I., Krafczyk, M., Lallemand, P. and Luo, L.-S. Multiple relaxation-time lattice Boltzmann models in three dimensions, Phil. Trans. R. Soc. Lond. A . 2002. 220: 437–451.

[44] Krafczyk, M., ¨o lkeh, J. T. and Luo, L.-S. Large-eddy simulations with a multiple-relaxation time lbe model, Int. J. Mod. Phy. B 2003. 17: 33–39.

[45] Shebalin, John V. Broken ergodicity and coherent structure in homogeneous turbulence, Physica D 1989; 37: 173-91.

[46] Shebalin, John V. Magnetic Prandtl Number Effects in MHD Turbulence. In: 31st EPS Conference on Plasma Phys. June 28 – July 2, 2004, London, England; 28G: 1-4.

[47] Shebalin, John V. The statistical mechanics of ideal homogeneous turbulence, NASA TP-2002-210783, (NASA JSC, Houston, Texas).

[48] Shebalin, John V, Matthaeus, W. H., and D. Montgomery. Anisotropy in MHD turbulence due to a mean magnetic field, J. Plasma Phys. 1983; 29: 525-47.

[49] Ting, Antonio C., Matthaeus W. H., and D. C. Montgomery. Turbulent relaxation processes in magnetohydrodynamics. Phys Fluids 1986;29: 3261-3274.

[50] Fyfe D. an D. Montgomery. High beta turbulence in two-dimensional magneto-hydrodynamics, J. Plasma Phys. 1976; 16: 181-91.

[51] Milano L. J., Matthaeus W. H., Dmitruk P., and D. C. Montgomery. Local anisotropy in incompressible magnetohydrodynamic turbulence. Phys Plasmas 2001;8: 2673-2681.

[52] Biskamp D., Magnetohydrodynamic Turbulence, Cambridge, England, Cambridge University Press, 2003.

[53] Pope SB. Turbulent flows. Cambridge, England: Cambridge University Press; 2000.

[54] Heijst, Gertjan van. Vortices in two-dimensional turbulence, In: Belgian Physical Society International Scientific Meeting 2006, Joined BPS and NNV "FYSICA 2006" Meeting, April 28, 2006, Leiden, Netherlands. Available from http://www.nnv.nl/NNV/CORE/00/05/5.HTML.

[55] Kassinos, S. C., Knaepen, B., and D. Carati. MHD turbulence in the presence of a strong magnetic field. In: Proceedings of the Summer Program 2002. Center for Turbulence Research (CTR), Stanford University, Stanford, California. Available from http://www.stanford.edu/group/ctr/Summer/SP02.html.

[56] Ashurst, T. W., Kerstein, A. R., Kerr, R. M., and C. H. Gibson. Alignment of vorticity and scalar gradient with strain rate in simulated Navier-Stokes turbulence. Phys Fluids 1987;8:2343-2353.

[57] Grinstein FF. Self-induced vortex ring dynamics in subsonic rectangular jets. Phys Fluids 1995;7:2519–21.

[58] Grinstein F. F. Vortex dynamics and entrainment in rectangular free jets. J. Fluid Mech. 2001;437:69–101.

[59] Grinstein FF and C. R. DeVore. Dynamics of coherent structures and transition to turbulence in free square jets. Phys Fluids 1996;8:1237–51.

[60] Grinstein FF, Gutmark E., and T. Parr. Near field dynamics of subsonic free square jets. A computational and experimental study. Phys Fluids 1996;8:1237–51.

[61] Gutmark EJ, Grinstein FF. Flow control with noncircular jets. Annu Rev Fluid Mech 1999;31:239–72.

[62] Quinn WR. Turbulent mixing in a free jet issuing from a low aspect ratio contoured rectangular nozzle. Aeronaut J 1995;No. 2110:337–42.

[63] Tsuchiya Y, Horikoshi C, Sato T. On the spread of rectangular jets. Exp Fluids 1986;4:197-204.

[64] Krothapalli A, Baganoff D, Karamcheti K. On the mixing of a rectangular jet. J Fluid Mech 1981;107:201–20.

[65] Sreenivasn, Binod and Alboussiere, Thierry. Experimental study of a vortex in a magnetic field. J. Fluid Mech. 2002;464:287–309.

[66] Harada, H., Okazawa, K., Tanaka, M., and E. Takeuchi. The MHD counterflow around a jet from a nozzle under a DC magnetic field, In: Proceeding, International Symposium on Electromagnetic Processing of Materials, EPM '94, October 25-28, 1994, Nagoya University Symposium, Nagoya, Japan.

VITA

Benjamin M. Riley
89 Lakeview Village
Montgomery, TX 77356
(936) 499-7069
b52@tamu.edu

EDUCATION

M.S. Aerospace Engineering, Texas A&M University, May 2007

B.S. Aerospace Engineering, Texas A&M University, May 2005

EMPLOYMENT

United States Navy Officer

U.S. Navy Nuclear Power School, Jan 2007 - July 2007

NROTC Texas A&M University, Dec 2006 – Jan 2007

Teaching/Research Assistant

Texas A&M University, Jun 2005 – Dec 2006